



저작자표시-비영리-변경금지 2.0 대한민국

이용자는 아래의 조건을 따르는 경우에 한하여 자유롭게

- 이 저작물을 복제, 배포, 전송, 전시, 공연 및 방송할 수 있습니다.

다음과 같은 조건을 따라야 합니다:



저작자표시. 귀하는 원저작자를 표시하여야 합니다.



비영리. 귀하는 이 저작물을 영리 목적으로 이용할 수 없습니다.



변경금지. 귀하는 이 저작물을 개작, 변형 또는 가공할 수 없습니다.

- 귀하는, 이 저작물의 재이용이나 배포의 경우, 이 저작물에 적용된 이용허락조건을 명확하게 나타내어야 합니다.
- 저작권자로부터 별도의 허가를 받으면 이러한 조건들은 적용되지 않습니다.

저작권법에 따른 이용자의 권리는 위의 내용에 의하여 영향을 받지 않습니다.

이것은 [이용허락규약\(Legal Code\)](#)을 이해하기 쉽게 요약한 것입니다.

[Disclaimer](#)

Doctor of Philosophy

**The Developments of Highly Active and Durable  
Nanomaterials for Electrocatalysts**

The Graduate School of the University of Ulsan

Department of Chemistry

**Respati Kevin Pramadewandaru**

**The Developments of Highly Active and Durable  
Nanomaterials for Electrocatalysts**

Supervisor: Professor Jong Wook Hong

A Dissertation

Submitted to

The Graduate School of the University of Ulsan

In partial Fulfillment of the Requirements

for the Degree of

Doctor of Philosophy in Department of Chemistry

by

Respati Kevin Pramadewandaru

Department of Chemistry

University of Ulsan, Korea

February 2024

# The Developments of Highly Active and Durable Nanomaterials for Electrocatalysts

This certifies that the dissertation of Respati Kevin Pramadewandaru is approved.

---

Committee Chair: Professor Min Hyung Lee (이민형)



---

Committee Member: Professor Jong Wook Hong (홍종욱)



---

Committee Member: Professor Jaehoon Jung (정재훈)



---

Committee Member: Professor Dongho Lee (이동호)



---

Committee Member: Professor Young Wook Lee (이영욱)



Department of Chemistry

University of Ulsan, Korea

February 2024



**This thesis is dedicated to my parents.**

For their endless love, support, and encouragement

# Table of Contents

|  |    |
|--|----|
| <b>Abstract</b> .....  | 1  |
| <b>List of Figures/Schemes</b> .....   | 3  |
| <b>Chapter 1. General Introduction</b> .....   | 8  |
| 1.1. The realms of electrochemical applications.....   | 8  |
| 1.2. The progress of nanomaterials.....  | 11 |
| 1.3. Synthetic strategies to enhance the electrocatalytic properties.....  | 12 |
| 1.4. References .....  | 14 |
| <b>Chapter 2. Synergistic Effect of Bimetallic Pd-Pt Nanocrystals for the Highly Efficient Methanol Oxidation Electrocatalysts</b> ..... | 17 |
| 2.1. Introduction .....  | 17 |
| 2.2. Experimental section .....  | 18 |
| 2.2.1. Chemical and materials.....   | 18 |
| 2.2.2. Synthesis of Pd–Pt alloy nanocubes.....   | 19 |
| 2.2.3. Synthesis of Pd@Pt core–shell nanocubes.....  | 19 |
| 2.2.4. Synthesis of Pd nanocubes.....  | 20 |
| 2.2.5. Synthesis of Pt nanocubes.....  | 20 |
| 2.2.6. Preparation of the working electrodes.....  | 20 |
| 2.2.7. Electrochemical measurement .....   | 21 |
| 2.2.8. Characterization .....  | 22 |
| 2.3. Result and Discussion.....  | 23 |
| 2.3.1. Synthesis and characterization of the nanocubes .....   | 23 |
| 2.3.2. Electrocatalytic MOR performance .....  | 29 |
| 2.4. Conclusion .....  | 33 |
| 2.5. References .....  | 34 |
| <b>Chapter 3. Highly Enhanced Electrocatalytic Performances with Dendritic Bimetallic Palladium-Based Nanocrystals</b> .....             | 37 |
| 3.1. Introduction .....  | 37 |
| 3.2. Experimental section .....  | 38 |
| 3.2.1. Chemical and materials.....   | 38 |
| 3.2.2. Synthesis of Pd–Pt NDs .....  | 38 |
| 3.2.3. Characterization .....  | 38 |
| 3.2.4. Electrochemical performance .....   | 39 |
| 3.3. Result and Discussion .....   | 40 |
| 3.4. Conclusion.....   | 51 |
| 3.5. References .....  | 52 |

|   |     |
|---|-----|
| <b>Chapter 4. Universal Synthesis Strategy of Edge-Rich Holey Pt Based Ultrathin Alloy Nanosheets for Efficient Electrochemical Oxygen Reduction Reaction</b> .....   | 55  |
| 4.1. Introduction .....   | 55  |
| 4.2. Experimental section .....   | 56  |
| 4.2.1. Chemicals and materials .....  | 56  |
| 4.2.2. Synthesis of holey ultrathin Pt nanosheets (Pt HU-NSs) .....   | 57  |
| 4.2.3. Synthesis of Pt <sub>3</sub> Ni HU-NSs.....  | 57  |
| 4.2.4. Synthesis of Pt <sub>3</sub> M (M= Co, Cu, Fe, Mn, Pd, Ir, Rh, and Ru) HU-NSs .....  | 57  |
| 4.2.5. XAFS data analysis .....   | 58  |
| 4.2.6. Electrochemical measurements.....  | 58  |
| 4.2.7 Characterization .....  | 60  |
| 4.3. Result and Discussion .....  | 61  |
| 4.4 Conclusion.....   | 78  |
| 4.5. References .....   | 79  |
| <b>Chapter 5. Boron-Insertion Promote Unique Crystal Structure of PdPt Nanocrystals for Superior Electrocatalytic Hydrogen Evolution Activity and Stability</b> ..... | 83  |
| 5.1. Introduction .....   | 83  |
| 5.2. Experimental section .....   | 84  |
| 5.2.1. Chemicals and materials .....  | 84  |
| 5.2.2. Synthesis of Pd-Pt nanocrystals .....  | 84  |
| 5.2.3 Synthesis of B-doped Pd-Pt nanocrystals .....   | 85  |
| 5.2.4 Electrochemical measurements .....  | 85  |
| 5.2.5 Characterization .....  | 85  |
| 5.3. Result and Discussion .....  | 87  |
| 5.4. Conclusion.....  | 102 |
| 5.5 References .....  | 103 |
| <b>Acknowledgement</b> .....  | 105 |
| <b>Curriculum Vitae</b> .....   | 106 |
| <b>List of Publications/Submission</b> .....  | 107 |

## Abstract

This thesis represents research on the fabrication of nanoparticles for electrocatalysis application. It explores their synthesis process, physical, electronic and electrochemical properties. Chapter one provides a brief introduction to the exploration of nanomaterials and their applications for electrocatalysts.

Chapter two describes the study about metal nanocrystals (NCs) with controlled compositional and distributional structures that have gained increasing attention due to their unique properties and broad applications, particularly in fuel cell systems. However, despite the significant importance of composition in metal NCs and their electrocatalytic behavior, comprehensive investigations into the relationship between atomic distribution and electrocatalytic activity remain scarce. In this study, we present the development of four types of nanocubes with similar sizes and controlled compositions (Pd–Pt alloy, Pd@Pt core–shell, Pd, and Pt) to investigate their influence on electrocatalytic performance for methanol oxidation reaction (MOR). The electrocatalytic activity and stability of these nanocubes exhibited variations based on their compositional structures, potentially affecting the interaction between the surface-active sites of the nanocrystals and reactive molecules. As a result, leveraging the synergistic effect of their alloy nanostructure, the Pd–Pt alloy nanocubes exhibited exceptional performance in MOR, surpassing the catalytic activity of other nanocubes, including Pd@Pt core–shell nanocubes, monometallic Pd and Pt nanocubes, as well as commercial Pd/C and Pt/C catalysts.

Chapter three discusses the exploration of efficient nanocatalysts with high activity and stability towards water electrolysis and fuel cell applications is extremely important for the advancement of electrochemical reactions. However, it remains challenging. Controlling the morphology of bimetallic Pd–Pt nanostructures can be a great way to improve their electrocatalytic properties compared with previously developed catalysts. Herein, we synthesize bimetallic Pd–Pt nanodendrites, which consist of a dense matrix of unsaturated coordination atoms and high porosity. The concentration of cetyltrimethylammonium chloride was significant for the morphology and size of the Pd–Pt nanodendrites. Pd–Pt nanodendrites prepared by cetyltrimethylammonium chloride (200 mM) showed

higher activities towards both the hydrogen evolution reaction and methanol oxidation reaction compared to their different Pd–Pt nanodendrites counterparts, commercial Pd, and Pt catalysts, which was attributed to numerous unsaturated surface atoms in well-developed single branches.

Chapter four deeply study about ultrathin two-dimensional (2D) metal nanosheets have attracted significant attention in the field of electrocatalysis. However, only a few of ultrathin nanosheets with limited elements were developed due to difficulties in restraining three-dimensional (3D) growth of metals and stabilizing unstable edge sites. Herein, for the first time, we present a universal synthetic approach for edge-rich holey ultrathin Pt<sub>3</sub>M alloy nanosheets (Pt<sub>3</sub>M HU-NSs, where M = Ni, Co, Cu, Ir, Pd, Ru, Rh, Fe, and Mn) with approximately 3 nm thickness and abundant edge sites through a two-step template-based method involving precisely controlled Pt reduction rates and thermal treatment. The Pt<sub>3</sub>Ni HU-NSs displayed significantly enhanced oxygen reduction reaction activity and stability compared to other Pt<sub>3</sub>M HU-NSs, pure Pt HU-NSs, and the state-of-the-art Pt/C catalysts, attributing to the retention of distinctive morphology and composition of Pt<sub>3</sub>Ni HU-NSs. We believe that highly active ultrathin 2D alloy structures with abundant edge sites and desirable catalytic functions offer a promising avenue for the development of advanced electrocatalysts.

Chapter five study about the exploration of tuning the crystal structure of bimetallic nanocrystals, especially Pd-based nanocatalysts with high activity and stability toward water electrolysis application, is essential for improving electrochemical reactions. Introducing the foreign element into the lattice of Pd-Pt nanocrystals (NCs) can be a great way to modify their neighbor lattice environment and improve their electrocatalytic properties compared with their traditional structure (fcc) of Pd-Pt NCs. Herein, we introduce the B insertion into PdPt NCs, which produces the change of crystal structure from fcc-to-hcp for the hydrogen evolution reaction (HER). We experimentally achieved this with the highly crystalline of PdPt–B NCs. Due to the presence of B atoms, the PdPt–B NCs exhibit higher activities and are incredibly stable towards HER compared to their pristine PdPt NCs, Pt/C, and Pd/C catalysts.

## List of Figures/Schemes

### Chapter 2

**Scheme 2.1.** Geometrical illustration of the Pd–Pt alloy Pd@Pt core–shell, Pd, and Pt nanocubes. Red and green denote Pd and Pt, respectively.

**Figure 2.1.** The SEM images of (a) Pd–Pt alloy, (b) Pd@Pt core-shell, (c) Pd, and (d) Pt nanocubes

**Figure 2.2.** Structure characterization of bimetallic Pd–Pt alloy, Pd@Pt core-shell, Pt and Pd nanocubes. (a) geometric illustration, (b–e) TEM, and (f–i) HR-TEM images including the corresponding FFT images. HAADF-STEM images and corresponding EDS elemental mapping analysis of (j) Pd–Pt alloy and (k) Pd@Pt core-shell nanocubes.

**Figure 2.3.** (a) XRD patterns of bimetallic Pd–Pt alloy, Pd@Pt core-shell, monometallic Pd and Pt nanocubes. The red and black bars are referred to Pt and Pd JCPDS card, respectively. XPS spectra of (b) Pd 3d and (c) Pt 4f of bimetallic Pd–Pt alloy, Pd@Pt core-shell, Pd, and Pt nanocubes, respectively.

**Figure 2.4.** Electrocatalytic MOR properties of bimetallic Pd–Pt alloy, Pd@Pt core-shell, monometallic Pt and Pd nanocubes, including commercial Pt/C and Pd/C in 0.1 M KOH and 0.5 M MeOH at 50 mV s<sup>-1</sup>. (a) CVs curves in 0.1 M KOH and ECSAs of different catalysts. (c) Mass-normalized and (d) ECSA-normalized CV curves of different catalysts. (e) Mass activity and specific activity of different catalysts. (f) CA curves of different catalysts for 5000 s.

**Figure 2.5.** The TEM images of (a) Pd–Pt alloy nanocubes and (b) Pt/C after CAs test.

**Figure 2.6.** (a) CO-stripping measurements of different catalysts and (b) corresponding maximum current potentials. (c) Nyquist plots of different catalysts in 0.1 M KOH at 50 mV s<sup>-1</sup>.

**Table 2.1.** XPS spectra of Pt 4f core levels for nanocubes with different atomic distribution.

**Table 2.2.** XPS spectra of Pd 3d core levels for nanocubes with different atomic distribution.

### Chapter 3

**Figure 3.1.** (a) and (b) HR-TEM image including the correspond FFT images. HAADF-STEM image with (c) corresponding EDS elemental mapping images, and (d) line-scan profiles analysis of Pd (black) and Pt (red) for the Pd-Pt NDs. (e) XRD pattern confirm of corroborating the Pd-Pt bimetallic feature.

**Figure 3.2.** SEM and TEM images of Pd-Pt NDs with controlled CTAC concentration representative to (a); (e); (i) Pd-Pt-10<sub>CTAC</sub> NDs, (b); (f); (j) Pd-Pt-50<sub>CTAC</sub> NDs, (c); (g); (k) Pd-Pt-100<sub>CTAC</sub> NDs, and (d); (h); (l) Pd-Pt-200<sub>CTAC</sub> NDs. Scale bar in the inset figures of parts (e)-(h) is 30 nm.

**Figure 3.3.** XRD Pattern of Pd-Pt NDs with controlled CTAC concentrations. The line pattern shows reference cards 46-1043 and 70-2075 for Pd and Pt according to JCPDS.

**Figure 3.4.** SEM images of Pd-Pt NDs prepared with controlled concentrations of CTAC with higher concentration of (a) 500 mM. Pd-Pt NDs prepared with lower concentration of CTAC than 10 mM with (b) 2.5 mM, (c) 5.0 mM, and (d) 7.5 mM.

**Figure 3.5.** Electrocatalytic HER performance of different Pd-Pt NDs, and commercial Pd/C and Pt/C electrocatalysts measured in 0.5 M H<sub>2</sub>SO<sub>4</sub> saturated with N<sub>2</sub>; sweep rate at 50 mV s<sup>-1</sup> (CVs) and 10 mV s<sup>-1</sup> (LSV). (a) CVs of all PdPt electrocatalysts. (b) LSV polarization curves and (c) derived from (b) to see details of H<sub>2</sub> evolution in overpotential at 10 mA cm<sup>-2</sup> of all electrocatalysts including commercials. (d) corresponded Tafel plots recorded on the electrode by polarization curves at potential 10 mV s<sup>-1</sup>.

**Figure 3-6.** MOR performance of different Pd-Ptx NDs and commercial Pd/C and Pt/C electrocatalysts measured in 1.0 M KOH containing 1.0 M methanol saturated with N<sub>2</sub>; sweep rate at 50 mV s<sup>-1</sup>. (a) CVs of all catalysts and (b) ECSA of all values of different electrocatalysts include commercials. MOR of all metals (Pd + Pt) (c) mass-normalized CV curves, (d) specific activity-normalized CV curves, and (e) Mass and specific activity data based on all different electrocatalysts. (f) Durability evaluation by chronoamperometry tests at -0.15 V vs. Hg/HgO for 30 minutes off all electrocatalysts.

**Figure 3.7.** MOR residual current density activities of Pd-Pt-200<sub>CTAC</sub> NDs, Pd/C and Pt/C after chronoamperometry experiment for 30 minutes.

**Table 3.1.** Activities values for all electrocatalysts including commercial Pd/C and Pt/C in HER activity.

The values including overpotential at  $10 \text{ mA cm}^{-2}$  and Tafel plots as compares in  $0.5 \text{ M H}_2\text{SO}_4$ .

**Table 3.2.** Comparative results for electrochemical MOR activity based on previous re-ports using Pd-Pt based catalysts in the literature.

## Chapter 4

**Scheme 4.1.** Schematic illustration for the synthesis procedure of  $\text{Pt}_3\text{M HU-NSs}$ .

**Figure 4.1.** (a) SEM and (b, c) TEM images of Pt NSs. (d) low- and (e) high-magnification HAADF-STEM images of Pt HU-NSs. (f) XRD pattern of Pt HU-NSs.

**Figure 4.2.** TEM images showing time dependent growth and shape evolution of Pt HU-NSs: reaction at (a, f) 15, (b, g) 20, (c, h) 25, (d, i) 30, and (e, j) 35 min.

**Figure 4.3.** HAADF-STEM and corresponding EDS elemental mapping images of various  $\text{Pt}_3\text{M HU-NSs}$ . (a)  $\text{Pt}_3\text{Ni HU-NSs}$ . (b)  $\text{Pt}_3\text{Co HU-NSs}$ . (c)  $\text{Pt}_3\text{Cu HU-NSs}$ . (d)  $\text{Pt}_3\text{Mn HU-NSs}$ . (e)  $\text{Pt}_3\text{Fe HU-NSs}$ . (f)  $\text{Pt}_3\text{Pd HU-NSs}$ . (g)  $\text{Pt}_3\text{Ir HU-NSs}$ . (h)  $\text{Pt}_3\text{Rh HU-NSs}$ . (i)  $\text{Pt}_3\text{Ru HU-NSs}$ .

**Figure 4.4.** XRD patterns of various  $\text{Pt}_3\text{M HU-NSs}$ . The red bars showing the reference of ICDD #00-001-1194 (Pt).

**Figure 4.5.** (a) SEM, (b) HAADF-STEM, and (c) TEM images of  $\text{Pt}_3\text{Ni HU-NSs}$ . (d) TEM image of side-face of the  $\text{Pt}_3\text{Ni HU-NSs}$ . (e) Atomic-resolution aberration corrected HAADF-STEM image of a  $\text{Pt}_3\text{Ni HU-NS}$  and corresponding FFT pattern. (f) EDS elemental mapping images of a  $\text{Pt}_3\text{Ni HU-NS}$ .

**Figure 4.6.** XAFS measurements for the  $\text{Pt}_3\text{Ni HU-NSs}$  and Pt HU-NSs. XANES spectra at the (a) Pt  $\text{L}_3$ -edge of the  $\text{Pt}_3\text{Ni HU-NSs}$ , Pt HU-NSs, and Pt foil and (b) Ni K-edge of the  $\text{Pt}_3\text{Ni HU-NSs}$  and Ni foil. Fourier-transformed  $k^3$ -weighted EXAFS spectra for (c) Pt  $\text{L}_3$ -edge and (d) Ni K-edge of the catalysts.

**Figure 4.7.** (a) SEM and (b) HAADF-STEM-EDS elemental mapping images of Pt-Ni NCs.

**Figure 4.8.** SEM images of Pt nanostructrues with different reaction temperatures at (a) 30, (b) 40, (c) 50, (d) 60, (e) 80, and (f) 100 °C.



**Figure 4.9.** SEM images of nanostructures prepared with different amount of (a-d) CTAC and (e-h) PVP. For CTAC: (a) 0, (b) 50, (c) 200, and (d) 500 mM. For PVP: (e) 0, (f) 200, (g) 300, and (h) 400 mg.

**Figure 4.10.** TEM images showing the time dependent transformation from Pt HU-NSs to Pt<sub>3</sub>Ni HU-NSs; (a, f) 0, (b, g) 30, (c, h) 90, (d, i) 270, and (e, j) 360 min. Changes in the (k) composition of metal elements, (l) pore size, and thickness of intermeidate products during the reaction.

**Figure 4.11.** Electrochemical properties of different catalysts. (a) CVs and (b) ORR curves of different catalysts. (c) Mass activity and specific activities of different catalysts at 0.9V<sub>RHE</sub>. (d) CVs and (e) ORR curves of Pt-Ni alloy catalysts with different Pt/Ni atomic ratios and (f) corresponding mass activity and specific activities of the catalysts at 0.9V<sub>RHE</sub>. ORR curves for (g) Pt<sub>3</sub>Ni HU-NS/C, (h) Pt HU-NS/C, and (i) commercial Pt/C catalysts before and after 5000 and 10000 cycles in an O<sub>2</sub>-saturated 0.1 M HClO<sub>4</sub> solution. The insets displaying the CVs before and after the durability test for each catalyst. (j) Bar graph showing changes in specific activities before and after durability test for each catalyst.

**Figure 4.12.** (a) UPS and (b) XPS valence-band spectra of Pt<sub>3</sub>Ni HU-NSs, Pt HU-NSs, and Pt/C. (c) CO-stripping voltammogram of the catalysts.

**Table 4.1.** The atomic ratio of Pt<sub>3</sub>M HU-NSs determined by ICP-OES and EDS analysis.

**Table 4.2.** The ECSA, Mass and specific activities of Pt<sub>3</sub>M HU-NS/C, Pt Hu-NS/C, and Pt/C.

## Chapter 5

**Scheme 5.1.** Schematic illustration of synthesis PdPt–B NPs

**Figure 5.1.** The characterization of (a–d) PdPt NPs and (e–j) PdPt–B NPs. (a, e) TEM images, (b, f) STEM image, (c, h) inset high magnification-STEM images, (d, i) FFT patterns, and (j) HAADF-STEM-EDS mapping images, respectively.

**Figure 5.2.** XRD patterns of pristine PdPt to hcp-PdPt–B NCs. The lines on the bottom show standard XRD pattern of fcc-PdPt structure and hcp-Pd structure.

**Figure 5.3.** XAS and XPS spectra of the catalysts. (a, b) XANES spectra, (c, d) EXAFS spectra of Pd

K-edge and Pt L<sub>3</sub>-edge, (e, f) XPS spectra of Pd 3d and Pt 4f.

**Figure 5.4.** Electrocatalytic performances of PdPt–B NCs, PdPt NCs, Pt/C, and Pd/C under acid conditions. (a) CVs curves, (b) HER Polarization curves recorded in N<sub>2</sub>-saturated 0.5 M H<sub>2</sub>SO<sub>4</sub> electrolyte at a scan rate of 10 mV s<sup>-1</sup>, (c) Tafel plots for HER obtained from the corresponding polarization curves in (b), and (d) Comparison of the overpotentials for different catalysts at the current density of 10 mA cm<sup>-2</sup> and Tafel plots, respectively. (e) Exchange current density and (f) EIS spectra of the PdPt–B NCs, PdPt NCs, commercial Pt/C and commercial Pd/C. (g-i) HER polarization curves of PdPt–B NCs, PdPt-B<sub>12h</sub> NCs and PdPt NCs before and after the accelerated durability test. Inset: the chronopotentiometric test of the PdPt–B catalysts at potentials of 10 mA cm<sup>-2</sup> for 100 days.

**Figure 5.5.** (a) Cyclic voltammograms, (b) HER polarization curves, (c) Comparison of the overpotentials for different catalysts at the current density of 10 mA cm<sup>-2</sup>, (d) Tafel plots for HER obtained from the corresponding polarization curves in (a) of various PdPt–B and PdPt NCs include counterpart of Pt/C and Pd/C.

**Figure 5.6.** TEM images before and after chronopotentiometric test for PdPt–B NCs. The (a) before and (b) after test for PdPt–B NCs, respectively.

**Table 5.1.** EDS and ICP-OES analysis result of atomic ratio Pd: Pt: B in PdPt and PdPt–B NCs.

**Table 5.2.** Binding energy value of Pd 3d and Pt 4f of PdPt–B and PdPt NCs include Pd and Pt.Z

**Table 5.3.** Activity values for PdPt–B NCs depending on reaction time including commercial Pd/C and Pt/C in HER activity. The value including overpotential at 10 mA cm<sup>-2</sup> and Tafel plots compared in 0.5 M H<sub>2</sub>SO<sub>4</sub>.

**Table 5.4.** The comparison of HER performance of PdPt–B NCs with some representative Pd-based electrocatalysts in acidic media (0.5 M H<sub>2</sub>SO<sub>4</sub>).

## Chapter 1. General Introduction

### 1.1. The realms of electrochemical applications

At present, nearly all chemical production processes, energy conversions, and storage procedures rely heavily on catalysts to operate efficiently. This growing industrial demand has driven extensive exploration into advanced catalysts. Furthermore, electrocatalytic reactions like oxygen reduction reaction (ORR), oxidation of small organic molecules (such as methanol, ethanol, formic acid, etc.), hydrogen evolution reaction (HER), oxygen evolution reaction (OER), nitrogen reduction reaction (NRR), and carbon dioxide reduction reaction (CO<sub>2</sub>RR) have inspired researchers to develop high-performance catalytic materials. These reactions play a pivotal role in promoting the comprehensive conversion of renewable sources by applying external potential. Currently, state-of-the-art electrocatalysts primarily rely on noble-metal-based catalysts, such as platinum (Pt), Palladium (Pd), ruthenium (Ru), Iridium (Ir), rhodium (Rh), and gold (Au).<sup>1-3</sup> However, the high cost and limited availability of these noble metals have impeded the widespread adoption of electrocatalytic applications.<sup>4-6</sup>

Hydrogen (H<sub>2</sub>) is considered a promising alternative to conventional fossil fuels for energy storage and conversion. H<sub>2</sub> offers several advantages, including the highest gravimetric energy density and zero emissions of pollution, making it an environmentally friendly option. Traditionally, H<sub>2</sub> is generated through processes like steam reforming of methane or gasification of coal, which result in significant greenhouse gas emissions.<sup>7-9</sup> A sustainable approach to H<sub>2</sub> production involves water splitting, a method that entails the cathodic hydrogen evolution reaction (HER) and the anodic oxygen evolution reaction (OER). This approach is environmentally friendly compared to other methods, making it a viable solution for clean energy production. Usually, the generation of hydrogen contains two reaction pathways (Volmer–Heyrovsky pathway or Volmer–Tafel pathway) based on the following three reactions.

- i. Volmer step:  $\text{H}^+ + \text{e}^- + * \rightarrow \text{H}^*$  (1)
- ii. Heyrovsky step:  $\text{H}^* + \text{H}^+ + \text{e}^- \rightarrow \text{H}_2 + *$
- iii. Tafel step:  $2\text{H}^* \rightarrow \text{H}_2 + 2*$

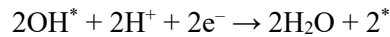
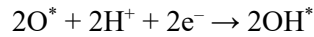
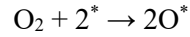
In evaluating HER performance, both theoretical and experimental results have emphasized the importance of the adsorption free energy of  $H^*$  ( $\Delta G_{H^*}$ ) as a crucial performance index, especially in acidic environments. For alkaline conditions, in addition to  $\Delta G_{H^*}$ , the kinetic barriers for water dissociation also play a significant role. Moreover, considering the competitive inhibition behavior of  $OH^-$  from alkaline solutions, appropriate  $OH^*$  adsorption is equally essential. While platinum (Pt) has been historically hailed as the best electrocatalyst for HER, its limited availability and high cost hinder large-scale industrial applications.<sup>10-12</sup> Researchers are actively seeking high efficiency electrocatalysts that are cost-effective and environmentally friendly. Recent advancements in nanomaterials have shown promising potential in hydrogen generation, prompting a comprehensive overview of their achievements in the HER field.

In the context of other applications, such as next-generation energy conversion and storage devices like fuel cells, metal–air batteries, and certain electrolyzers, the oxygen reduction reaction (ORR) serves a pivotal role in determining the overall device performance.<sup>13, 14</sup> Currently, commercial ORR catalysts primarily use Pt/C with Pt content ranging from 20–42 wt%. However, the high cost and scarcity of Pt limit their large-scale commercial use. Utilizing Pt at the atomic level can fundamentally address these challenges. Various nanomaterials play a crucial role in green conservation catalysis due to their size effect, high-efficiency atom utilization, and unique interactions between support and active centers. The rational design of ORR catalysts must adhere to specific standards, ensuring that the adsorption of  $O_2$  molecules on specific sites strikes a balance between being neither too strong nor too weak. This balance is vital because subsequent reaction steps are greatly influenced by the binding energy of O and active sites.<sup>15, 16</sup>

The electrochemical ORR occurs through either a direct four-electron ( $4e^-$ ) pathway or a two-electron ( $2e^-$ ) transfer, reducing  $O_2$  to  $H_2O$  or  $OH^-$  as final products in acidic or basic solutions, respectively. The  $4e^-$  pathway is preferred in fuel cell devices, while the  $2e^-$  pathway provides a green synthesis method for the versatile clean oxidant  $H_2O_2$ . In fact, there is a significant industrial demand for  $H_2O_2$ , with approximately 4 million tons required annually. Therefore, electrochemical synthesis of  $H_2O_2$

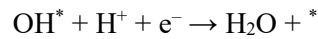
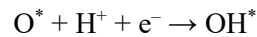
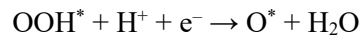
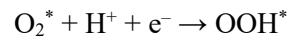
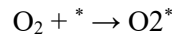
presents a promising avenue. In acidic solutions, the  $4e^-$  pathway is considered the primary dissociation pathway of  $O_2$ .<sup>17, 18</sup>

*Dissociation pathway*

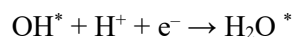
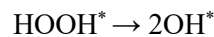
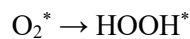


However, the  $4e^-$  pathway of two-step  $2e^-$  transfer involves two mechanisms: associative and peroxo pathways.

*Associative pathway*



*Peroxo pathway*



In practical applications, due to the serious corrosion behavior of hydroxyl radicals derived from  $H_2O$  to device, the  $4e^-$  pathway is highly preferred and the  $2e^-$  is highly limited. The  $2e^-$  pathway includes the formation of hydrogen peroxide ions as an intermediate, which can be used for  $H_2O_2$  production in industry.<sup>19, 20</sup>

Besides, with the development of next-generation fuel cells, the organic-molecule-dominant anodic reaction within direct fluid fuel cells, such as formic acid, methanol, ethanol, ethylene glycol, etc., are regarded as another promising alternatives for conventional fossil energy due to their high energy density, zero pollution emissions, and sustainable access. Among them, direct methanol fuel cells

(DMFCs), direct ethanol fuel cells (DEFCs), and direct formic acid fuel cells (DFAFCs) as half anodic reaction are widely applied in direct fluid fuel cells.<sup>21-23</sup> However, under the current severe circumstances that technical bottleneck and economical barriers, realizing the large-scale applications in the world still meet many issues, especially on the advanced electrocatalysts, which control the main reaction process to some extent. Until now, enormous advanced electrocatalysts for direct fluid fuel cells are reported, such as Pt-based<sup>24-28</sup> catalysts and Pd-based catalyst.<sup>29-31</sup>

## **1.2. The progress of nanomaterials**

Nanomaterials represent a remarkable category of materials characterized by their unique size range, typically falling between 1 to 100 nanometers in at least one dimension. These materials offer an extraordinary advantage due to their exceptionally high surface areas, which can be strategically tailored through the rational design of nanomaterial structures. Nanomaterials exhibit distinctive magnetic, electrical, optical, mechanical, and catalytic properties that substantially deviate from their bulk counterparts.<sup>25</sup> These properties can be precisely adjusted to meet specific requirements by controlling size, shape, synthesis conditions, and appropriate functionalization.<sup>32</sup>

Essentially, nanomaterials can have different atomic structures: some are well-ordered (crystalline), while others have a disordered arrangement (amorphous). The structure affects their properties. Materials can change from one structure to another due to pressure and temperature. For example, under high pressure, some materials become disordered, and disordered materials can become ordered. These changes often lead to new properties that can be used in various applications.<sup>33</sup> Nanomaterials are easier to control because their growth depends on surface features and other factors. By adjusting experimental conditions, scientists can precisely control the structure of nanomaterials. This control is crucial for understanding how the structure affects the material's properties, essential for designing nanomaterials for specific uses. Exploring different structures in nanomaterials helps discover new properties and applications.

In recent years, scientists have made significant progress in controlling the structure of nanomaterials to achieve unique properties.<sup>34</sup> While people usually change nanomaterials by altering their composition, shape, size, or other factors, changing their atomic structure (phase engineering) is a powerful way to

control their properties.<sup>35</sup> Phase engineering focuses on designing, making, and transforming different atomic structures in nanomaterials. It involves understanding how to create nanomaterials with specific structures, change their structures, grow structures with different phases, and create nanomaterials with ordered and disordered parts. This level of control enables fine-tuning nanomaterial attributes for a wide range of applications, especially electrocatalytic applications.

### **1.3. Synthetic strategies to enhance the electrocatalytic properties**

In the realm of electrocatalysis, enhancing the activity, or the rate of reaction, of a nanocatalyst system typically involves two approaches: firstly, augmenting the number of active sites on a specific electrode. This can be achieved by increasing loading or optimizing the nanocatalyst structure to expose more active sites per gram. Secondly, boosting the intrinsic activity of each active site is another viable strategy. Importantly, these methods are not mutually exclusive and can ideally be pursued simultaneously, resulting in the most significant enhancements in activity.<sup>36, 37</sup>

However, it is crucial to recognize that there are inherent constraints regarding the amount of catalyst material that can be loaded onto an electrode. This limitation arises from the need to maintain other vital processes, such as charge and mass transport, which can be adversely affected if the loading exceeds certain physical thresholds. Balancing these factors is essential for effectively designing and optimizing electrocatalytic systems.<sup>38, 39</sup>

Herein, several critical strategies to enhance the electrocatalytic properties based on increasing the number of active sites and increasing the intrinsic activity of nanocatalysts are detailed below:

1. The synthesis of nanomaterials through cost-effective routes is one of various major strategies. High-quality nanomaterials are generally produced using sophisticated instrumentation and harsh conditions, limiting their large-scale production.
2. Another major strategy is the crystal phase adjustment and face regulation in nanomaterials. The atomic arrangement or electronic structure can fundamentally change physical and chemical properties, and these strategies increase intrinsic activity.
3. The heteroatomic doping in nanomaterials, this doping of metallic or non-metallic elements into the original materials, modulates the different functioned surface atoms and/or change of

electronic structures of main (original) materials, which might effectively modify the adsorption strength of the intermediate species in the catalytic reaction.

4. Modulating the ligand and strain effects in the nanomaterials changes the electronic structures of the main (original) materials. The different sizes and electronics of atomic metal and/or non-metal optimize the local density of states of main materials, improving the catalytic reaction.

Concurrently, we have examined and understood the relationships between various nanostructures and catalytic performance. These insights have been directly translated into significant improvements in catalytic activity and stability for a wide range of electrochemical reactions, including the oxygen reduction reaction (ORR), hydrogen evolution reaction (HER), and alcohol oxidation reaction (AOR). Through critical assessment of the latest synthetic innovations and the resulting advances in catalytic performance, this research illustrates nanoparticle catalyst design and reveals opportunities for future development.

In conclusion, our collective efforts in renewable energy generation, electrocatalysis, and nanomaterial research are paving the way for a sustainable future. Delving deeper into these technologies advances scientific knowledge and propels us toward a future powered by renewable energy. By harnessing the power of electrochemical processes and mastering the intricacies of nanomaterials, we are shaping a world where clean and efficient energy sources drive progress, preserving our environment and improving lives globally. Together, we are on the path to a brighter, greener future.



#### 1.4. References

1. Saleem, F.; Zhang, Z.; Xu, B.; Xu, X.; He, P.; Wang, X. *J. Am. Chem. Soc.* **2013**, 135, (49), 18304-7.
2. Kulkarni, A.; Siahrostami, S.; Patel, A.; Norskov, J. K. *Chem. Rev.* **2018**, 118, (5), 2302-2312.
3. Xie, C.; Niu, Z.; Kim, D.; Li, M.; Yang, P. *Chem. Rev.* **2020**, 120, (2), 1184-1249.
4. Lingzheng Bu; Nan Zhang; Shaojun Guo; Xu Zhang; Jing Li; Jianlin Yao; Tao Wu; Gang Lu; Jing-Yuan Ma; Dong Su; Huang, X. *Science* **2016**, 354, (6318), 140-1414.
5. Hunt, S. T.; Roman-Leshkov, Y. *Acc. Chem. Res.* **2018**, 51, (5), 1054-1062.
6. Ye, C.; Peng, M.; Li, Y.; Wang, D.; Chen, C.; Li, Y. *Sci. China-Mater.* **2022**, 66, (3), 1071-1078.
7. Zheng, Y.; Jiao, Y.; Qiao, S. Z. *Adv. Mater.* **2015**, 27, (36), 5372-8.
8. Jamesh, M. I. *J. Power Sources* **2016**, 333, 213-236.
9. Mao, J.; He, C. T.; Pei, J.; Liu, Y.; Li, J.; Chen, W.; He, D.; Wang, D.; Li, Y. *Nano Lett.* **2020**, 20, (5), 3442-3448.
10. Zhou, Q.; Shen, Z.; Zhu, C.; Li, J.; Ding, Z.; Wang, P.; Pan, F.; Zhang, Z.; Ma, H.; Wang, S.; Zhang, H. *Adv. Mater.* **2018**, 30, (27), e1800140.
11. Yang, S.; Li, S.; Song, L.; Lv, Y.; Duan, Z.; Li, C.; Praeg, R. F.; Gao, D.; Chen, G. *Nano Research* **2019**, 12, (11), 2881-2888.
12. Zhu, J.; Hu, L.; Zhao, P.; Lee, L. Y. S.; Wong, K. Y. *Chem. Rev.* **2020**, 120, (2), 851-918.
13. Calle-Vallejo, F.; Pohl, M. D.; Reinisch, D.; Loffreda, D.; Sautet, P.; Bandarenka, A. S. *Chem. Sci.* **2017**, 8, (3), 2283-2289.
14. Lai, J.; Lin, F.; Tang, Y.; Zhou, P.; Chao, Y.; Zhang, Y.; Guo, S. *Adv. Energy Mater.* **2019**, 9, (8), 1800684.
15. Kariuki, N. N.; Khudhayer, W. J.; Karabacak, T.; Myers, D. J. *ACS Catal.* **2013**, 3, (12), 3123-3132.
16. Calle-Vallejo, F.; Tymoczko, J.; Colic, V.; Loffreda, D.; Schuhmann, W.; Bandarenka, A. S. *Science* **2015**, 350, (6257), 185-188.
17. Wang, Y.; Wang, D.; Li, Y. *SmartMat* **2021**, 2, (1), 56-75.
18. Luo, L.; Tan, Z.; Fu, C.; Xue, R.; Cheng, X.; Bi, T.; Zhao, L.; Guo, Y.; Cai, X.; Yin, J.; Shen, S.; Zhang, J. *Chem. Eng. J.* **2023**, 451, 138786.
19. Lin, F.; Lv, F.; Zhang, Q.; Luo, H.; Wang, K.; Zhou, J.; Zhang, W.; Zhang, W.; Wang, D.; Gu, L.; Guo, S. *Adv. Mater.* **2022**, 34, (27), e2202084.

20. Wang, Q.; Guesmi, H.; Tingry, S.; Cornu, D.; Holade, Y.; Minteer, S. D. *ACS Energy Lett.* **2022**, *7*, (3), 952-957.
21. Mekhilef, S.; Saidur, R.; Safari, A. *Renew. Sust. Energ. Rev.* **2012**, *16*, (1), 981-989.
22. Qin, Y.; Zhang, X.; Dai, X.; Sun, H.; Yang, Y.; Shi, Q.; Gao, D.; Wang, H. *J. Mater. Chem. A* **2015**, *3*, (20), 10671-10676.
23. Li, C.; Clament Sagaya Selvam, N.; Fang, J. *Nanomicro Lett.* **2023**, *15*, (1), 83.
24. Kim, Y. T.; Ohshima, K.; Higashimine, K.; Uruga, T.; Takata, M.; Suematsu, H.; Mitani, T. *Angew. Chem. Int. Ed. Engl.* **2006**, *45*, (3), 407-411.
25. Chen, Q. S.; Zhou, Z. Y.; Vidal-Iglesias, F. J.; Solla-Gullon, J.; Feliu, J. M.; Sun, S. G. *J. Am. Chem. Soc.* **2011**, *133*, (33), 12930-3.
26. Chen, G.; Xu, C.; Huang, X.; Ye, J.; Gu, L.; Li, G.; Tang, Z.; Wu, B.; Yang, H.; Zhao, Z.; Zhou, Z.; Fu, G.; Zheng, N. *Nat. Mater.* **2016**, *15*, (5), 564-9.
27. Cao, Z.; Chen, Q.; Zhang, J.; Li, H.; Jiang, Y.; Shen, S.; Fu, G.; Lu, B. A.; Xie, Z.; Zheng, L. *Nat. Commun.* **2017**, *8*, 15131.
28. Wang, Y.; Zheng, M.; Sun, H.; Zhang, X.; Luan, C.; Li, Y.; Zhao, L.; Zhao, H.; Dai, X.; Ye, J.-Y.; Wang, H.; Sun, S.-G. *Appl. Catal. B-Environ.* **2019**, *253*, 11-20.
29. Liu, R.; Zhang, L. Q.; Yu, C.; Sun, M. T.; Liu, J. F.; Jiang, G. B. *Adv. Mater.* **2017**, *29*, (7), 1604571.
30. Guo, J.; Gao, L.; Tan, X.; Yuan, Y.; Kim, J.; Wang, Y.; Wang, H.; Zeng, Y. J.; Choi, S. I.; Smith, S. C.; Huang, H. *Angew. Chem. Int. Ed. Engl.* **2021**, *60*, (19), 10942-10949.
31. Chen, Q.; Jin, H.; Cheng, T.; Wang, Z.; Ren, Y.; Tian, J.; Zhu, Y. *Nanoscale* **2023**, *15*, (8), 3772-3779.
32. Poerwoprajitno, A. R.; Gloag, L.; Cheong, S.; Gooding, J. J.; Tilley, R. D. *Nanoscale* **2019**, *11*, (41), 18995-19011.
33. Cheng, W.; Sun, L.; He, X.; Tian, L. *Dalton Trans.* **2022**, *51*, (20), 7763-7774.
34. Baig, N.; Kammakam, I.; Falath, W. *Mater. Adv.* **2021**, *2*, (6), 1821-1871.
35. Chen, Y.; Lai, Z.; Zhang, X.; Fan, Z.; He, Q.; Tan, C.; Zhang, H. *Nat. Rev. Chem.* **2020**, *4*, (5), 243-256.
36. Seh, Z. W.; Kibsgaard, J.; Dickens, C. F.; Chorkendorff, I.; Norskov, J. K.; Jaramillo, T. F. *Science* **2017**, *355*, (6321), 146.
37. Poerwoprajitno, A. R.; Cheong, S.; Gloag, L.; Gooding, J. J.; Tilley, R. D. *Acc. Chem. Res.* **2022**, *55*, (12), 1693-1702.

38. Chen, T.; Foo, C.; Edman Tsang, S. C. *Chem. Sci.* **2020**, 12, (2), 517-532.
39. Govindarajan, N.; Kastlunger, G.; Heenen, H. H.; Chan, K. *Chem. Sci.* **2021**, 13, (1), 14-26.

## Chapter 2. Synergistic Effect of Bimetallic Pd-Pt Nanocrystals for the Highly Efficient Methanol Oxidation Electrocatalysts

### 2.1. Introduction

Over the past few decades, there has been significant focus on high-performance fuel cells, which efficiently convert chemical energy into electrical energy while avoiding the emission of harmful gases.<sup>1-6</sup> Among the various fuel cell types, direct methanol fuel cells (DMFCs) have garnered attention due to their exceptional energy density, high conversion efficiency, light-weight nature, and comparatively low operating temperature.<sup>7-9</sup> Nevertheless, the slow kinetics of anodic oxidation and surface CO poisoning hinder the practical implementation of DMFCs.<sup>10,11</sup> As a result, extensive research efforts have been initiated in this field.

Pt is widely recognized as one of the primary electrocatalysts utilized in various applications.<sup>12-14</sup> To pave the way for the eventual large-scale commercialization of fuel cells, significant attention has been dedicated to advancing Pt-based materials, aiming to develop cost-effective, highly efficient, and long-lasting electrocatalysts.<sup>15-17</sup> Currently, efforts are being directed towards addressing catalytic activity by means of controlling factors such as surface structure and composition.<sup>18-27</sup> Among the various strategies, the control of compositional structure in Pt-based bimetallic nanocrystals (NCs) has emerged as a highly effective strategy for manipulating their electronic and geometric properties.<sup>28-30</sup> This approach enables the optimization of the catalytic active centres, leading to the modification of adsorption/desorption properties of the intermediates involved in the methanol oxidation reaction (MOR).<sup>31-33</sup> Among various metals for the formation of Pt-based bimetallic NCs, Pd is recognized for its capability to augment the MOR activity and durability of Pt-based catalysts.<sup>34-37</sup> Given this background, Pd–Pt bimetallic NCs are widely regarded as highly promising candidates for efficient electrocatalysis in the MOR. However, the preparation of Pd–Pt bimetallic NCs with precisely controlled compositional structures and the in-depth investigation of their MOR properties have been rarely explored to date.

Herein, we prepared Pd–Pt alloy, Pd@Pt core–shell, Pd, and Pt nanocubes with identical {100} facets and similar edge size to investigate the effect of atomic distribution in Pd–Pt bimetallic NCs for

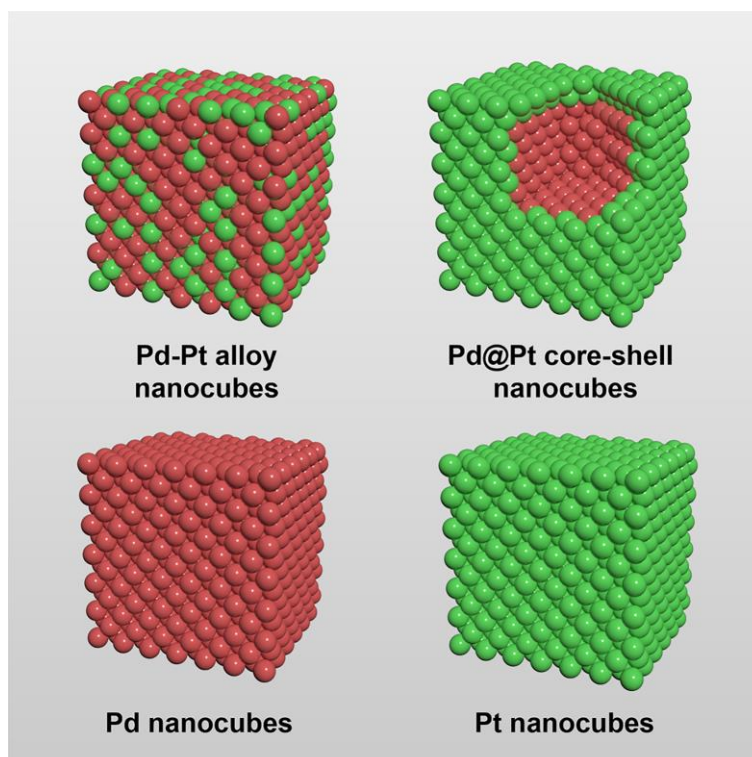
electrochemical MOR (**Scheme 2.1**). The four types of nanocubes have different atomic distributions. The surface of Pd–Pt alloy nanocubes is composed of both Pd and Pt atoms, while Pd@Pt core–shell nanocubes have a Pt surface and a Pd core region. Unlike the bimetallic Pd–Pt alloy and Pd@Pt core–shell nanocubes, Pd and Pt nanocubes are exclusively composed of pure Pd or Pt atoms, respectively. This distinct atomic distribution enables the study of compositional structure-dependent electrocatalytic performance. Indeed, the present work demonstrates that electrocatalytic activity of the Pd–Pt bimetallic nanocubes highly depends on their atomic distribution and combinations. Among the nanocubes, the Pd–Pt alloy nanocubes exhibited enhanced electrocatalytic activities than the Pd@Pt core–shell, Pt, and Pd nanocubes. Furthermore, Pd–Pt alloy nanocubes exhibited larger MOR activity than commercial Pt/C and Pd/C catalysts due to their optimal electronic structure. Apart from their superior MOR activity, the Pd–Pt alloy nanocubes also exhibited higher stability compared to the other nanocubes, as well as Pt/C and Pd/C catalysts. The controlled catalysis experiments unambiguously demonstrate that the activity and stability of the bimetallic NCs can be tuned by controlling their compositional structure.

## **2.2. Experimental section**

### **2.2.1. Chemical and materials**

Chloroform ( $\text{CHCl}_3$ , 99%, JUNSEI), chloroplatinic acid hexahydrate ( $\text{H}_2\text{PtCl}_6 \cdot 6\text{H}_2\text{O}$ ,  $\geq 99\%$ , Sigma-Aldrich), glucose ( $\text{C}_6\text{H}_{12}\text{O}_6$ , 99%, Sigma-Aldrich), hexadecyltrimethylammonium bromide ( $\text{C}_{19}\text{H}_{42}\text{BrN}$ ,  $\geq 99\%$ , Sigma-Aldrich), l-ascorbic acid ( $\text{C}_6\text{H}_8\text{O}_6$ , AA, Daejung), methanol ( $\text{CH}_3\text{OH}$ , MeOH, 99.8%, Junsei), Nafion® perfluorinated resin solution (5 wt%, Sigma-Aldrich), N,N-dimethylformamide (DMF, 99.5%, Sigma-Aldrich), oleic acid ( $\text{C}_{18}\text{H}_{32}\text{O}_2$ , OLA, 90%, Sigma-Aldrich), oleylamine ( $\text{C}_{18}\text{H}_{37}\text{N}$ , OAm, 70%, Sigma-Aldrich), commercial Pd/C (20 wt%, Alfa Aesar), commercial Pt/C (20 wt%, Alfa Aesar), poly(vinylpyrrolidone) (PVP, MW = 55 000, Sigma-Aldrich), potassium bromide (KBr,  $\geq 99\%$ , Sigma Aldrich), potassium chloride (KCl,  $\geq 99\%$ , Sigma Aldrich), potassium hydroxide (KOH, 95%, Samchun), potassium tetrachloroplatinate ( $\text{K}_2\text{PtCl}_4$ ,  $>99.9\%$ , Sigma-Aldrich), sodium tetrachloropalladate ( $\text{Na}_2\text{PdCl}_4$ ,  $>99.9\%$ , Sigma-Aldrich), sodium iodide (NaI,  $\geq 99.99\%$ , Sigma-

Aldrich), and other chemicals were reagent grade and deionized water (DI) with a resistivity of greater than 18.3 M $\Omega$  cm was used in the preparation of reaction solutions.



**Scheme 2.1.** Geometrical illustration of the Pd–Pt alloy Pd@Pt core–shell, Pd, and Pt nanocubes. Red and green denote Pd and Pt, respectively.

### 2.2.2. Synthesis of Pd–Pt alloy nanocubes

In a typical synthesis of Pd–Pt alloy nanocubes, 1.5 mL of Na<sub>2</sub>PdCl<sub>4</sub> (20 mM), 0.5 mL of K<sub>2</sub>PtCl<sub>4</sub> (20 mM), 300 mg of NaI, and 160 mg of PVP were mixed with 10 mL of DMF in a 20 mL vial. After the vial had been capped, the mixture was ultrasonicated to get the homogeneous mixture. The mixture was transferred into a conventional oven and heated at 130 °C for 5 h before it was cooled to room temperature. The resulting colloidal products were collected by centrifugation and washed several times with an ethanol–DI water mixture.

### 2.2.3. Synthesis of Pd@Pt core–shell nanocubes

In a typical synthesis of Pd@Pt core–shell nanocubes, 1 mL of a suspension of the as-prepared Pd nanocubes was washed with DI water and re-dispersed in 1 mL of OAm. Then, 1 mL of the suspension of seed Pd nanocubes and 4 mL of OAm solution containing 100 mg of glucose (20 mg mL<sup>-1</sup>) and 5

mg of  $\text{H}_2\text{PtCl}_6 \cdot 6\text{H}_2\text{O}$  were added into a 30 mL vial, which connected with air through a syringe needle on the cap. The mixture was heated at 200 °C in an oil bath under magnetic stirring for 3 h, and then cooled down to room temperature. The final products were washed with mixture hexane–ethanol and finally dispersed in ethanol.

#### **2.2.4. Synthesis of Pd nanocubes**

In a typical synthesis of Pd nanocubes, 8.0 mL of an aqueous solution containing 105 mg of PVP, 60 mg of l-ascorbic acid, 270 mg of KBr, and 170 mg of KCl were placed in a 30 mL vial, and pre-heated in air under stirring at 100 °C for 10 min. Then, 3.0 mL of an aqueous solution containing 57 mg of  $\text{Na}_2\text{PdCl}_4$  was added. After the vial had been capped, the reaction was maintained to process at 100 °C for 3 h. The product was collected by centrifugation and washed several times with DI water.

#### **2.2.5. Synthesis of Pt nanocubes**

In a typical synthesis of Pt nanocubes, 20 mg of  $\text{Pt}(\text{acac})_2$  was dissolved in a mixed solvent containing 8 mL of OAm and 2 mL of OLA in water bath (60 °C) for 10 min, then dipped into oil bath which was preheated to 190 °C and stirred at 190 °C with a CO flow for 60 min. The resultant reaction mixture was then cooled down to room temperature. Pt nanocubes were precipitated out and washed twice with a mixture of toluene and ethanol. The precipitates were re-dispersed in ethanol.

#### **2.2.6. Preparation of the working electrodes**

All nanocubes were loaded onto a carbon support (Vulcan carbon XC-72) with a metal content of approximately 20%, relative to the total mass of Pd and/or Pt. To load the nanocubes onto the carbon support, a specific quantity of nanocubes and carbon support were dispersed in ethanol. Subsequently, the mixture was subjected to sonication for 5 h, followed by stirring overnight. Then, the carbon-supported metal nanocubes (catalyst/C) were collected via centrifugation, redispersed in 10 mL of acetic acid, and subjected to heating at 60 °C for 3 h to facilitate the removal of chemical species adsorbed onto the surface of the metal nanocubes. Finally, the catalyst/C was retrieved through centrifugation, rinsed six times with ethanol, and then dried overnight in an oven. For the preparation of catalyst inks, catalyst/C (2.5 mg), isopropyl alcohol (0.50 mL), and Nafion solution (10  $\mu\text{L}$ , 5 wt%) were added in deionized water (2.00 mL), followed by sonication for 30 min. In this study, a binder/ionomer, Nafion®

perfluorinated resin solution from Sigma-Aldrich, was employed. The commercial Pd/C and Pt/C (20 wt%) catalysts were sourced from Alfa Aesar. The procedure for preparing the commercial catalyst was also analogous to that of the metal nanocube catalyst, involving the formulation of a catalyst ink. For the preparation of the electrode, the glassy carbon electrode (GCE) was polished using 0.05  $\mu\text{m}$   $\text{Al}_2\text{O}_3$  and subsequently washed with deionized (DI) water before utilization. The GCE (diameter: 5 mm) featured a geometric area of 0.196  $\text{cm}^2$ . Subsequently, 10.0  $\mu\text{L}$  of the resultant catalyst ink was carefully deposited onto a GCE and allowed to dry within an oven. To ensure uniformity, we took measures to maintain a consistent total catalyst mass of 5.1  $\mu\text{g cm}^{-2}$  on the GC electrode.

### 2.2.7. Electrochemical measurement

Electrochemical measurements were carried out using a Bio-logic EC-Lab SP-300 in a three-electrode setup. The counter electrode was Pt wire, and the reference electrode was Hg/HgO (1 M NaOH). The GCE was used as a working electrode. The 0.1 M KOH and 0.5 M methanol were used as electrolyte and fuel for MOR experiment. All experiments were conducted at room temperature. The GCE was electrochemically cleaned through 50 potential cycles between  $-0.900$  and  $0.250$  V vs. Hg/HgO at a scan rate of  $50 \text{ mV s}^{-1}$  in 0.1 M KOH. The electrolyte solutions were purged with Ar-gas for 30 min before the experiments. For the MOR, CVs for all catalysts were recorded between  $-0.900$  and  $0.250$  V vs. Hg/HgO at a scan rate of  $50 \text{ mV s}^{-1}$  in both 0.1 M KOH and 0.1 M KOH + 0.5 M methanol. For stability testing using CAs, the potential was set at the oxidation peak potential of each catalyst and monitored for 5000 s. CO-stripping experiments involved saturating the catalyst-loaded GCE surface with CO by purging CO gas in 0.1 M KOH while maintaining the working electrode at  $-0.3$  V vs. Hg/HgO for 15 min. Then, CO dissolved in the electrolyte was removed by purging with Ar-gas for 40 min. CO-stripping experiments were carried out between  $-0.900$  and  $0.250$  V vs. Hg/HgO at a scan rate of  $50 \text{ mV s}^{-1}$ . Electrochemically active surface area (ECSA) was determined using the equation:  $\text{ECSA} = Q_0/q_0$ , where  $Q_0$  represents the surface charge from the area below the oxygen reduction CV curve, and  $q_0$  is associated with the charge required for the oxygen monolayer reduction on Pd ( $420 \mu\text{C cm}^{-2}$ ) and Pt ( $424 \mu\text{C cm}^{-2}$ ).



### **2.2.8. Characterization**

Transmission Electron Microscopy (TEM) and Scanning Electron Microscopy (SEM) images of the prepared Pd–Pt alloy, Pd@Pt core–shell, Pd, and Pt nanocubes were obtained on Jeol JEM-2100F and Jeol JEM-7210F, respectively. Inductively coupled plasma-optical emission spectrometry (ICP-OES) measurement was carried out using a Spectroblue-ICP-OES (Ametek). X-ray diffraction (XRD) measurements were conducted on a Rigaku D/MAX2500V/PC scanning for  $2\theta$  at 30 to 90°. X-ray photoelectron spectroscopy (XPS) measurements were conducted on a Thermo-Fisher K-alpha. SEM analysis were done using instruments at total-period analysis center for Ulsan chemical industry of the Korea Basic Science Institute (KBSI).

## 2.3. Result and Discussion

### 2.3.1. Synthesis and characterization of the nanocubes

The nanocubes with different compositional structures of Pd and Pt were synthesized using a wet-chemical synthesis method, following the previously reported procedure with a slight modification.<sup>38–41</sup> The Pd–Pt alloy nanocubes were synthesized by co-reduction of Pd and Pt precursors in a reaction mixture containing NaI, PVP, and DMF, respectively, following the previous reported.<sup>40</sup> On the other hand, the synthesis of bimetallic Pd@Pt core–shell nanocubes was accomplished through epitaxial growth of the Pt shell on the pre-synthesized Pd nanocubes with an edge length greater than 8 nm.<sup>41</sup> The utilization of different chemicals and reaction temperature enables the formation of {100}-faceted nanocubes with different atomic distribution by providing optimal Pd and Pt growth rate. SEM images in **Figure 2.1.** depict the prepared nanocubes, highlighting their uniform cubic morphology and similar sizes across different samples.

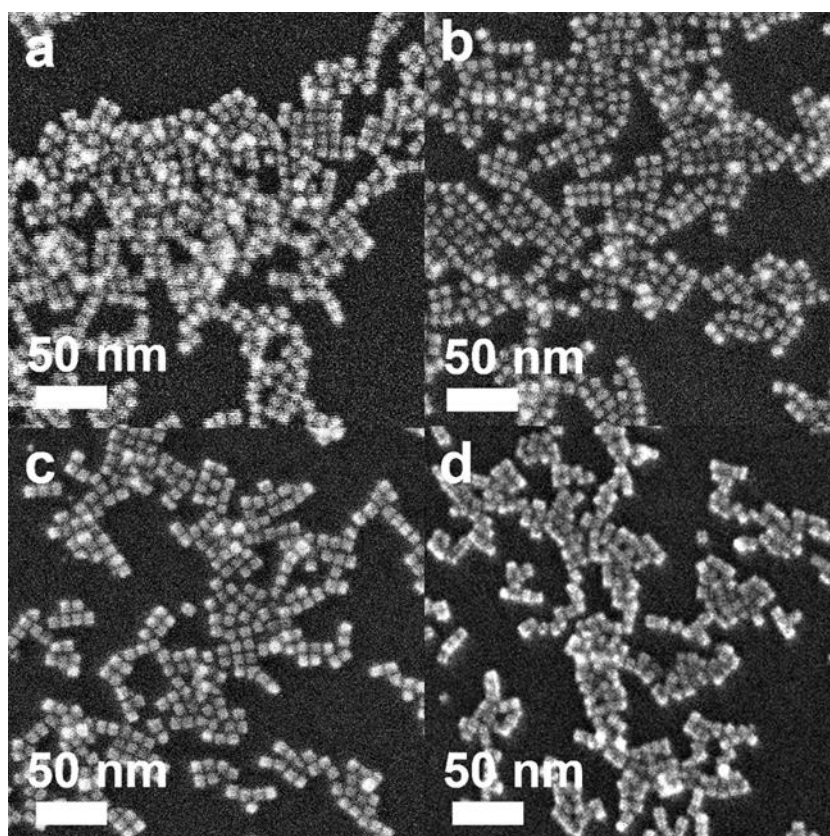


**Figure 2.1.** The SEM images of (a) Pd-Pt alloy, (b) Pd@Pt core-shell, (c) Pd, and (d) Pt nanocubes.

TEM images of the products further confirm the well-defined cubic shape of the products, with average edge lengths of  $8.4 \pm 1.6$  nm,  $9.2 \pm 1.6$  nm,  $8.3 \pm 1.4$  nm, and  $8.7 \pm 1.1$  nm for Pd–Pt alloy, Pd@Pt, Pd, and Pt nanocubes, respectively (**Figure 2.2.a–i**). The adjacent lattice fringes of all nanocubes exhibit d-spacings around 0.194–0.196 nm, corresponding to the (200) planes of face-centered cubic (fcc) Pd–Pt alloy, Pd, and Pt. This confirms the successful formation of identical (100) faceted nanocubes (**Figure 2.2.f–i**). Furthermore, the highly crystalline nature of the prepared nanocubes was confirmed by the fast Fourier transform (FFT) patterns obtained from a single Pd–Pt alloy, Pd@Pt, Pd, and Pt nanocubes (inset in **Figure 2.2.f–i**). To investigate the compositional structure of the Pd–Pt bimetallic nanocubes, including Pd–Pt alloy and Pd@Pt nanocubes, High-Angle Annular Dark-Field Scanning Transmission Electron Microscopy-Energy Dispersive X-ray Spectroscopy (HAADF-STEM-EDS) measurements were conducted. **Figure 2.2.j** exhibit the uniform distribution of Pd and Pt signals throughout the entire nanocube, indicating the successful formation of the Pd–Pt alloy compositional structure. The Pd/Pt atomic ratio in the Pd–Pt alloy nanocubes, measured using EDS and ICP-OES measurements, was determined to be 3 : 1. In contrast, the HAADF-STEM-EDS images shown in **Figure 2.2.k** show that Pd signals are predominantly observed in the core region, while Pt signals are clearly detected in the surface shell region, demonstrating the successful formation of Pd@Pt core–shell nanocubes. The Pd/Pt atomic ratio in the Pd@Pt core–shell nanocubes, as determined by EDS and ICP-OES measurements, was also found to be 3 : 1, matching the ratio observed in the Pd–Pt alloy nanocubes.

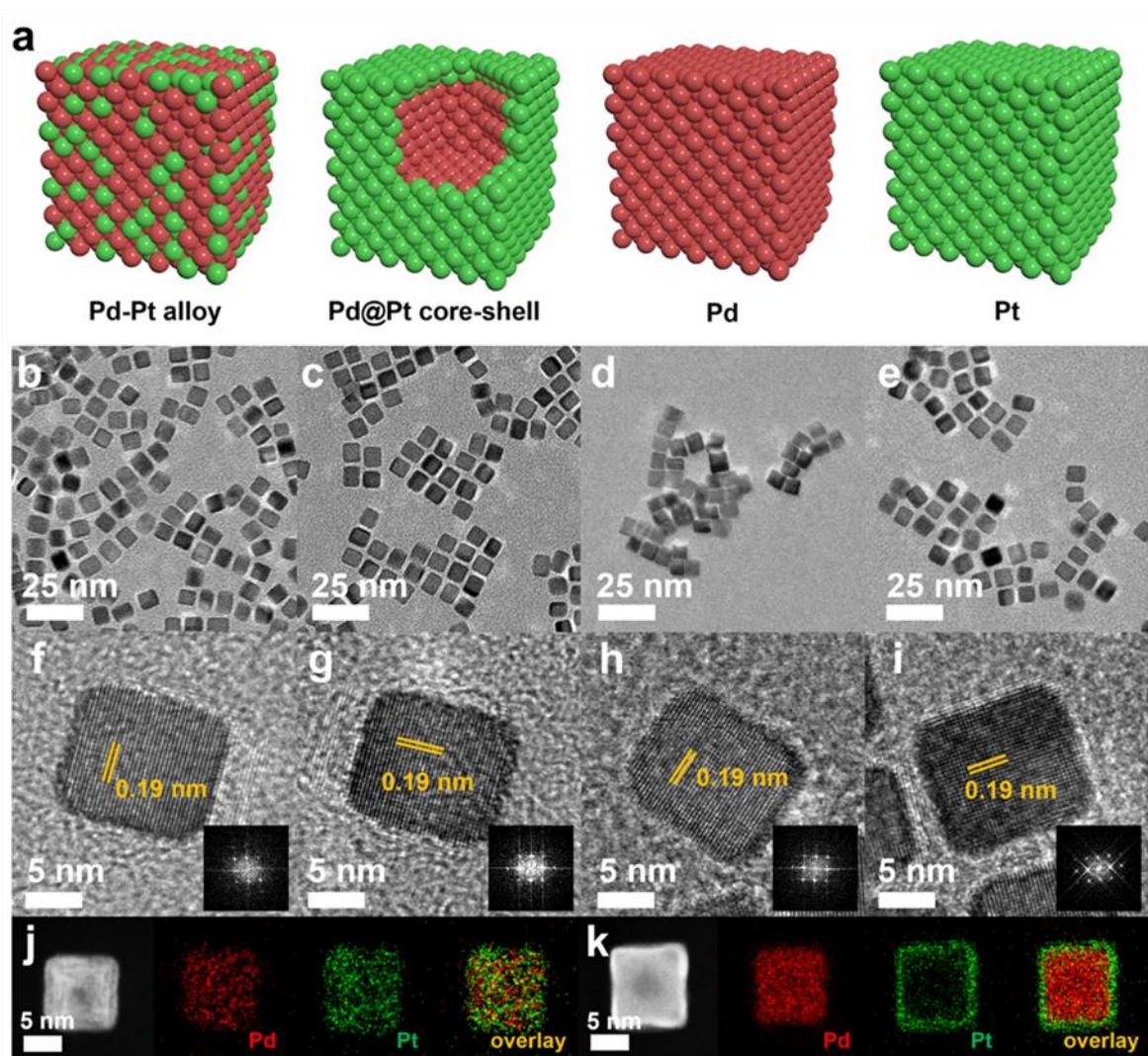


**Figure 2.2.** Structure characterization of bimetallic Pd-Pt alloy, Pd@Pt core-shell, Pt and Pd nanocubes. (a) geometric illustration, (b-e) TEM, and (f-i) HR-TEM images including the correspond FFT images. HAADF-STEM images and corresponding EDS elemental mapping analysis of (j) Pd-Pt alloy and (k) Pd@Pt core-shell nanocubes.

The crystal structures of the nanocubes were investigated using XRD patterns. **Figure 2.3.a** displays the XRD patterns of the nanocubes, revealing all the nanocubes possess characteristic diffraction peaks corresponding to the fcc crystal structure. Comparing the diffraction peak positions, pure Pt nanocubes exhibit slightly negative-shifted peak positions compared to those of Pd nanocubes, which can be attributed to the slightly larger atomic size of Pt atoms compared to Pd atoms.<sup>42-44</sup> The lattice distance from XRD pattern also well-match with the TEM images that four different types of Pd-Pt nanocubes. In the case of the Pd-Pt alloy and Pd@Pt core-shell nanocubes, the diffraction peak positions are

located between those of pure Pt and Pd nanocubes. This observation further supports their Pd–Pt bimetallic nature, indicating the successful formation of the Pd–Pt alloy and Pd@Pt core–shell compositional structures. To investigate the surface composition and chemical states of the nanocubes, XPS analysis was conducted (Figure 2.3b, c, Table 2.1 and 2.2). In the XPS spectra of the Pt 4f core levels, the binding energies of 71.36 and 74.72 eV were observed for the Pd–Pt alloy nanocubes, corresponding to Pt 4f<sub>7/2</sub> and 4f<sub>5/2</sub>, respectively. These positions are negatively shifted compared to those of the Pd@Pt core–shell (71.39 and 74.79 eV) and Pt nanocubes (71.58 and 75.00 eV) (**Figure 2.3.b**). The Pt 4f binding energy order of the nanocubes follows the sequence: Pt nanocubes > Pd@Pt core–shell nanocubes > Pd–Pt alloy nanocubes. The binding energies of Pd 3d<sub>5/2</sub> and 3d<sub>3/2</sub> for the Pd–Pt alloy nanocubes (335.88 and 341.17 eV) shifted to higher values compared to those of the Pd@Pt core–shell (335.85 and 341.12 eV) and Pd nanocubes (335.76 and 341.08 eV) (Figure 2.3c). These XPS results indicate the electron transfer from Pd to Pt in both bimetallic Pd–Pt alloy and Pd@Pt core–shell nanocubes. Furthermore, the subtle differences in binding energies between the Pd–Pt alloy nanocubes and Pd@Pt core–shell nanocubes indicate distinct interplay between Pd and Pt atoms, which is contingent upon the compositional structure. These findings emphasize that despite having an identical Pd/Pt atomic ratio, the Pd–Pt alloy and Pd@Pt core–shell nanocubes exhibit different electronic structures, leading to unique electrocatalytic properties.

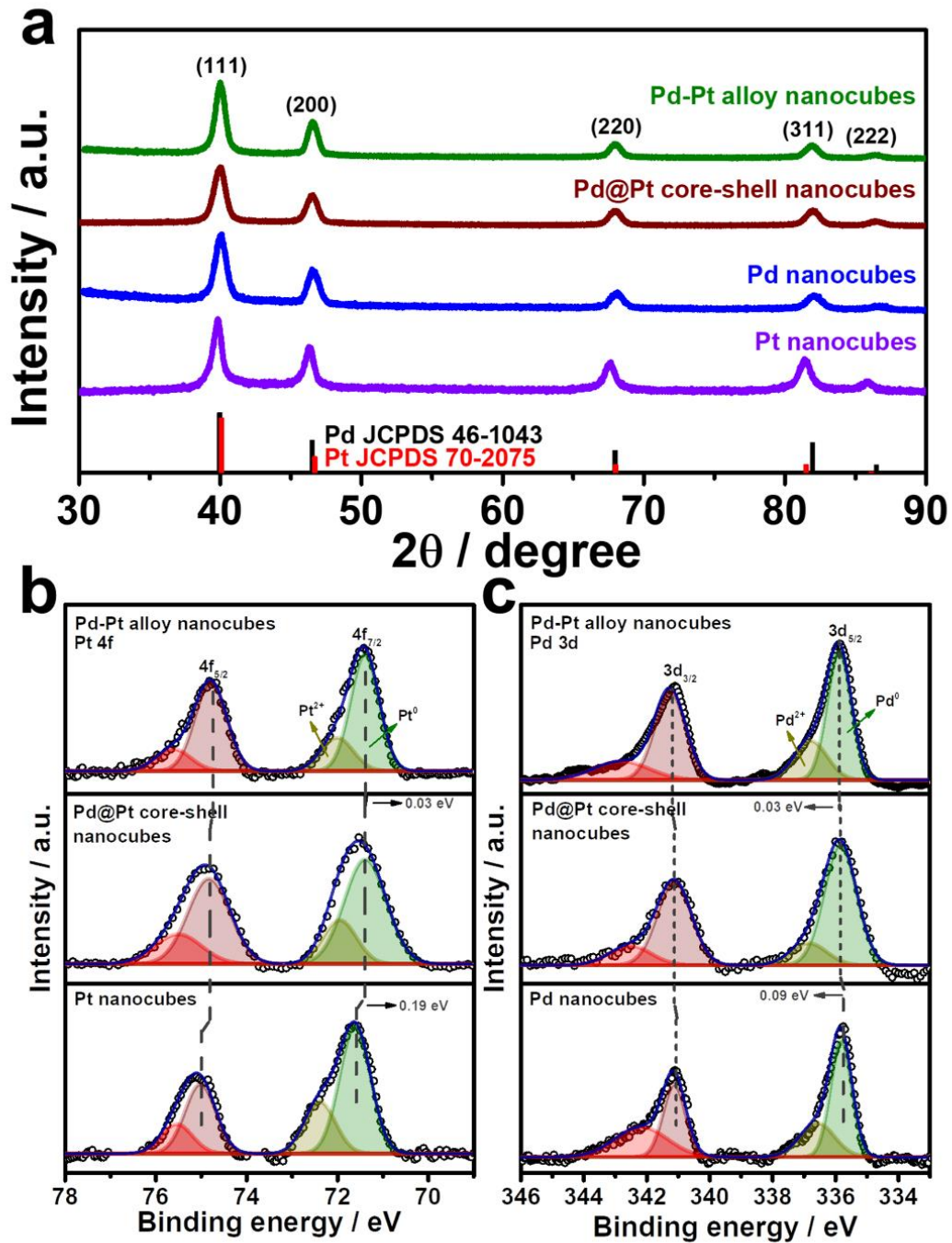


**Figure 2.3.** (a) XRD patterns of bimetallic Pd-Pt alloy, Pd@Pt core-shell, monometallic Pd and Pt nanocubes. The red and black bars are referred to Pt and Pd JCPDS card, respectively. XPS spectra of (b) Pd 3d and (c) Pt 4f of bimetallic Pd-Pt alloy, Pd@Pt core-shell, Pd, and Pt nanocubes, respectively.

**Table 2.1.** XPS spectra of Pt 4f core levels for nanocubes with different atomic distribution.

| Catalyst         | Pt 4f <sub>5/2</sub> |                 | Pt 4f <sub>7/2</sub> |                 |
|------------------|----------------------|-----------------|----------------------|-----------------|
|                  | Pt <sup>2+</sup>     | Pt <sup>0</sup> | Pt <sup>2+</sup>     | Pt <sup>0</sup> |
| PdPt alloy       | 75.51 eV             | 74.72 eV        | 71.99 eV             | 71.36 eV        |
| Pd@Pt core-shell | 75.52 eV             | 74.79 eV        | 71.92 eV             | 71.39 eV        |
| Pt               | 75.55 eV             | 75.00 eV        | 72.37 eV             | 71.58 eV        |
| Pd               | -                    | -               | -                    | -               |

**Table 2.2.** XPS spectra of Pd 3d core levels for nanocubes with different atomic distribution.

| Catalyst         | Pd 3d <sub>3/2</sub> |                 | Pd 3d <sub>5/2</sub> |                 |
|------------------|----------------------|-----------------|----------------------|-----------------|
|                  | Pd <sup>2+</sup>     | Pd <sup>0</sup> | Pd <sup>2+</sup>     | Pd <sup>0</sup> |
| PdPt alloy       | 342.90 eV            | 341.17 eV       | 336.76 eV            | 335.88 eV       |
| Pd@Pt core-shell | 342.57 eV            | 341.12 eV       | 336.90 eV            | 335.85 eV       |
| Pd               | 342.18 eV            | 341.08 eV       | 336.48 eV            | 335.76 eV       |
| Pt               | -                    | -               | -                    | -               |

### 2.3.2 Electrocatalytic MOR performance

To examine the influence of compositional structure on the electrocatalytic reaction, the catalytic performances of the prepared Pd–Pt alloy, Pd@Pt core–shell, Pd, and Pt nanocubes were evaluated for MOR and compared with those of commercial Pd/C and Pt/C catalysts. Cyclic voltammograms (CVs) of the Pd–Pt alloy, Pd@Pt core–shell, Pd, and Pt nanocubes were obtained in a three-electrode system using a scan rate of 50 mV s<sup>-1</sup> in 0.1 M KOH electrolyte (**Figure 2.4.a**). The catalysts displayed the hydrogen adsorption/desorption peak within the range of -0.9 to -0.6 V vs. Hg/HgO, along with the metal oxide reduction peak spanning -0.45 to 0.0 V vs. Hg/HgO (**Figure 2.4.a**).<sup>45–47</sup> Compared with Pd nanocubes and Pd/C, the catalysts containing Pt surface atoms such as Pd–Pt alloy, Pd–Pt alloy nanocubes, Pd@Pt nanocubes, Pt nanocubes, and Pt/C exhibited metal oxide reduction peak at more positive potential.<sup>48,49</sup>

The ECSAs of the catalysts were calculated from the oxygen species desorption regions in the CVs. The ECSAs of the Pd–Pt alloy, Pd@Pt core–shell, Pd, and Pt nanocubes were determined to be 25.9, 24.4, 25.3, and 24.7 m<sup>2</sup> g<sup>-1</sup>, respectively (**Figure 2.4.b**). The similar ECSAs of the nanocubes can be attributed to their comparable sizes, enabling investigation of the compositional effect on electrocatalytic activity independent of surface area. The ECSAs of the Pd/C and Pt/C catalysts were 34.9 and 38.1 m<sup>2</sup> g<sup>-1</sup>, respectively, reflecting their smaller sizes (**Figure 2.4.b**). **Figure 4.c** and **d** shows the CVs of MOR obtained using the different catalysts in 0.1 M KOH solution containing 0.5 M methanol. The current measured in the CVs was normalized to the mass of the catalysts loaded on the GCE and the ECSA, representing the mass activity and specific activity, respectively. The Pd–Pt alloy nanocubes exhibit the highest mass activity, with a value of 3070 mA mg<sup>-1</sup>, which is 1.5, 2.5, 2.2, 6.3, and 3.0 times higher than the those of the Pd@Pt core–shell nanocubes (2030 mA mg<sup>-1</sup>), Pd nanocubes (1210 mA mg<sup>-1</sup>), Pt nanocubes (1380 mA mg<sup>-1</sup>), Pd/C (490 mA mg<sup>-1</sup>), and Pt/C (1040 mA mg<sup>-1</sup>) catalysts, respectively (**Figure 2.4.c** and **e**). Despite the lower mass activity compared to the Pd–Pt alloy nanocubes, the Pd@Pt core–shell nanocubes exhibit 1.7 and 1.5 times higher mass activity compared to pure Pd and Pt nanocubes, respectively. In addition, a similar trend across the catalysts was also observed in the specific activity (**Figure 2.4.d** and **e**). These results demonstrate the positive effect by



combination of Pd–Pt bimetallic composition. Moreover, the higher MOR activities observed in all the nanocubes compared to commercial Pt/C and Pd/C indicate that the {100} surfaces of both Pt and Pd are more effective for electrochemical methanol oxidation than the mixed surface of commercial Pt/C and Pd/C catalysts.<sup>15,50–53</sup>

To assess the stability of these catalysts, chronoamperometry (CA) curves of all nanocubes were obtained and compared with those of Pd/C and Pt/C catalysts. As shown in **Figure 2.4.f**, the current densities of monometallic catalysts such as Pd nanocubes, Pt nanocubes, Pd/C, and Pt/C rapidly dropped and their current densities were 108, 168, 16, and 51 mA mg<sup>-1</sup> after 5000 s, respectively, suggesting the poor MOR stabilities. In contrast, the current density of Pd–Pt alloy and Pd@Pt core–shell nanocubes could maintain above 521 and 256 mA mg<sup>-1</sup> after 5000 s, respectively. Notably, Pd–Pt alloy nanocubes exhibited superior stability for MOR compared to Pd@Pt core–shell nanocubes. To check the excellent stability of the Pd–Pt alloy nanocubes, morphology and composition changes were investigated using TEM measurements.

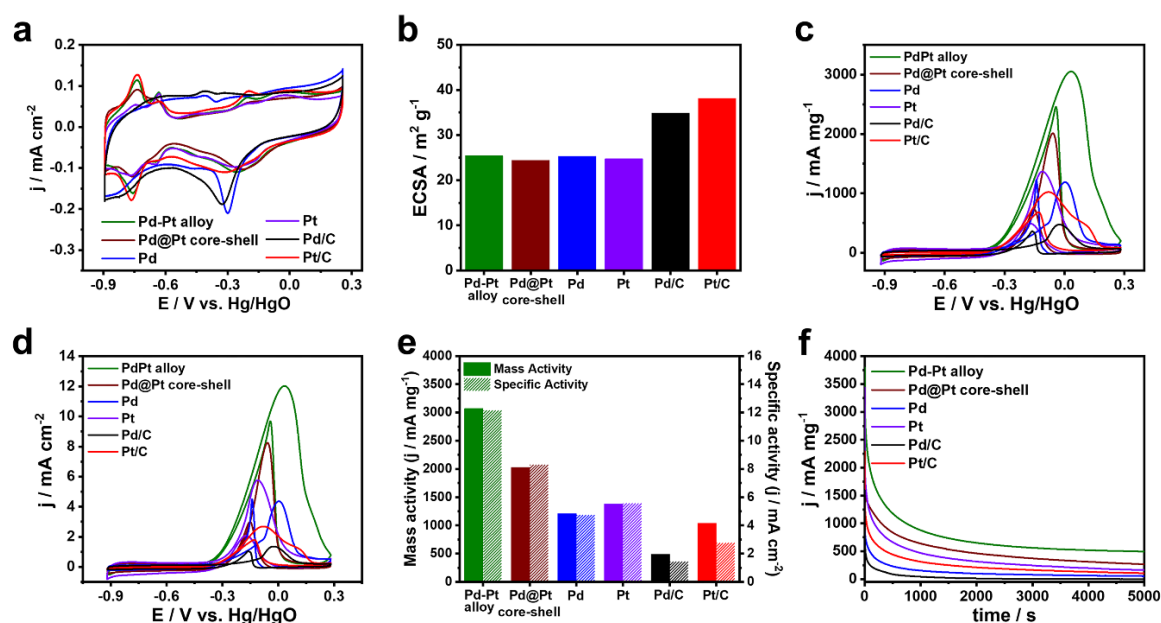


**Figure 2.4.** Electrocatalytic MOR properties of bimetallic Pd-Pt alloy, Pd@Pt core-shell, monometallic Pt and Pd nanocubes, including commercial Pt/C and Pd/C in 0.1 M KOH and 0.5 M MeOH at 50 mV s<sup>-1</sup>. (a) CVs curves in 0.1 M KOH and ECSAs of different catalysts. (c) Mass-normalized and (d) ECSA-normalized CV curves of different catalysts. (e) Mass activity and specific activity of different catalysts. (f) CA curves of different catalysts for 5000 s.

A TEM image shown in **Figure 2.5.a** demonstrates that the morphology of the Pd–Pt alloy nanocubes is preserved even after the stability test. Furthermore, the Pd/Pt atomic ratio, as determined through EDS analysis, maintained a high degree of similarity to its initial value of 3 : 1 throughout the experiment, with a measured ratio of 75.81 : 24.19. In contrast, aggregated morphology of Pt/C after stability test was observed in TEM image (**Figure 2.5.b**). These results provide evidence that the sustained activity of the Pd–Pt alloy nanocubes can be attributed to the preservation of their structural and compositional integrity.

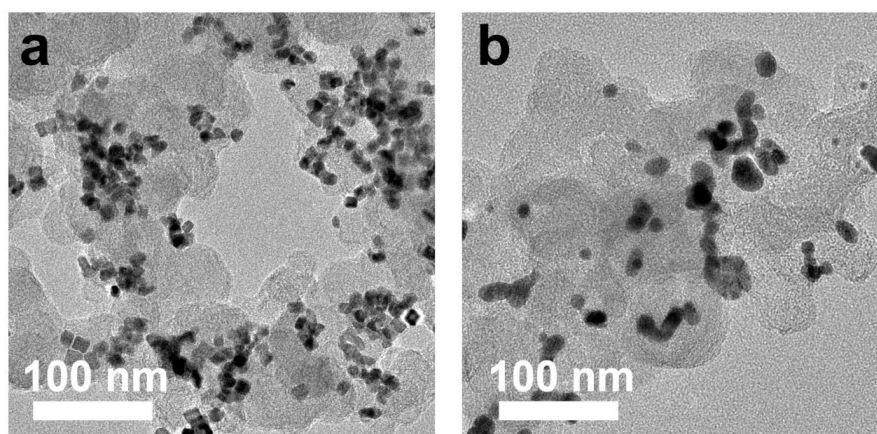
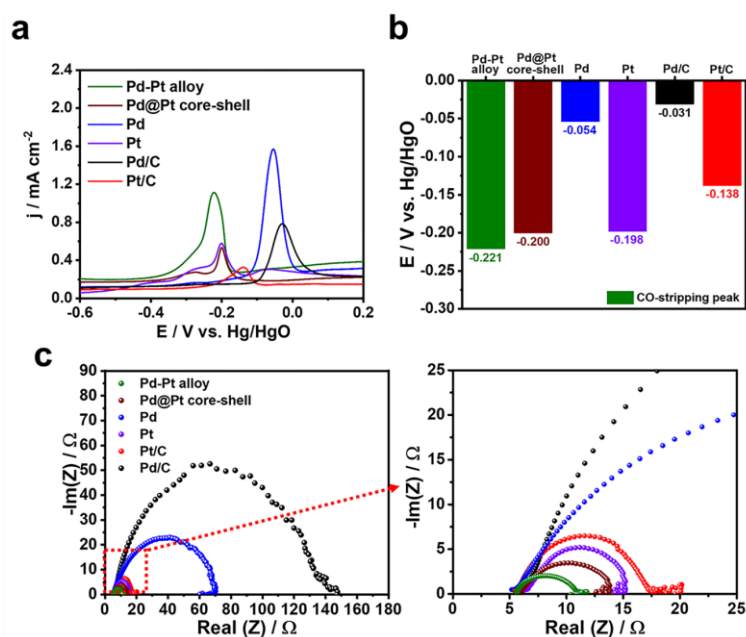


**Figure 2.5.** The TEM images of (a) Pd-Pt alloy nanocubes and (b) Pt/C after CAs test.

To gain insights into the substantial enhancement in the MOR performance of the Pd–Pt alloy nanocubes compared to the Pd@Pt core–shell nanocubes and other monometallic catalysts, a CO stripping experiment was conducted. This experiment was performed because the strong bonding between the catalyst surface and CO, which is generated during electrochemical methanol oxidation, can hinder MOR by blocking the adsorption of methanol on catalyst active sites. Hence, an efficient MOR catalyst should have the ability to efficiently remove or scavenge the CO adsorbed on the catalyst surface. In **Figure 2.6.a** and **b**, the bimetallic Pd–Pt alloy and Pd@Pt core–shell nanocubes exhibited a maximum current potential of  $-0.221$  and  $-0.200$  V, respectively, for the oxidative elimination of CO to CO<sub>2</sub>. These maximum current potentials were observed at more negative potentials compared to those of the Pt nanocubes ( $-0.198$  V), Pd nanocubes ( $-0.054$  V), Pt/C ( $-0.138$  V), and Pd/C ( $-0.031$  V), respectively (**Figure 2.6.a** and **b**). Importantly, the higher CO removal capability of the Pd–Pt alloy nanocubes compared to that of the Pd@Pt core–shell nanocubes, as well as other catalysts, can account for their

enhanced MOR activity and stability. Furthermore, the electrochemical resistant of the catalysts measured by electrochemical impedance spectroscopy (EIS) analysis. In **Figure 2.6.c**, it can be observed that bimetallic Pd–Pt nanocubes, including Pd–Pd alloy and Pd@Pt core–shell nanocubes, exhibited smaller arc radius compared to monometallic Pd or Pt catalysts. This finding indicates that the formation of a Pd–Pt bimetallic compositional structure is advantageous in enhancing their electron transfer ability compared to monometallic Pd or Pt compositions. Notably, smaller arc radius of Pd–Pd alloy nanocubes compared to Pd@Pt core–shell nanocubes implies the Pd–Pt alloy is more efficient than Pd@Pt core–shell structure to transfer electron. Consequently, the enhanced MOR activity and stability of the Pd–Pt alloy nanocubes, compared to the Pd@Pt core–shell nanocubes and monometallic Pd or Pt catalysts, can be attributed to their superior abilities in CO removal and electron transfer.

**Figure 2.6.** (a) CO-stripping measurements of different catalysts and (b) corresponding maximum current potentials. (c) Nyquist plots of different catalysts in 0.1 M KOH at 50 mV s<sup>-1</sup>.



## 2.4. Conclusion

In conclusion, we have successfully demonstrated that the electrocatalytic activity of Pd–Pt based nanocubes for the MOR is intricately tied to the atomic distribution of Pd and Pt. This has been accomplished through a meticulous investigation involving Pd–Pt alloy, Pd@Pt core–shell, Pt, and Pd nanocubes. Notably, in comparison to Pd@Pt core–shell, Pt, and Pd nanocubes with monometallic surfaces, the Pd–Pt alloy nanocubes showed significantly enhanced catalytic activity, achieving an impressive mass (specific) activity of approximately  $3070 \text{ mA mg}^{-1}$  ( $12.17 \text{ mA cm}^{-2}$ ). Furthermore, the stability of the Pd–Pt alloy nanocubes was superior to that of Pd@Pt core–shell, Pt, and Pd nanocubes. The exceptional electrocatalytic activity and stability of the Pd–Pt alloy nanocubes can be ascribed to their adeptness at CO removal and the modification of surface electronic structure, a consequence of the interplay between Pd and Pt within the alloy phase. These findings hold promise for applications in other electrochemical systems, with potential for even further enhancement of catalytic performance through the strategic manipulation of atomic distribution in nanostructures.

## References

1. L. Luo, Z. Tan, C. Fu, R. Xue, X. Cheng, T. Bi, L. Zhao, Y. Guo, X. Cai, J. Yin, S. Shen and J. Zhang, *Chem. Eng. J.*, **2023**, 451, 138786.
2. D. T. Lestarini and J. W. Hong, *Appl. Surf. Sci.*, **2023**, 610, 155311.
3. M. Simões, S. Baranton and C. Coutanceau, *Appl. Catal., B*, **2010**, 93, 354–362.
4. K. Eid, Y. H. Ahmad, S. Y. AlQaradawi and N. K. Allam, *Catal. Sci. Technol.*, **2017**, 7, 2819–2827.
5. T.-P. Wang, B.-D. Hong, Y.-M. Lin and C.-L. Lee, *Appl. Catal., B*, **2020**, 260, 118140.
6. H. Ahn, H. Ahn, J. An, H. Kim, J. W. Hong and S. W. Han, *Nano Lett.*, **2022**, 22, 9115–9121.
7. H. J. Kim, C. J. Moon, S. Lee, J. Theerthagiri, J. W. Hong, M. Y. Choi and Y. W. Lee, *J. Mater. Sci. Technol.*, **2023**, 165, 153–160.
8. D. Jin, Y. Lee, I. Y. Kim, C. Lee and M. H. Kim, *J. Mater. Chem. A*, **2023**, 11, 16243–16254.
9. H. Wahidah and J. W. Hong, *Bull. Korean Chem. Soc.*, **2022**, 43, 1111–1117.
10. J. Li, Z. Luo, Y. Zuo, J. Liu, T. Zhang, P. Tang, J. Arbiol, J. Llorca and A. Cabot, *Appl. Catal., B*, **2018**, 234, 10–18.
11. X. Cui, P. Xiao, J. Wang, M. Zhou, W. Guo, Y. Yang, Y. He, Z. Wang, Y. Yang, Y. Zhang and Z. Lin, *Angew Chem. Int. Ed. Engl.*, **2017**, 56, 4488–4493.
12. C. Li, N. Clament Sagaya Selvam and J. Fang, *Nano-Micro Lett.*, **2023**, 15, 83.
13. C. Y. Ahn, J. E. Park, S. Kim, O. H. Kim, W. Hwang, M. Her, S. Y. Kang, S. Park, O. J. Kwon, H. S. Park, Y. H. Cho and Y. E. Sung, *Chem. Rev.*, **2021**, 121, 15075–15140.
14. B. W. Zhang, H. L. Yang, Y. X. Wang, S. X. Dou and H. K. Liu, *Adv. Energy Mater.*, **2018**, 8, 1703597.
15. Y. X. Xiao, J. Ying, G. Tian, X. Q. Zhang, C. Janiak, K. I. Ozoemena and X. Y. Yang, *Chem. Commun.*, **2021**, 57, 986–989.
16. S. Y. Ma, H. H. Li, B. C. Hu, X. Cheng, Q. Q. Fu and S. H. Yu, *J. Am. Chem. Soc.*, **2017**, 139, 5890–5895.
17. B. Y. Xia, H. B. Wu, X. Wang and X. W. Lou, *J. Am. Chem. Soc.*, **2012**, 134, 13934–13937.
18. S. Du, *Engineering*, **2021**, 7, 33–49.
19. Y. Qi, M. A. Sadi, D. Hu, M. Zheng, Z. Wu, Y. Jiang and Y. P. Chen, *Adv. Mater.*, **2023**, 35, e2205714.
20. J. Rajendran, *J. Hazard. Mater.*, **2023**, 449, 130979.
21. W. Kong, J. Deng and L. Li, *J. Mater. Chem. A*, **2022**, 10, 14674–14691.
22. Ş. Neaţu, F. Neaţu, I. M. Chirica, I. Borbáth, E. Tálas, A. Tompos, S. Somacescu, P. Osiceanu, M. A.

- Folgado, A. M. Chaparro and M. Florea, *J. Mater. Chem. A*, **2021**, 9, 17065–17128.
23. Q. Chang, Y. Hong, H. J. Lee, J. H. Lee, D. Ologunagba, Z. Liang, J. Kim, M.J. Kim, J. W. Hong, L. Song, S. Kattel, Z. Chen, J. G. Chen and S. I. Choi, *Proc. Natl. Acad. Sci. U. S. A.* **2022**, 119, e2112109119.
24. Philip and A. Ruban Kumar, *Renewable Sustainable Energy Rev.*, **2023**, 182, 113423.
25. S. Yanik, D. Emre, M. Alp, F. Algi, S. Yilmaz, A. Bilici and D. Ozkan-Ariksoysal, *J. Pharm. Biomed. Anal.*, **2023**, 234, 115524.
26. H. Xu, H. Shang, C. Wang and Y. Du, *Adv. Funct. Mater.*, **2020**, 30, 2000793.
27. Q. F. Li, X. Chen, H. Wang, M. Liu and H. L. Peng, *ACS Appl. Mater. Interfaces*, **2023**, 15, 13290–13298.
28. W. Wang, X. Chen, X. Zhang, J. Ye, F. Xue, C. Zhen, X. Liao, H. Li, P. Li, M. Liu, Q. Kuang, Z. Xie and S. Xie, *Nano Energy*, **2020**, 71, 104623.
29. H. Lv, X. Chen, D. Xu, Y. Hu, H. Zheng, S. L. Suib and B. Liu, *Appl. Catal., B*, **2018**, 238, 525–532.
30. J. W. Hong, S. W. Kang, B.-S. Choi, D. Kim, S. B. Lee and S. W. Han, *ACS Nano*, **2012**, 6, 2410–2419.
31. Z. Wang, S. Hu, A. Ali, H. Chen and P. K. Shen, *ACS Appl. Energy Mater.*, **2021**, 4, 1085–1092.
32. L. N. Zhou, X. T. Zhang, Z. H. Wang, S. Guo and Y. J. Li, *Chem. Commun.*, **2016**, 52, 12737–12740.
33. X. Chen, Z. Cai, X. Chen and M. Oyama, *Carbon*, **2014**, 66, 387–394.
34. H. C. Kim, R. K. Pramadewandaru, S. U. Lee and J. W. Hong, *Bull. Korean Chem. Soc.*, **2020**, 41, 237–240.
35. F. Zhan, T. Bian, W. Zhao, H. Zhang, M. Jin and D. Yang, *CrystEngComm*, **2014**, 16, 2411–2416.
36. W. Wang, Q. Huang, J. Liu, Z. Zou, M. Zhao, W. Vogel and H. Yang, *J. Catal.*, **2009**, 266, 156–163.
37. J. J. De la Cruz-Cruz, M. A. Domínguez-Crespo, E. Ramírez-Meneses, A. M. Torres-Huerta, S. B. Brachetti-Sibaja, N. Cayetano-Castro and H. J. Dorantes-Rosales, *Int. J. Hydrogen Energy*, **2020**, 45, 4570–4586.
38. B. Wu, N. Zheng and G. Fu, *Chem. Commun.*, **2011**, 47, 1039–1041.
39. M. Jin, H. Liu, H. Zhang, Z. Xie, J. Liu and Y. Xia, *Nano Res.*, **2010**, 4, 83–91.
40. X. Huang, Y. Li, Y. Li, H. Zhou, X. Duan and Y. Huang, *Nano Lett.*, **2012**, 12, 4265–4270.
41. X. Li, Q. Chen, M. Wang, Z. Cao, Q. Zhan, T. He, Q. Kuang, Y. Yin and M. Jin, *J. Mater. Chem. A*, **2016**, 4, 13033–13039.
42. M. Censabella, V. Torrisi, S. Boninelli, C. Bongiorno, M. G. Grimaldi and F. Ruffino, *Appl. Surf. Sci.*, **2019**, 475, 494–503.
43. G. Zhang, C. Huang, R. Qin, Z. Shao, D. An, W. Zhang and Y. Wang, *J. Mater. Chem. A*, **2015**, 3, 5204–

5211.

44. Z. Liu, L. Hong, M. P. Tham, T. H. Lim and H. Jiang, *J. Power Sources*, **2006**, 161, 831–835.
45. J. Chang, G. Wang, C. Li, Y. He, Y. Zhu, W. Zhang, M. Sajid, A. Kara, M. Gu and Y. Yang, *Joule*, **2023**, 7, 587–602.
46. Y. Zhang, G. Shu, Z. Shang, K. Ma, L. Song, C. Wang, C.-A. Zhou and H. Yue, *ACS Sustain. Chem. Eng.*, **2023**, 11, 8958–8967.
47. J. Li, S. Ghoshal, M. K. Bates, T. E. Miller, V. Davies, E. Stavitski, K. Attenkofer, S. Mukerjee, Z. F. Ma and Q. Jia, *Angew Chem. Int. Ed. Engl.*, **2017**, 56, 15594–15598.
48. Sathyaseelan, V. Elumalai, K. Krishnamoorthy, A. Sajeev and S.-J. Kim, *ACS Sustainable Chem. Eng.*, **2023**, 11, 5345–5355.
49. W. Du, K. E. Mackenzie, D. F. Milano, N. A. Deskins, D. Su and X. Teng, *ACS Catal.*, **2012**, 2, 287–297.
50. L. Sahoo and U. K. Gautam, *ACS Appl. Nano Mater.*, **2020**, 3, 8117–8125.
51. H. J. Kim, B. Ruqia, M. S. Kang, S. B. Lim, R. Choi, K. M. Nam, W. S. Seo, G. Lee and S. I. Choi, *Sci. Bull.*, **2017**, 62, 943–949.
52. Y.-W. Lee, J.-Y. Lee, D.-H. Kwak, E.-T. Hwang, J. I. Sohn and K.-W. Park, *Appl. Catal., B*, **2015**, 179, 178–184.
53. Y. Kim, Y. W. Lee, M. Kim and S. W. Han, *Chem. – Eur. J.*, **2014**, 20, 7901–7905.

## **Chapter 3. Highly Enhanced Electrocatalytic Performances with Dendritic Bimetallic Palladium-Based Nanocrystals**

### **3.1. Introduction**

The preparation of metal nanocrystals (NCs) is significant for the development of efficient catalysts for various promising electrochemical reactions.<sup>1,2</sup> In particular, controlling the shape, size, and composition of metal NCs can allow the interaction of target molecules with the surface of NCs to be optimized, resulting in the enhancement of catalytic performances.<sup>3-5</sup> Recently, porous NCs have attracted an enormous amount of interest due to their enhanced catalytic performances, attributable to their large surface areas.<sup>6,7</sup> Among various porous metal NCs, dendritic NCs with many highly porous branches have attracted much attention for their morphological benefits, such as high volume-to-surface area, efficient mass transport, and many unsaturated surface atoms in their branches, which can promote the conversion of molecules for various electrochemical reactions.<sup>8-11</sup>

Along with the shape of noble metal NCs, controlling the composition of the NCs is effective in enhancing their catalytic performance. The incorporation of secondary metals into monometallic NCs can influence the adsorption strength of reagents and form an intermediate by changing the electronic structures of active surface metal atoms.<sup>12-16</sup> In addition, some bimetallic NCs can remove poisoning intermediates bound on active surface atoms, and bimetallic NCs with controlled compositions have shown enhanced electrocatalytic performance compared with monometallic NCs.<sup>17-19</sup> In particular, Pd–Pt bimetallic NCs constructed by precise shape and composition engineering have exhibited remarkable electrocatalytic activities towards various electrochemical reactions, including the methanol oxidation reaction (MOR) and hydrogen evolution reaction (HER).<sup>20-24</sup> Based on these previous findings, it can be anticipated that using Pd–Pt bimetallic nanodendrites (NDs) with a small size is a desirable approach for the development of efficient electrocatalysts for various electrochemical reactions.

In this work, we report wet chemical synthesis for the preparation of Pd–Pt bimetallic NDs with controllable sizes. Pd–Pt alloy NDs were produced by the co-reduction of Na<sub>2</sub>PdCl<sub>4</sub> and K<sub>2</sub>PtCl<sub>4</sub> in the presence of cetyltrimethylammonium chloride (CTAC) and ascorbic acid (AA), used as stabilizers and reducing agents, respectively. CTAC and AA are critical in creating the well-defined dendritic shape



and compositional structure of the bimetallic Pd–Pt composition. Notably, adjusting the amounts of CTAC in the synthesis allowed precise manipulation of the size of the Pd–Pt NDs, resulting in various Pd–Pt NDs with different sizes. The Pd–Pt NDs with different sizes exhibited distinctive electrocatalytic performances against both MOR and HER. For MOR and HER, the Pd–Pt NDs with an average diameter size of  $29.2 \pm 4.9$  nm, prepared using 200 mM of CTAC, exhibit higher catalytic activity compared to their Pd–Pt NDs counterparts with different sizes, commercial Pd/C, and Pt/C catalysts, due to their highly porous morphology, favorable exposed facet, and Pd–Pt bimetallic properties.

### **3.2. Experimental section**

#### **3.2.1. Chemical and materials**

CTAC (Aldrich, 25 wt%),  $K_2PtCl_4$  (Aldrich, 98%),  $Na_2PdCl_4$  (Aldrich, 98%), AA (Dae Jung Chemicals & Metals Co., 99.5%), Pd/C (Alfa Aesar, 20wt%), Pt/C (Alfa Aesar, 20wt%), potassium hydroxide (DaeJung Chemicals & Metals Co., 93%), and methanol (Junsei, 99.8%) were used as received. Deionized (DI) water was used in the preparation of chemical solutions.

#### **3.2.2. Synthesis of Pd–Pt NDs**

For synthesis of Pd–Pt–200<sub>CTAC</sub>, Pd–Pt–100<sub>CTAC</sub>, Pd–Pt–50<sub>CTAC</sub>, and Pd–Pt–10<sub>CTAC</sub> NDs, an aqueous solutions of CTAC (1 mL, X mM; X= 10, 50, 100, and 200 mM) were added into reaction mixtures containing of  $Na_2PdCl_4$  (0.5 mL, 5 mM),  $K_2PtCl_4$  (0.5 mL, 5 mM), AA (0.5 mL, 100 mM), and DI water (46 mL) with a vigorous stirring for 5 min, respectively. Subsequently, the reaction mixture was heated at 90 °C for 10 min. The result-ant reaction mixture was subjected to centrifugation and washed with ethanol/DI water (8000 rpm for 5 min, 3 times) to remove excess chemicals.

#### **3.2.3. Characterization**

Transmission electron microscopy (TEM) and scanning electron microscopy (SEM) images of the prepared Pd–Pt NDs were obtained on Jeol JEM-2100F and Jeol JEM-7210F, respectively. Inductively coupled plasma-optical emission spectrometry (ICP-OES) measurement was carried out using a Spectroblue-ICP-OES (Ametek). X-ray diffraction (XRD) measurements were conducted on a Rigaku D/MAX2500V/PC scanning for  $2\theta$  at 20 to 90 degrees. For preparation of TEM sample, first, residual chemicals in the Pd–Pt ND solution were removed by centrifugation. The precipitated Pd–Pt NDs were

re-dispersed into purified water and then an aqueous solution including nanoparticles was dropped on TEM grid (Formvar/Carbon 300 Mesh, Copper). Subsequently, the TEM grid was dried at room temperature. Before taking TEM image, the TEM grid was cleaned with ethanol.

#### **3.2.4. Electrochemical performance**

Electrochemical experiments were conducted in a three-electrode cell using EC-Lab Biologic Model SP-300 potentiostat. Pt wire was used as counter electrode. Ag/AgCl (3.0 M KCl) electrode for HER and Hg/HgO (in 3.0 M NaOH) electrode for MOR were used as reference electrodes, respectively. For the MOR electrocatalytic measurement, Ar-purged electrolyte (1.0 M KOH) were used for MOR. Before electrochemical experiments, catalyst ink (5  $\mu\text{L}$ ) was loaded on the GCE (0.196  $\text{cm}^2$ ).

HER electrocatalytic measurements were performed at room temperature. The N<sub>2</sub>-purged electrolyte (0.5 M H<sub>2</sub>SO<sub>4</sub>) was used for HER. Before electrochemical experiments, catalyst ink (5  $\mu\text{L}$ ) was loaded on the L-type GCE (0.196  $\text{cm}^2$ ). The potential applied for linear sweep voltammogram (LSV) between 0.05 V to -0.25 V vs. RHE with sweep rate of 10  $\text{mV s}^{-1}$ .

### 3.3. Result and Discussion

**Figure 3.1.a** and **b** shows the representative TEM images of the product prepared by co-reduction of  $\text{Na}_2\text{PdCl}_4$  and  $\text{K}_2\text{PtCl}_4$  by AA in presence of CTAC (200 mM), demonstrating that the majority of the nanostructures consisted of NDs with highly porous branches. The NDs possess an average diameter size of  $29.2 \pm 4.9$  nm and branch thickness size of  $8.7 \pm 0.9$  nm, respectively. The high-resolution TEM (HR-TEM) image of a ND displays the d-spacing of 2.24 Å between adjacent lattice distance. This highly corresponds to that of the (111) planes of face-centered cubic (fcc) bimetallic Pd-Pt (inset in **Figure 3.1.b**).<sup>25</sup> Fast Fourier transform (FFT) pattern obtained from a ND reveals the highly crystalline feature of the prepared NCs (inset of **Figure 3.1.b**). Notably, as shown at inset in **Figure 3.1.b**, many un-saturated surface atoms at the tips of the ND were explicitly observed in the HR-TEM image. To investigate further structural characteristics of the NDs, the high-angle annular dark-field scanning TEM (HAADF-STEM) images of NDs were obtained (**Figure 3.1.c**).

The high porosity of the NDs was observed by strong contrast in the NDs. The formation of bimetallic Pd@Pt core-shell structure was corroborated by elemental mapping and overlap profile analysis with HAADF-STEM-energy-dispersive X-ray spectroscopy (HAADF-STEM-EDS) (**Figure 3.1.c** and **d**). The Pd/Pt atomic ratio of the NDs measured by EDS analysis and ICP-OES were 51:49 and 53:47, respectively. In addition, diffraction peaks in the XRD pattern of the NDs further show their Pd-Pt bimetallic feature (**Figure 3.1.e**).<sup>21,26,27</sup>

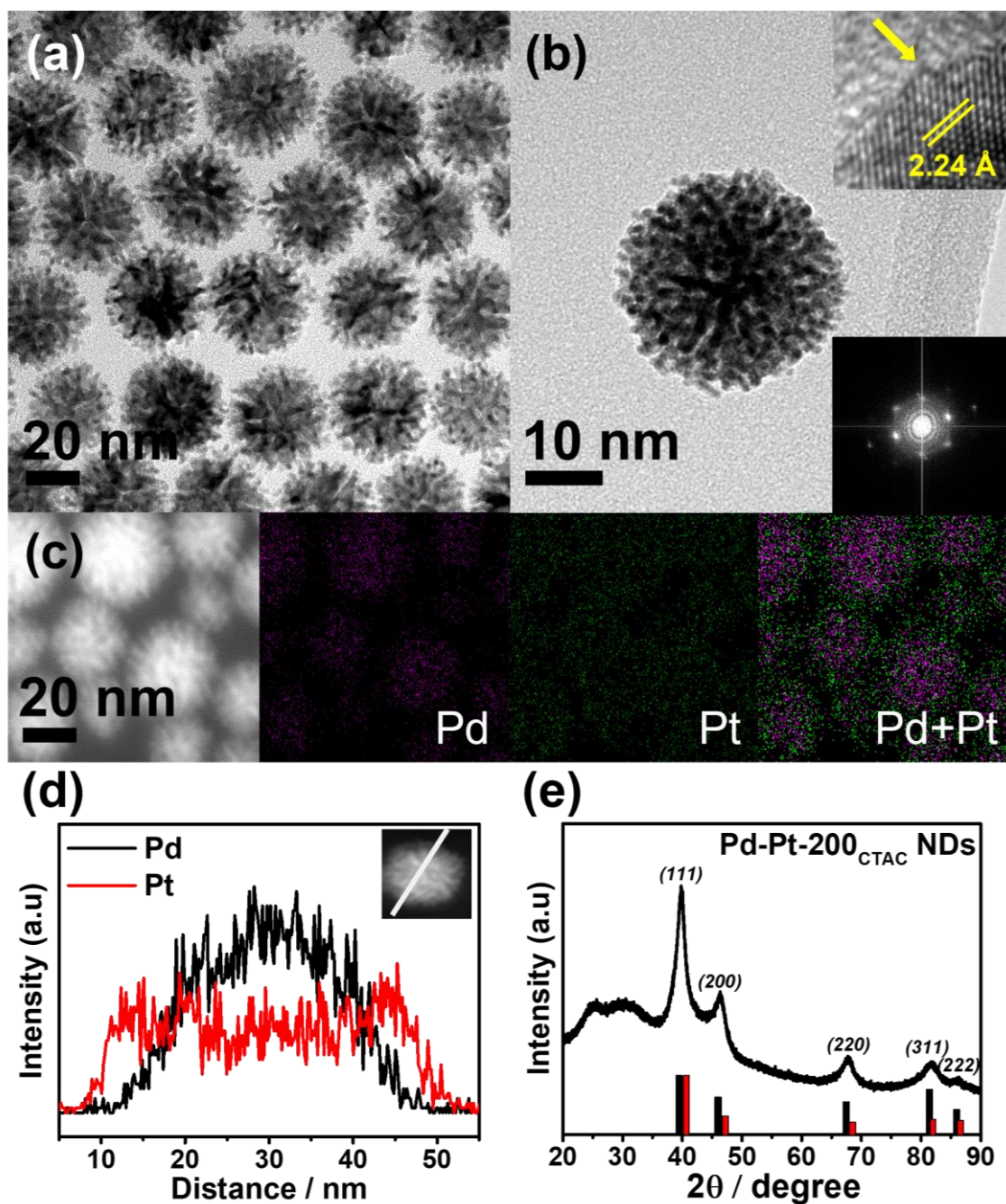


**Figure 3.1.** (a) and (b) HR-TEM image including the correspond FFT images. HAADF-STEM image with (c) corresponding EDS elemental mapping images, and (d) line-scan profiles analysis of Pd (black) and Pt (red) for the Pd-Pt NDs. (e) XRD pattern confirm of corroborating the Pd-Pt bimetallic feature.

The NDs with different diameter sizes and porosity were realized by changing the amount of CTAC added into the reaction mixture. The representative SEM and TEM images of the products show that the average diameter sizes of NDs were increased as the amount of CTAC increased (**Figure 3.2**). The

CTAC solution (200mM) resulted in the formation of Pd–Pt–200<sub>CTAC</sub> NDs with an average diameter size of  $29.2 \pm 4.9$  nm (standard synthesis). Pd–Pt NDs with an average size of  $46.3 \pm 7.7$ ,  $38.6 \pm 8.9$ , and  $36.5 \pm 5.6$  nm (Pd–Pt–10<sub>CTAC</sub>, Pd–Pt–50<sub>CTAC</sub>, and Pd–Pt–100<sub>CTAC</sub> NDs) were formed when the different concentrations of CTAC solutions (10, 50, and 100 mM) were added for synthesis of Pd–Pt nanostructures, respectively (**Figure 3.2.a-c**). Along with size change, NDs obtained by a higher concentration of CTAC show a high degree of porosity due to their more developed branches, indicating the highest porosity of Pd–Pt–200<sub>CTAC</sub> NDs than the other NDs (inset of **Figure 3.2.e-h**).

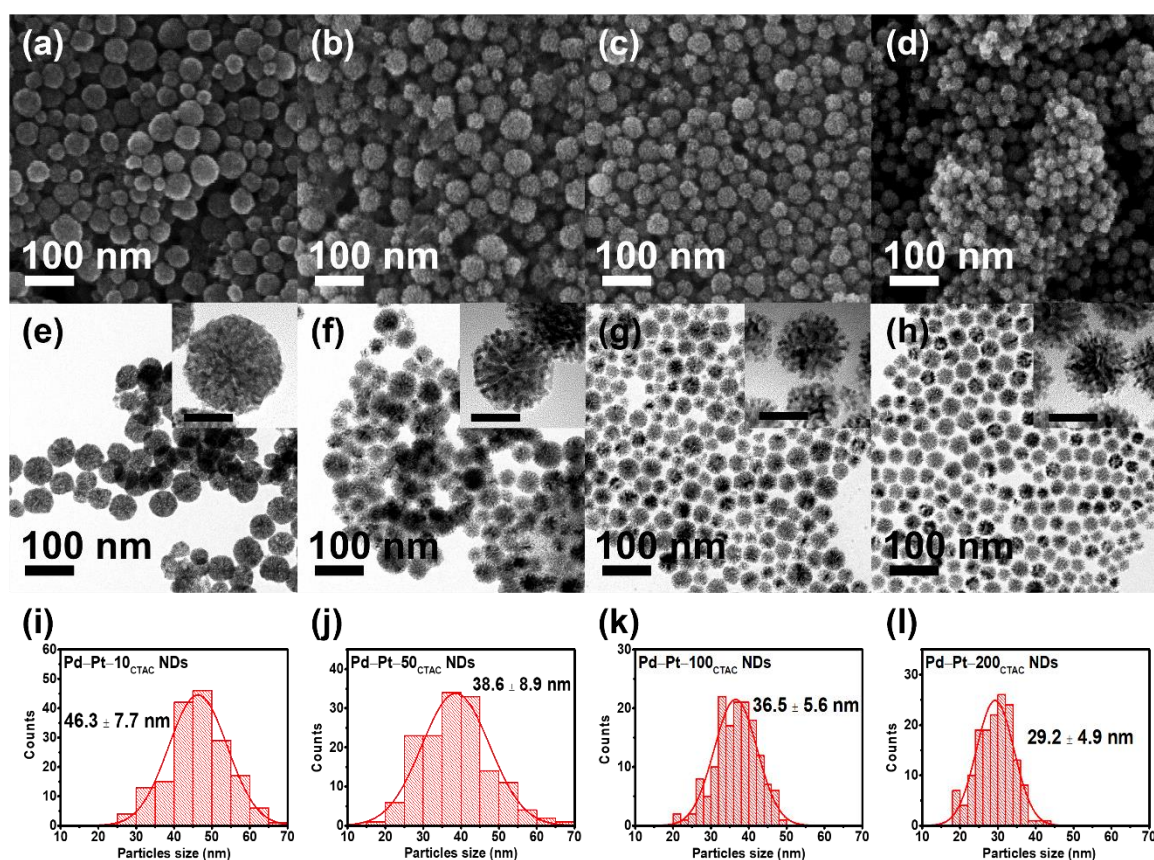


**Figure 3.2.** SEM and TEM images of Pd–Pt NDs with controlled CTAC concentration representative to (a); (e); (i) Pd–Pt–10<sub>CTAC</sub> NDs, (b); (f); (j) Pd–Pt–50<sub>CTAC</sub> NDs, (c); (g); (k) Pd–Pt–100<sub>CTAC</sub> NDs, and (d); (h); (l) Pd–Pt–200<sub>CTAC</sub> NDs. Scale bar in the inset figures of parts (e)-(h) is 30 nm.

The XRD patterns of the samples also show bimetallic Pd–Pt nature, which is analogous with that of Pd–Pt–200<sub>CTAC</sub> NDs (**Figure 3.3**). In addition, similar peak positions in XRD patterns for various Pd–Pt NDs were observed, which reveals the analogous composition structures.

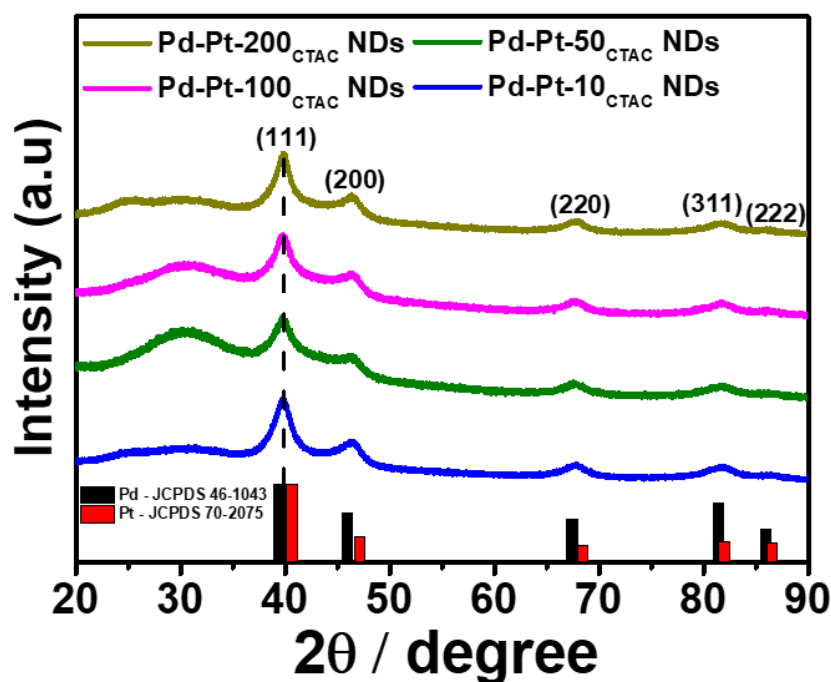


**Figure 3.3.** XRD Pattern of Pd–Pt NDs with controlled CTAC concentrations. The line pattern shows reference cards 46-1043 and 70-2075 for Pd and Pt according to JCPDS.

The different size of the NDs prepared by different amounts of CTAC indicates that CTAC and metal precursors closely interplay, resulting in different size and porosity. To further investigate the influence of CTAC concentration for the formation NDs, nanostructures were produced in reaction mixtures with various concentrations of CTAC, while other synthesis conditions were unchanged. In higher concentration of CTAC (500 mM), products having similar shape with the Pd–Pt–200<sub>CTAC</sub> NDs were synthesized (**Figure 3.4.a**), although their size is somewhat larger ( $48.3 \pm 3.4$  nm). In contrast, lower concentration of CTAC than 10 mM such as 2.5, 5.0, and 7.5 mM yielded some irregular shaped nanostructures (**Figure 3.4.b-d**). In low concentration of CTAC, although large amounts of seed NCs can be initially produced, insufficient surfactants adsorbed on the surface of seed NCs can lead to fast aggregation of pre-formed seed NCs, resulting in the formation of NDs with uncontrolled shapes and



large diameter sizes, which further demonstrate the importance of optimal CTAC concentration for the formation of dendritic shapes.<sup>10,23,28</sup> Given that NDs with well-developed branches and smaller size possess larger volume to surface area than NDs with unmaturing branches and larger size, we expected the Pd–Pt–200<sub>CTAC</sub> NDs can exhibit improved electrocatalytic performances.

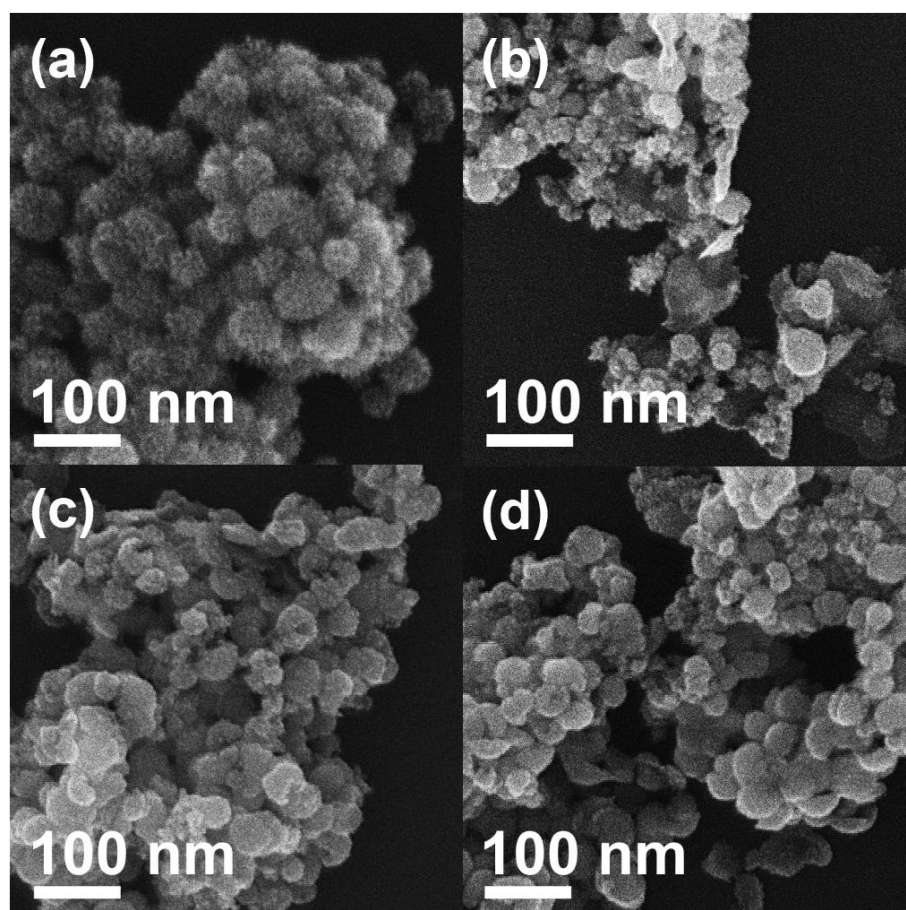


**Figure 3.4.** SEM images of Pd–Pt NDs prepared with controlled concentrations of CTAC with higher concentration of (a) 500 mM. Pd–Pt NDs prepared with lower concentration of CTAC than 10 mM with (b) 2.5 mM, (c) 5.0 mM, and (d) 7.5 mM.

To investigate the effect of dendritic structure and size on the bimetallic Pd–Pt NDs, the electrocatalytic activities of the various Pd–Pt NDs (Pd–Pt–200<sub>CTAC</sub>, Pd–Pt–100<sub>CTAC</sub>, Pd–Pt–50<sub>CTAC</sub>, and Pd–Pt–10<sub>CTAC</sub> NDs) were estimated for HER and their electrocatalytic activities were compared to those of both commercial Pd/C and Pt/C catalysts (**Figure 3.5**). CVs of various catalysts were measured in the N<sub>2</sub>-saturated 0.5 M H<sub>2</sub>SO<sub>4</sub> at sweeping rate of 50 mV s<sup>-1</sup> (**Figure 3.5.a**) to remove residual surfactants and organic molecules adsorbed on surface of the catalysts.<sup>29</sup> The HER performances were examined by

LSV polarization curves at sweeping rate  $10 \text{ mV s}^{-1}$  within the applied potential window of 0.05 to  $-0.25 \text{ V vs. RHE}$  at room temperature (**Figure 3.5.b** and **c**). According to the LSV curves, the overpotentials of the Pd–Pt–200<sub>CTAC</sub> NDs, Pd–Pt–100<sub>CTAC</sub> NDs, Pd–Pt–50<sub>CTAC</sub> NDs, Pd–Pt–10<sub>CTAC</sub> NDs, Pd/C, and Pt/C catalysts at current density ( $10 \text{ mA cm}^{-2}$ ) reaches 32.3, 32.4, 33.1, 34.7, 122.3, and 35.4 mV, respectively. To further evaluate the catalytic activities of the catalysts, the linear sections of the Tafel plots shown in **Figure 3.5.b** and **c** were fitted to the Tafel equation, and the slope values were obtained (**Figure 3.5.d**).<sup>30</sup> The Tafel slope values of the Pd–Pt–200<sub>CTAC</sub>, Pd–Pt–100<sub>CTAC</sub>, Pd–Pt–50<sub>CTAC</sub>, and Pd–Pt–10<sub>CTAC</sub> NDs were 23.8, 24.4, 24.7, and 25.1  $\text{mV dec}^{-1}$ , respectively, which are lower than those of both commercial Pd/C ( $76.5 \text{ mV dec}^{-1}$ ) and Pt/C ( $30.5 \text{ mV dec}^{-1}$ ) catalyst (**Table 3.1**). The findings signify that superior HER activities of all bimetallic Pd–Pt NDs than commercial Pd/C and Pt/C catalysts. Noticeably, the Pd–Pt–200<sub>CTAC</sub> NDs exhibited the highest electrochemical HER activity than different Pd–Pt NDs, which implies the importance of dendritic shapes with well-developed branches.

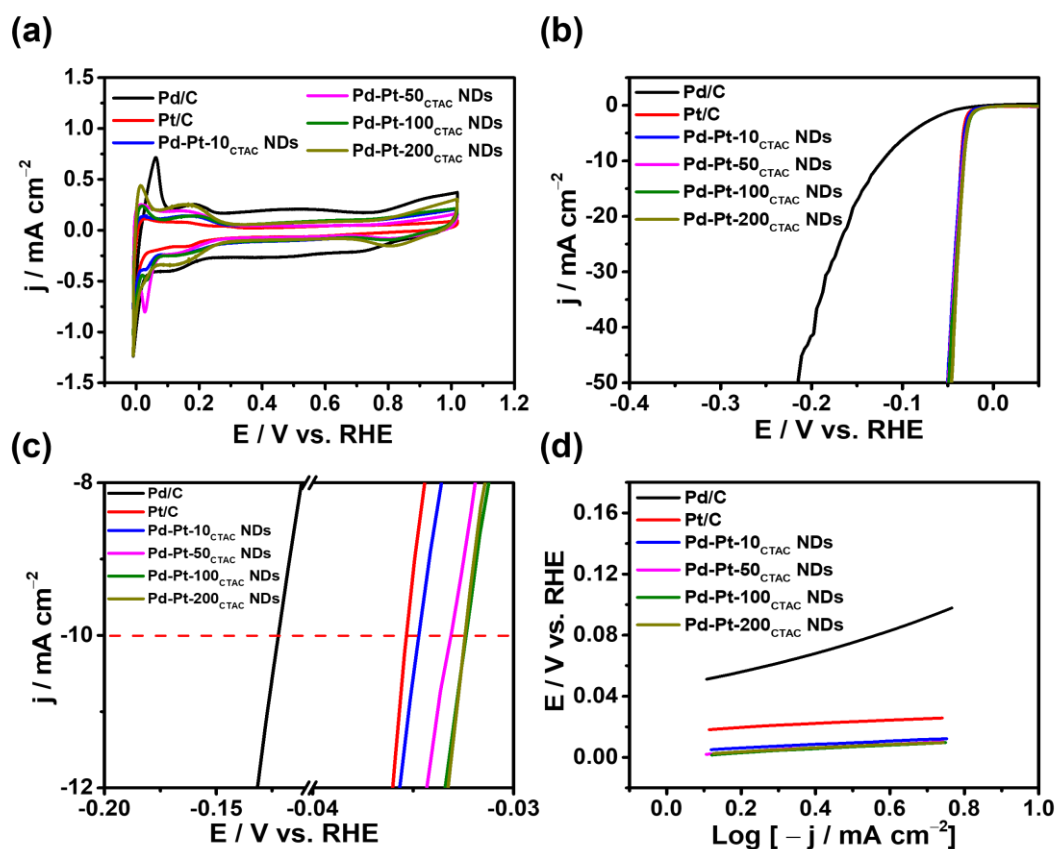


**Figure 3.5.** Electrocatalytic HER performance of different Pd–Pt NDs, and commercial Pd/C and Pt/C



electrocatalysts measured in 0.5 M H<sub>2</sub>SO<sub>4</sub> saturated with N<sub>2</sub>; sweep rate at 50 mV s<sup>-1</sup> (CVs) and 10 mV s<sup>-1</sup> (LSV). (a) CVs of all PdPt electrocatalysts. (b) LSV polarization curves and (c) derived from (b) to see details of H<sub>2</sub> evolution in overpotential at 10 mA cm<sup>-2</sup> of all electrocatalysts including commercials. (d) corresponded Tafel plots recorded on the electrode by polarization curves at potential 10 mV s<sup>-1</sup>.

**Table 3.1.** Activities values for all electrocatalysts including commercial Pd/C and Pt/C in HER activity. The values including overpotential at 10 mA cm<sup>-2</sup> and Tafel plots as compares in 0.5 M H<sub>2</sub>SO<sub>4</sub>.

| <b>Catalyst</b>                     | <b>Overpotential / <math>\eta</math> (mV)<br/>~10 mA cm<sup>-2</sup></b> | <b>Tafel Plots / (mV dec<sup>-1</sup>)</b> |
|-------------------------------------|--|--|
| <b>Pd/C</b>                         | <b>122.3 mV</b>  | <b>76.8 mV dec<sup>-1</sup></b>            |
| <b>Pt/C</b>                         | <b>35.3 mV</b>   | <b>30.5 mV dec<sup>-1</sup></b>            |
| <b>Pd-Pt-10<sub>CTAC</sub> NDs</b>  | <b>34.7 mV</b>   | <b>25.1 mV dec<sup>-1</sup></b>            |
| <b>Pd-Pt-50<sub>CTAC</sub> NDs</b>  | <b>33.1 mV</b>   | <b>24.7 mV dec<sup>-1</sup></b>            |
| <b>Pd-Pt-100<sub>CTAC</sub> NDs</b> | <b>32.4 mV</b>   | <b>24.4 mV dec<sup>-1</sup></b>            |
| <b>Pd-Pt-200<sub>CTAC</sub> NDs</b> | <b>32.3 mV</b>   | <b>23.8 mV dec<sup>-1</sup></b>            |

To further investigate the electrocatalytic properties of bimetallic Pd–Pt–200CTAC NDs, an electrochemical MOR was performed with various of the catalysts including different NDs, commercial Pd/C, and Pt/C. CVs of various catalysts were obtained in the N<sub>2</sub>-saturated 1.0 M KOH (**Figure 3.6.a**). Electrochemically active surface areas (ECSAs) of the catalysts were measured using the reduction charge of oxygen species in the CVs of the catalysts. The ECSAs for the Pd–Pt–200<sub>CTAC</sub> NDs, Pd–Pt-100<sub>CTAC</sub> NDs, Pd–Pt–50<sub>CTAC</sub> NDs, Pd–Pt–10<sub>CTAC</sub> NDs, Pd/C, and Pt/C were 55.4, 46.4, 43.9, 29.8, 63.1, and 69.2 m<sup>2</sup> g<sup>-1</sup>, respectively (**Figure 3.6.b**), which shows that the higher ECSA value of Pd–Pt–200<sub>CTAC</sub> NDs than the other Pd–Pt NDs can be attributed to their smaller size and well-developed branches leading high porosity. To check the morphological benefits of the Pd–Pt–200<sub>CTAC</sub> NDs for electrocatalytic reactions, the CVs of the catalysts in 1.0 M KOH containing 1.0 M methanol were

measured and their mass activities were obtained by normalizing the current densities by the total mass (Pd+Pt) of the catalysts loaded on the glassy carbon electrode (GCE) used as a working electrode (**Figure 3.6.c**). The mass activities of the Pd–Pt–200<sub>CTAC</sub>, Pd–Pt–100<sub>CTAC</sub>, Pd–Pt–50<sub>CTAC</sub>, and Pd–Pt–10<sub>CTAC</sub> NDs for MOR were 6.40, 5.87, 5.37, and 4.67 A mg<sub>Pt</sub><sup>-1</sup>, respectively. Notably, all bimetallic Pd–Pt NDs showed better MOR activities than both commercial Pd/C (0.90 A mg<sub>Pd</sub><sup>-1</sup>) and Pt/C (2.06 A mg<sub>Pt</sub><sup>-1</sup>) catalysts (**Figure 3.6.c and e**), which can be attributed to undercoordinated surface atoms formed by their unique dendritic shapes and bimetallic Pd–Pt surface. In previous reports, undercoordinated surface atoms can promote the conversion of reagents to products by optimizing binding strength between surface of nanostructures and intermediates, which could endow them with greatly enhanced electrocatalytic activity.<sup>8</sup> In addition, compared with pure Pd and Pt catalysts, Pd–Pt bimetallic catalysts could reduce the adsorption of surface poisoning intermediates, boosting the electrochemical reactions. On the other hand, among the different bimetallic Pd–Pt NDs, the Pd–Pt–200<sub>CTAC</sub> NDs exhibited the largest mass activity among the different NDs for MOR: the Pd–Pt–200<sub>CTAC</sub> NDs showed 1.09-, 1.19-, and 1.37-times higher mass activity than Pd–Pt–100<sub>CTAC</sub>, Pd–Pt–50<sub>CTAC</sub>, and Pd–Pt–10<sub>CTAC</sub> NDs, respectively.

Furthermore, the corresponding current density of the Pd–Pt–200<sub>CTAC</sub> NDs, which is calculated by normalizing the current density with ECSAs of the catalysts is 25.12 mA cm<sup>-2</sup>, which is 1.06, 1.11, 1.20, 17.56, and 8.43 folds larger than those of the Pd–Pt–100<sub>CTAC</sub> NDs (23.49 mA cm<sup>-2</sup>), Pd–Pt–50<sub>CTAC</sub> NDs (22.64 mA cm<sup>-2</sup>), Pd–Pt–10<sub>CTAC</sub> NDs (20.89 mA cm<sup>-2</sup>), Pd/C (1.43 mA cm<sup>-2</sup>), and Pt/C (2.98 mA cm<sup>-2</sup>) catalysts, respectively (**Figure 3.6.d and e**). Mass and specific activities for MOR of various bimetallic Pd–Pt NDs show similar trend across the different size of Pd–Pt NDs against the counterparts of commercial Pd/C and Pt/C. Taken together, these electrochemical experiments demonstrate the synergistic influence of dendritic shape and Pd–Pt bimetallic feature to increase electrocatalytic performances.<sup>31-33</sup> The MOR activity of the Pd–Pt–200<sub>CTAC</sub> NDs was compared with those of previously reported Pd–Pt-based catalysts (**Table 3.2**). The Pd–Pt–200<sub>CTAC</sub> NDs showed superior activities than the previously reported catalysts, which can be due to dendritic shape and bimetallic Pd–Pt composition structure.<sup>27,34-42</sup> To investigate the stability of prepared catalysts, chronoamperometric (CA) curves of

the various Pd–Pt NDs, Pd/C, and Pt/C catalysts were obtained at  $-0.15$  V vs. Hg/HgO in a solution containing 1.0 M KOH + 1.0 M methanol for 30 minutes (**Figure 3.6.f**). During the stability test, both commercial Pd/C and Pt/C catalysts revealed fast decay in current density. In contrast, the current density of Pd–Pt NDs in MOR was well maintained compared to those of commercial Pd/C and Pt/C catalysts after 30 min.

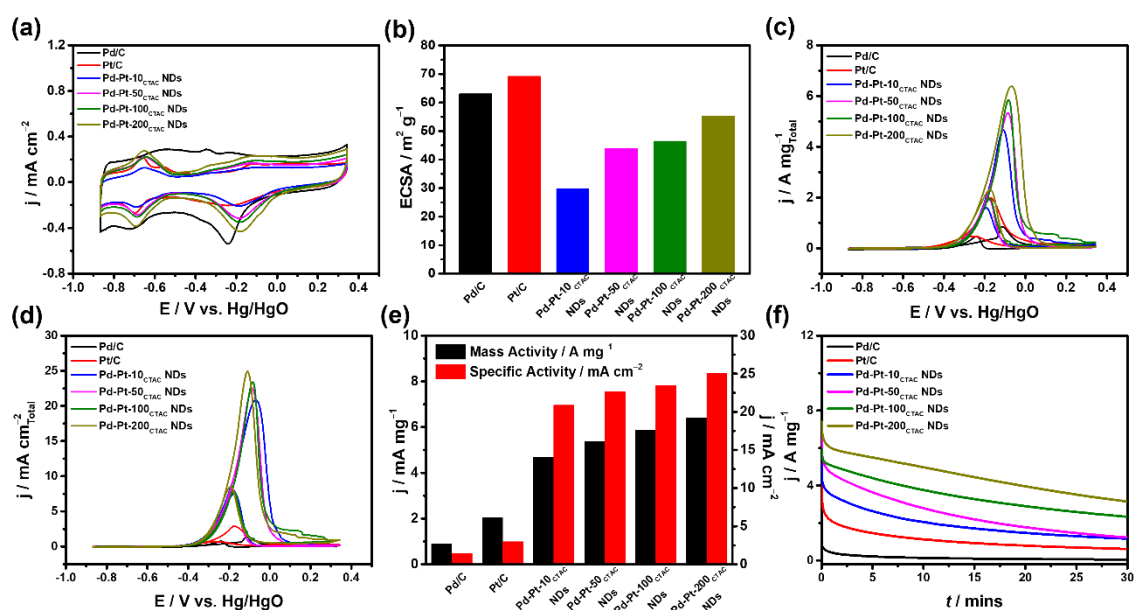


**Figure 3.6.** MOR performance of different Pd-Ptx NDs and commercial Pd/C and Pt/C electrocatalysts measured in 1.0 M KOH containing 1.0 M methanol saturated with  $\text{N}_2$ ; sweep rate at  $50 \text{ mV s}^{-1}$ . (a) CVs of all catalysts and (b) ECSA of all values of different electrocatalysts include commercials. MOR of all metals (Pd + Pt) (c) mass-normalized CV curves, (d) specific activity-normalized CV curves, and (e) Mass and specific activity data based on all different electrocatalysts. (f) Durability evaluation by chronoamperometry tests at  $-0.15$  V vs. Hg/HgO for 30 minutes off all electrocatalysts.

**Table 3.2.** Comparative results for electrochemical MOR activity based on previous re-ports using Pd-Pt based catalysts in the literature.

| Catalyst                                      | Electrochemical Condition     | Mass Activity ( $A\text{ mg}^{-1}_{\text{total}}$ ) | Ref.                |
|---|-------------------------------|---|---------------------|
| <b>Pd-Pt-200<sub>CTAC</sub> Nanodendrites</b> | <b>1 M KOH +<br/>1 M MeOH</b> | <b>6.40</b>   | <b>In this work</b> |
| Pd <sub>45</sub> Pt <sub>55</sub> Nanowires   | 1 M KOH +<br>1 M MeOH         | ~1.90   | [34]                |
| h-BN/PdPt Nanocorals                          | 1 M KOH +<br>0.5 M MeOH       | 0.96  | [35]                |
| PtPd/RGO nanogarlands                         | 1 M KOH +<br>1 M MeOH         | 0.33  | [36]                |
| Pt <sub>50</sub> Pd <sub>50</sub> Nanocubes   | 1 M KOH +<br>1 M MeOH         | 0.34  | [37]                |
| PdPt/CNTs                                     | 0.5 M KOH +<br>0.5 M MeOH     | 1.07  | [38]                |
| Pt <sub>30</sub> Pd <sub>70</sub> /C          | 1 M KOH +<br>1 M MeOH         | 0.72  | [39]                |
| o-PdH <sub>0.43</sub> @Pt Nanooctahedra       | 1 M KOH +<br>1 M MeOH         | 3.68  | [27]                |
| c-PdH <sub>0.43</sub> @Pt Nanocubes           | 1 M KOH +<br>1 M MeOH         | 2.14  | [27]                |
| PtPd Nanowires                                | 1 M KOH +<br>1 M MeOH         | 4.29  | [40]                |
| PdPt Bimetallic Nanosponges                   | 1 M KOH +<br>1 M MeOH         | ~2.20   | [41]                |
| Pt@Pd/RGO                                     | 1 M KOH +<br>1 M MeOH         | ~0.65   | [42]                |

In particular, the Pd–Pt–200<sub>CTAC</sub> NDs showed the best stability among the various Pd–Pt NDs. Furthermore, the CVs of the Pd–Pt–200<sub>CTAC</sub> NDs, Pd/C, and Pt/C catalysts were obtained after CA measurement (30 min) to check the superior stability of the Pd–Pt–200<sub>CTAC</sub> NDs (**Figure 3.7.**). After the CA for 30 min, mass activity of the Pd–Pt–200<sub>CTAC</sub> NDs was determined as 6.1 A mg<sub>Pd+Pt</sub><sup>-1</sup>, which is 4.7 % decrease compared with initial mass activity of the Pd–Pt–200<sub>CTAC</sub> NDs, whereas Pd/C (0.7 A mg<sub>Pd</sub><sup>-1</sup>), and Pt/C (1.7 A mg<sub>Pt</sub><sup>-1</sup>) catalysts exhibited 22.2 and 14.3 % decreases compared to those obtained before operation of CA for 30 min, respectively.

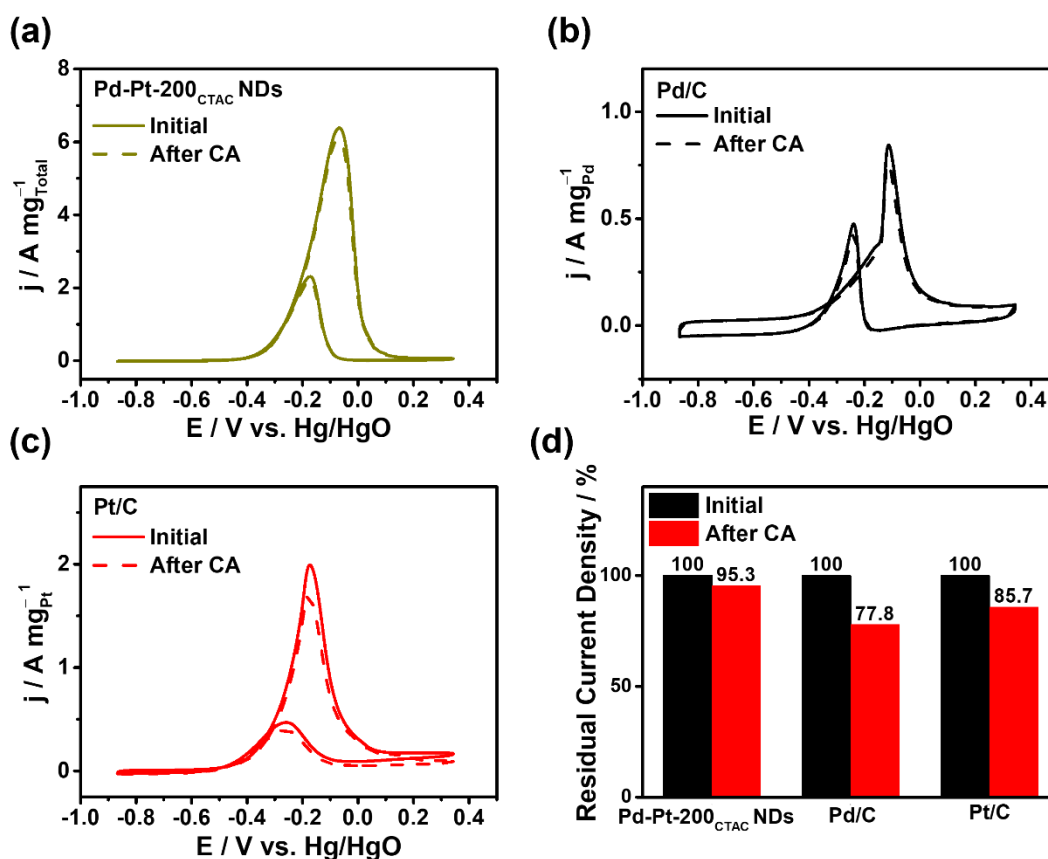


**Figure 3.7.** MOR residual current density activities of Pd–Pt–200<sub>CTAC</sub> NDs, Pd/C and Pt/C after chronoamperometry experiment for 30 minutes.

### **3.4. Conclusion**

We developed a facile synthesis for the preparation of bimetallic Pd–Pt NDs with well–developed branches. The morphology and size of the Pd–Pt NDs were highly sensitive to concentration of CTAC used as surfactant. The Pd–Pt NDs exhibited excellent electrocatalytic performances for both HER and MOR compared with both commercial Pd/C and Pt/C catalysts. The investigations through the electrochemical reactions have established that the Pd–Pt NDs have superb activity and stability for both HER and MOR compared with both commercial Pd/C and Pt/C catalysts. This demonstrates that the co–influence of dendritic shape and bimetallic Pd–Pt nature is the pivotal factor for their enhancement in electrocatalytic performance. In particular, the Pd–Pt–200<sub>CTAC</sub> NDs showed superior electrocatalytic performances than their Pd–Pt ND counterparts, which can be due to numerous unsaturated surface atoms in unique well–developed branches.

### 3.5. References

1. Hong, J. W.; Kang, S. W.; Choi, B. S.; Kim, D.; Lee, S. B.; Han, S. W. *ACS Nano*, **2012**, 6, 2410 - 2419.
2. Wu, J.; Qi, L.; You, H.; Gross, A.; Li, J.; Yang, H. *J. Am. Chem. Soc.*, **2012**, 134, (29), 11880-3.
3. Lv, H.; Chen, X.; Xu, D.; Hu, Y.; Zheng, H.; Suib, S. L.; Liu, B. *Appl. Catal. B-Environ.*, **2018**, 238, 525-532.
4. Wang, S.; Yang, G.; Yang, S., *J. Phys. Chem. C* **2015**, 119, (50), 27938-27945.
5. Wu, Y.; Wang, D.; Niu, Z.; Chen, P.; Zhou, G.; Li, Y., *Angew. Chem. Int. Ed. Engl.*, **2012**, 51, (50), 12524-12528.
6. Guo, T.; Xiang, H.; Li, W.; Li, H.; Chen, H.; Liu, S.; Yu, G., *ACS Sustain. Chem. Eng*, **2020**, 8, (7), 2901-2909.
7. Yamauchi, Y.; Wang, L., *J. Am. Chem. Soc.*, **2010**, 132, 13636 - 13638.
8. Lee, Y. W.; Im, M.; Hong, J. W.; Han, S. W., *ACS Appl. Mater. Interfaces*, **2017**, 9, (50), 44018-44026.
9. Shi, Q.; Zhu, C.; Li, Y.; Xia, H.; Engelhard, M. H.; Fu, S.; Du, D.; Lin, Y., *Chem. Mat.*, **2016**, 28, (21), 7928-7934.
10. Ye, Y.; Joo, J.; Lee, S.; Lee, J. *J. Mater. Chem. A*, **2014**, 2, (45), 19239-19246.
11. Lim, B.; Jiang, M.; Pedro, H. C.; Cho, C.; Xia, Y., *Science*, **2009**, 324, 1302 - 1305.
12. Li, X.; Li, X.; Liu, C.; Huang, H.; Gao, P.; Ahmad, F.; Luo, L.; Ye, Y.; Geng, Z.; Wang, G.; Si, R.; Ma, C.; Yang, J.; Zeng, J., *Nano Lett.*, **2020**, 20, (2), 1403-1409.
13. Wang, W.; He, T.; Yang, X.; Liu, Y.; Wang, C.; Li, J.; Xiao, A.; Zhang, K.; Shi, X.; Jin, M., *Nano Lett.*, **2021**, 21, (8), 3458-3464.
14. Wu, Q.; Luo, M.; Han, J.; Peng, W.; Zhao, Y.; Chen, D.; Peng, M.; Liu, J.; de Groot, F. M. F.; Tan, Y., *ACS Energy Lett.*, **2019**, 5, (1), 192-199.
15. Xia, B. Y.; Wu, H. B.; Wang, X.; Lou, X. W., *J. Am. Chem. Soc.*, **2012**, 134, (34), 13934-13937.
16. Zhang, N.; Guo, S.; Zhu, X.; Guo, J.; Huang, X., *Chem. Mat.*, **2016**, 28, (12), 4447-4452.
17. Chen, L.; Lu, L.; Zhu, H.; Chen, Y.; Huang, Y.; Li, Y.; Wang, L., *Nat. Commun.*, **2017**, 8, 14136.
18. Fan, J.; Qi, K.; Zhang, L.; Zhang, H.; Yu, S.; Cui, X., *ACS Appl. Mater. Interfaces*, **2017**, 9, (21), 18008-18014.
19. Wu, J.; Cui, X.; Fan, J.; Zhao, J.; Zhang, Q.; Jia, G.; Wu, Q.; Zhang, D.; Hou, C.; Xu, S.; Jiao, D.; Gu, L.; Singh, D. J.; Zheng, W., *ACS Energy Lett.*, **2021**, 6, (5), 1912-1919.
20. Li, S. S.; Lv, J. J.; Teng, L. N.; Wang, A. J.; Chen, J. R.; Feng, J. J., *ACS Appl. Mater. Interfaces*, **2014**, 6,

- (13), 10549-10555.
21. Liu, Y.; Liu, S.; Che, Z.; Zhao, S.; Sheng, X.; Han, M.; Bao, J., *J. Mater. Chem. A*, **2016**, 4, (42), 16690-16697.
  22. Wu, L.; Liu, Z.; Xu, M.; Zhang, J.; Yang, X.; Huang, Y.; Lin, J.; Sun, D.; Xu, L.; Tang, Y., *Int. J. Hydrog. Energy*, **2016**, 41, (16), 6805-6813.
  23. Zhang, J.; Wan, L.; Liu, L.; Deng, Y.; Zhong, C.; Hu, W., *Nanoscale*, **2016**, 8, (7), 3962-3972.
  24. Huang, X.; Li, Y.; Li, Y.; Zhou, H.; Duan, X.; Huang, Y., *Nano Lett.*, **2012**, 12, (8), 4265-70.
  25. Li, F.-M.; Gao, X.-Q.; Li, S.-N.; Chen, Y.; Lee, J.-M., *NPG Asia Mater.*, **2015**, 7, (10), e219-e219.
  26. Kang, S. W.; Lee, Y. W.; Park, Y.; Choi, B. S.; Hong, J. W.; Han, S. W., *ACS Nano*, **2013**, 7, 7945-7955.
  27. Liu, G.; Zhou, W.; Ji, Y.; Chen, B.; Fu, G.; Yun, Q.; Chen, S.; Lin, Y.; Yin, P. F.; Cui, X.; Liu, J.; Meng, F.; Zhang, Q.; Song, L.; Gu, L.; Zhang, H. *J. Am. Chem. Soc.*, **2021**, 143, (29), 11262-11270.
  28. Zhang, H.; Jin, M.; Xia, Y. *Chem. Soc. Rev.*, **2012**, 41, (24), 8035-8049.
  29. Yu, Y.; Jiang, K.; Luo, M.; Zhao, Y.; Lan, J.; Peng, M.; de Groot, F. M. F.; Tan, Y., *ACS Nano*, **2021**, 15, (3), 5333-5340.
  30. Yao, R.-Q.; Zhou, Y.-T.; Shi, H.; Zhang, Q.-H.; Gu, L.; Wen, Z.; Lang, X.-Y.; Jiang, Q. *ACS Energy Lett.*, **2019**, 4, (6), 1379-1386.
  31. Chang, F.; Bai, Z.; Li, M.; Ren, M.; Liu, T.; Yang, L.; Zhong, C. J.; Lu, J. *Nano Lett.*, **2020**, 20, (4), 2416-2422.
  32. Sarkar, S.; Peter, S. C. *Inorg. Chem. Front.*, **2018**, 5, (9), 2060-2080.
  33. Wu, J.; Shan, S.; Cronk, H.; Chang, F.; Kareem, H.; Zhao, Y.; Luo, J.; Petkov, V.; Zhong, C.-J. *J. Phys. Chem. C*, **2017**, 121, (26), 14128-14136.
  34. Zhu, C.; Guo, S.; Dong, S. *Adv. Mater.*, **2012**, 24, (17), 2326-2331.
  35. Zhang, H.; Xu, L.; Tian, Y.; Jiao, A.; Li, S.; Liu, X.; Chen, F., *ACS omega*, **2019**, 4, (6), 11163-11172.
  36. Li, S. S.; Zheng, J. N.; Ma, X.; Hu, Y. Y.; Wang, A. J.; Chen, J. R.; Feng, J. J., *Nanoscale*, **2014**, 6, (11), 5708-5713.
  37. Zhou, L. N.; Zhang, X. T.; Wang, Z. H.; Guo, S.; Li, Y. J., *Chem. Commun.*, **2016**, 52, (86), 12737-12740.
  38. Yang, G.; Zhou, Y.; Pan, H. B.; Zhu, C.; Fu, S.; Wai, C. M.; & Lin, Y., *Ultrason. Sonochem.*, **2016**, 28, 192-198.
  39. De la Cruz-Cruz, J. J.; Domínguez-Crespo, M. A.; Ramírez-Meneses, E.; Torres-Huerta, A. M.; Brachetti-Sibaja, S. B.; Cayetano-Castro, N.; Dorantes-Rosales, H. J. *Int. J. Hydrog. Energy*, **2020**, 45, (7), 4570-



4586.

40. Zhai, Y.; Zhu, Z.; Lu, X.; Zhou, Z.; Shao, J.; Zhou, H. S., *ACS Appl. Energ. Mater.*, **2017**, *1*, (1), 32-37.
41. Zhu, C.; Guo, S.; Dong, S. Rapid, *Chem. Eur. J.*, **2013**, *19*, (3), 1104-1111.
42. Feng, J. X.; Zhang, Q. L.; Wang, A. J.; Wei, J.; Chen, J. R.; Feng, J. J., *Electrochim. Acta*, **2014**, *142*, 343-350.

## **Chapter 4. Universal Synthesis Strategy of Edge-Rich Holey Pt Based Ultrathin Alloy Nanosheets for Efficient Electrochemical Oxygen Reduction Reaction**

### **4.1. Introduction**

Ultrathin two-dimensional (2D) metal nanosheets have been the subject of intensive research for various catalytic reactions due to their unique properties coming from anisotropic structures and atomic thickness compared with bulk.<sup>1-8</sup> Ultrathin metal nanosheets with high surface-to-volume ratio significantly enhanced the catalytic performances via their high utilization efficiency of the metal.<sup>9-14</sup> In addition, the development of bimetallic alloy nanosheets has provided a route to improve the desirable properties for various electrocatalytic reactions in comparison to monometallic nanosheets.<sup>15-</sup>

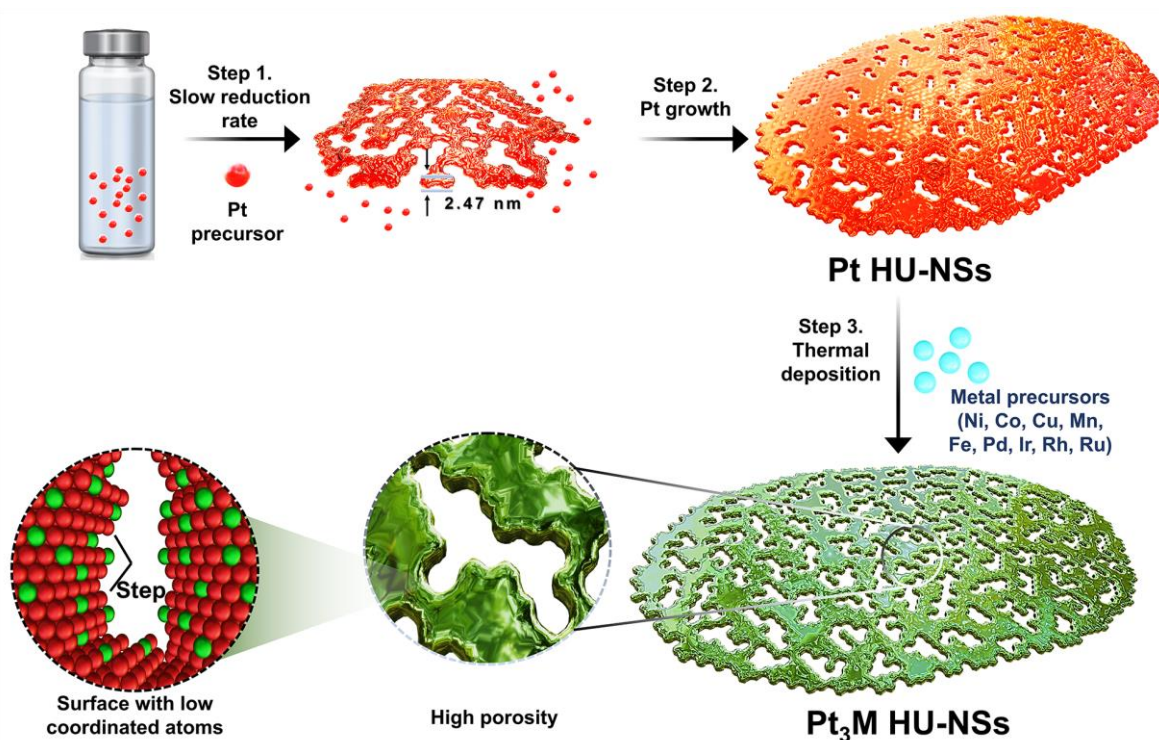
21

To propose an advanced electrocatalyst, we focus on the fact that the 2D nanostructures consist of basal plane and edge, in which the edge is composed of lower coordinated atoms in comparison to the basal plane. Since the establishment of the optimized coordination environment in the catalysts is a promising approach to increase the intrinsic reactivity of active sites,<sup>22-25</sup> the distinctive coordination environments between basal plane and edge site of 2D nanostructures may play a crucial role in determining its electrocatalytic performances.<sup>26-31</sup> For example, Calle-Vallejo et al. reported that concave Pt surfaces containing a considerable number of step or kink atoms can enhance the catalytic performance for the oxygen reduction reaction (ORR) compared to low-indexed Pt surfaces.<sup>26</sup> Sun et al. synthesized 2D Pt-Pd-based nanorings with a high density of edge sites, which showed improved ORR activity compared to the counterparts mostly composed of low-index facets.<sup>32</sup> These results indicate the importance of low-coordinated surface atoms in improving the performance of nano-sized catalyst. Taken all together, the synthesis of ultrathin Pt-based alloy (Pt-M) 2D nanosheets with a high density of edge atoms is expected to enable the development of advanced catalysts for a variety of electrochemical reactions.

Although metal-based 2D nanostructures with ultrathin thicknesses (~3 nm) have been designed, including Pd, Ir, Rh, and Au,<sup>33-37</sup> the development of ultrathin Pt-M nanosheets is severely limited due to the difficulty of stabilizing the high Pt surface energy compared to the above metal elements.<sup>30,38,39</sup> Moreover, increasing the durability of thermodynamically unstable edge atoms and deepening the

comprehensive understanding of the Pt-M growth mechanism remain challenging tasks to achieve the synthesis of edge-rich ultrathin Pt-M nanosheets

Herein, we report the universal synthesis process to achieve holey ultrathin Pt<sub>3</sub>M alloy nanosheets (Pt<sub>3</sub>M HU-NSs, M = Ni, Co, Cu, Ir, Pd, Ru, Rh, Fe, and Mn) and the improved electrocatalytic performances of Pt<sub>3</sub>Ni HU-NSs for electrochemical ORR. The edge-rich Pt<sub>3</sub>M HU-NSs with a thickness of about 3 nm were prepared via a two-step template-based synthesis approach. The preparation of pure Pt HU-NSs by controlling the reduction rate of Pt precursor and the further thermal treatment to form Pt<sub>3</sub>M alloys without shape deformation are key levers for the successful synthesis of Pt<sub>3</sub>M HU-NSs (**Scheme 4.1.**). The as-prepared Pt<sub>3</sub>Ni HU-NSs exhibited greatly enhanced ORR activity and stability compared to other Pt<sub>3</sub>M HU-NSs, pristine Pt HU-NSs, and the state-of-the-art Pt/C catalysts due to the unique morphological and compositional properties.



**Scheme 4.1.** Schematic illustration for the synthesis procedure of Pt<sub>3</sub>M HU-NSs.

## 4.2. Experimental section

### 4.2.1. Chemicals and materials

Potassium tetrachloroplatinate(II) (K<sub>2</sub>PtCl<sub>4</sub>, 99.0%), nickel(II) chloride hexahydrate (NiCl<sub>2</sub>·6H<sub>2</sub>O,

99.9%), cobalt(II) chloride hexahydrate ( $\text{CoCl}_2 \cdot 6\text{H}_2\text{O}$ , 99.9%), copper(II) chloride dihydrate ( $\text{CuCl}_2 \cdot 6\text{H}_2\text{O}$ , 99.9%), iron(II) chloride tetrahydrate ( $\text{FeCl}_2 \cdot 4\text{H}_2\text{O}$ , 98%), manganese(II) chloride tetrahydrate ( $\text{MnCl}_2 \cdot 4\text{H}_2\text{O}$ , 98%), sodium tetrachloropalladate(II) ( $\text{Na}_2\text{PdCl}_4$ , >99.99%), iridium(III) chloride hydrate ( $\text{IrCl}_3 \cdot x\text{H}_2\text{O}$ , 99.9%), rhodium(III) chloride hydrate ( $\text{RhCl}_3 \cdot x\text{H}_2\text{O}$ , >98%), ruthenium(III) chloride trihydrate ( $\text{RuCl}_3 \cdot x\text{H}_2\text{O}$ , >98%), cetyltrimethylammonium chloride solution (CTAC, solution in water, 25wt%), perchloric acid ( $\text{HClO}_4$ , 70%), isopropanol (IPA, >99.99%), polyvinylpyrrolidone (PVP,  $M_w \sim 55,000$ ), and Nafion resin solution (5 wt%) were purchased from Sigma-Aldrich. Pt/C (20 wt%, average Pt particle size = 3 nm) was purchased from Alfa Aesar. L-ascorbic acid (AA, 99.5%) was purchased from DAEJUNG. N,N-Dimethylformamide (DMF, 99.5%) was purchased from JUNSEI. Deionized water (18.2 M $\Omega$  cm) was employed to prepare the reaction solutions.

#### **4.2.2. Synthesis of holey ultrathin Pt nanosheets (Pt HU-NSs)**

In a typical synthesis of Pt-HU NSs, 0.5 mL of DMF, 20 mg of PVP, 0.05 mL of CTAC (100 mM), and 1.5 mL of  $\text{K}_2\text{PtCl}_4$  (5 mM) were added into 4 mL of deionized water with gentle shaking, and then 0.5 mL of AA (100 mM) was added into mixture and sonicated for 3 min. The reaction mixture was heated at 40 °C for 1 h in water bath. Subsequently, resultant products were collected by centrifugation and washed two times with ethanol.

#### **4.2.3. Synthesis of Pt<sub>3</sub>Ni HU-NSs**

In a typical synthesis of Pt<sub>3</sub>Ni HU-NSs, Pt HU-NSs obtained from 30 mL of Pt HU-NS solution, 20 mg of PVP, 1 mL of  $\text{NiCl}_2 \cdot 6\text{H}_2\text{O}$  (12.5 mM), and 0.5 mL of AA (100 mM) were dispersed in 5 mL of DMF. The reaction mixture was transferred to a 35 mL Teflon-lined stainless steel autoclave which was then sealed and heated at 180 °C for 6 h in a conventional oven. Resultant products were collected by centrifugation and washed two times with ethanol.

For preparing Pt<sub>1</sub>Ni, Pt<sub>2</sub>Ni, and Pt<sub>4</sub>Ni HU-NSs, 1 mL of 37.5, 18.8, and 9.4 mM  $\text{NiCl}_2 \cdot 6\text{H}_2\text{O}$  solution was injected in reaction mixture instead of 1 mL of 12.5 mM  $\text{NiCl}_2 \cdot 6\text{H}_2\text{O}$  solution, respectively.

#### **4.2.4. Synthesis of Pt<sub>3</sub>M (M= Co, Cu, Fe, Mn, Pd, Ir, Rh, and Ru) HU-NSs**

For the preparation of different Pt<sub>3</sub>M HU-NSs (M=Co, Cu, Fe, Mn, Pd, Ir, Rh, and Ru), 1 mL of 12.5

mM metal precursor (CoCl<sub>2</sub>·6H<sub>2</sub>O, CuCl<sub>2</sub>·6H<sub>2</sub>O, FeCl<sub>2</sub>·4H<sub>2</sub>O, MnCl<sub>2</sub>·4H<sub>2</sub>O, Na<sub>2</sub>PdCl<sub>4</sub>, IrCl<sub>3</sub>·xH<sub>2</sub>O, RhCl<sub>3</sub>·xH<sub>2</sub>O, RuCl<sub>3</sub>·xH<sub>2</sub>O) were used instead of NiCl<sub>2</sub>·6H<sub>2</sub>O, respectively, while other conditions are identical for synthesis of Pt<sub>3</sub>Ni HU-NSs.

#### 4.2.5. XAFS data analysis

The quantitative degree of alloying or atomic distribution in Pt<sub>3</sub>Ni HU-NSs was calculated quantitatively by analyzing the XAFS structural parameters. These parameters, necessary for determining the extent of alloying, are represented as  $P_{observed}$ ,  $P_{random}$ ,  $R_{observed}$ , and  $R_{random}$ .  $P_{observed}$  is defined as a ratio of the scattering atom B coordination-number (CN) atom around absorbing A atoms ( $N_{A-B}$ ) to the total CN of absorbing atoms ( $\sum N_{A-i}$ ). This calculation is represented as follows:  $P_{observed} = (\sum N_{A-B}) / (\sum N_{A-i})$ . On the other hand,  $R_{observed}$  is defined as an analogous calculation to  $P_{observed}$ , ( $R_{observed} = (\sum N_{B-A}) / (\sum N_{B-i})$ ). Furthermore, the  $P_{random}$  is the parameter of atom-A-based perfect bimetallic alloy under the ideal condition, which can be calculated from the atom number as follows:

$$P_{random} = (n_B / (n_A + n_B)) \times 100\% \quad (1)$$

$$R_{random} = (n_A / (n_A + n_B)) \times 100\% \quad (2)$$

We determined the extent of alloying of the Pt in Pt<sub>3</sub>Ni HU-NSs by evaluating the ratio of  $P_{observed}$  to  $P_{random}$ . Similarly, we estimated the alloying extent of the Ni in Pt<sub>3</sub>Ni HU-NSs by examining the ratio of  $R_{observed}$  to  $R_{random}$ . The quantitative calculation of the extent of alloying for Pt ( $J_A$ ) and Ni ( $J_B$ ) in the Pt<sub>3</sub>Ni HU-NSs is carried out using equations 3 and 4, respectively.

$$J_A = \frac{P_{observed}}{P_{random}} \times 100\% \quad (3)$$

$$J_B = \frac{R_{observed}}{R_{random}} \times 100\% \quad (4)$$

#### 4.2.6. Electrochemical measurements

Cyclic voltammetry (CV) and linear sweep voltammetry (LSV) measurements were carried out in a three-electrode cell using a multichannel potentiostat (EC-Lab Biologic SP-300) and a rotator (Pine instrument). A Pt mesh (1 cm<sup>2</sup>) connected with Pt wire and an Ag/AgCl (in 3M NaCl) were used as the counter and reference electrodes, respectively. A rotating disk electrode (RDE) containing a glassy

carbon disk (GC, 5 mm in diameter, E3TPK) was utilized as the working electrode. Electrochemical experiments were conducted at room temperature. Prior to electrochemical experiments, RDE was polished with 0.05  $\mu\text{m}$   $\text{Al}_2\text{O}_3$  bead solution and cleaned with deionized (DI) water. Catalyst ink was prepared by mixing a catalyst powder (~2.5 mg), DI water (2.0 mL), isopropyl alcohol (0.50 mL), and 5 wt% Nafion (10  $\mu\text{L}$ ). The catalyst ink was ultrasonicated for 30 min for preparation of working electrode. To prepare the working electrode, 10.0  $\mu\text{L}$  of the catalyst ink was dropped on GC disk of RDE and dried in an oven. The total Pt mass loadings on GC disk for all catalyst was 20.4  $\mu\text{g cm}^{-2}$ . CV was conducted in a potential cycle between 0.08 to 1.108  $V_{\text{RHE}}$  in an Ar-saturated 0.1 M  $\text{HClO}_4$  solution for 50 cycles at a scan rate of 100  $\text{mV s}^{-1}$  and final CV was recorded at a scan rate of 50  $\text{mV s}^{-1}$ .

Electrochemical surface area ( $\text{ECSA}_{\text{HUPD}}$ ) was determined through hydrogen underpotential deposition (HUPD) analysis of CV curves, where hydrogen adsorption/desorption peaks occurred in the potential region between 0.08 and 0.40  $V_{\text{RHE}}$ . The charges associated with the hydrogen adsorption/desorption area were first divided using a reference value of 210  $\mu\text{C cm}^{-2}$  and then further divided by the total mass of Pt loading.

ORR polarization curves were obtained in  $\text{O}_2$ -saturated 0.1 M  $\text{HClO}_4$  solution at 10  $\text{mV s}^{-1}$  and a rotating speed of 1600 rpm. All ORR polarization curves were  $iR$ -corrected. The Koutecky-Levich equation was used to obtain kinetic current density ( $j_k$ ):

$$\frac{1}{j} = \frac{1}{j_k} + \frac{1}{j_d}$$

$$j_k = \frac{(j \times j_d)}{j_d - j}$$

Where,  $j$  and  $j_d$  are the measured current density and the diffusion limiting current at certain potential, respectively. Accelerated durability tests (ADT) were conducted by cycling between 0.6 and 1.0  $V_{\text{RHE}}$  at a rate of 100  $\text{mV s}^{-1}$  for 5,000 and 10,000 cycles in an  $\text{O}_2$ -saturated 0.1 M  $\text{HClO}_4$  solution. After 5,000 and 10,000 cycles of ADT, the CV and ORR polarization curves were measured in a fresh 0.1 M  $\text{HClO}_4$  solution.

For CO-stripping tests, the surface of the catalysts on RDE was saturated with CO by purging CO gas

in 0.1 M HClO<sub>4</sub> while holding the working electrode at -0.05 V<sub>RHE</sub> for the 10 min and then the remaining CO was removed from solution by purging Ar gas for 30 min. The CO stripping voltammograms were obtained with a scan rate of 50 mVs<sup>-1</sup>.

#### **4.2.7 Characterization**

SEM images were obtained from a JEM-2100F (JEOL). TEM, HAADF-STEM, and EDS data were obtained with field-emission transmission electron microscopes (FEI Tecnai G2 F30 S-Twin operated at 300 kV and Talos F200X operated at 200 kV with Super-X system equipped with 4 EDS detectors) or a double Cs-corrected transmission electron microscope (Titan cubed G2 60-300 operated at 300 kV with Super-X system equipped with 4 EDS detectors) after placing a drop of diluted colloidal solution on a formvar/carbon-coated Cu or Ni grid (300 mesh). The compositions of nanostructures were determined by inductively coupled plasma-optical emission spectrometry (ICP-OES, Spectroblue-ICP-OES (Ametek)). X-ray diffraction (XRD) measurements were conducted on a Rigaku D/MAX2500V/PC using Cu K $\alpha$  (0.1542 nm) radiation. Ultraviolet photoelectron spectroscopy (UPS) and X-ray photoelectron spectroscopy (XPS) valence band measurements were conducted using a Thermo VG Scientific Sigma Probe spectrometer (light source = 1486.6 eV (Al K $\alpha$  X-ray)). The synchrotron-based X-ray absorption spectroscopy (EXAFS and XANES) analyses at Pt L3-edge and Ni K-edge were conducted with the 7D beamline located in the Pohang Accelerator Laboratory equipped with a Si (111) double-crystal monochromator (PLS-II, 3.0 GeV, Korea).

### 4.3. Result and Discussion

To produce the Pt<sub>3</sub>M HU-NSs, the Pt HU-NSs were first prepared through a slow reduction of K<sub>2</sub>PtCl<sub>4</sub> at a mild temperature (40 °C) in an aqueous reaction mixture containing cetyltrimethylammonium chloride (CTAC), poly(vinyl pyrrolidone) (PVP), and L-ascorbic acid (AA) that led to the anisotropic in-plane growth of Pt. **Figure 4.1.a** and **b** show the typical scanning electron microscopy (SEM) and transmission electron microscopy (TEM) images of the products, respectively, evidencing the successful massive production of Pt HU-NSs with porous 2D nanostructures. The shape evolution observed by TEM measurement indicated that Pt HU-NSs are formed by gradual growth of initially formed dendritic 2D nanostructures (**Figure 4.2.**). The average diagonal length of the Pt HU-NSs was determined as  $260 \pm 53$  nm. The thickness of the Pt HU-NSs was approximately 2.5 nm, which was acquired by a TEM image captured from the side-face of the Pt HU-NSs attached to a SiO<sub>2</sub> microbead (**Figure 4.1.c**). The high-angle annular dark-field scanning TEM (HAADF-STEM) image of a Pt HU-NS manifested their highly porous nature with  $0.6 \pm 0.4$  nm pore size (**Figure 4.1.d**). The high-magnification HAADF-STEM image showed that the lattice spacing of the Pt HU-NSs is 2.25 Å (**Figure 4.1.e**), which corresponds to the Pt(111) facet.<sup>40-43</sup> The low-coordinated surfaces such as {311} and {211} can be readily observed in the curved surfaces of Pt HU-NSs. The X-ray diffraction (XRD) pattern of the Pt HU-NSs indicates their highly crystalline feature with a face-centered cubic (fcc) Pt phase (**Figure 4.1.f**).



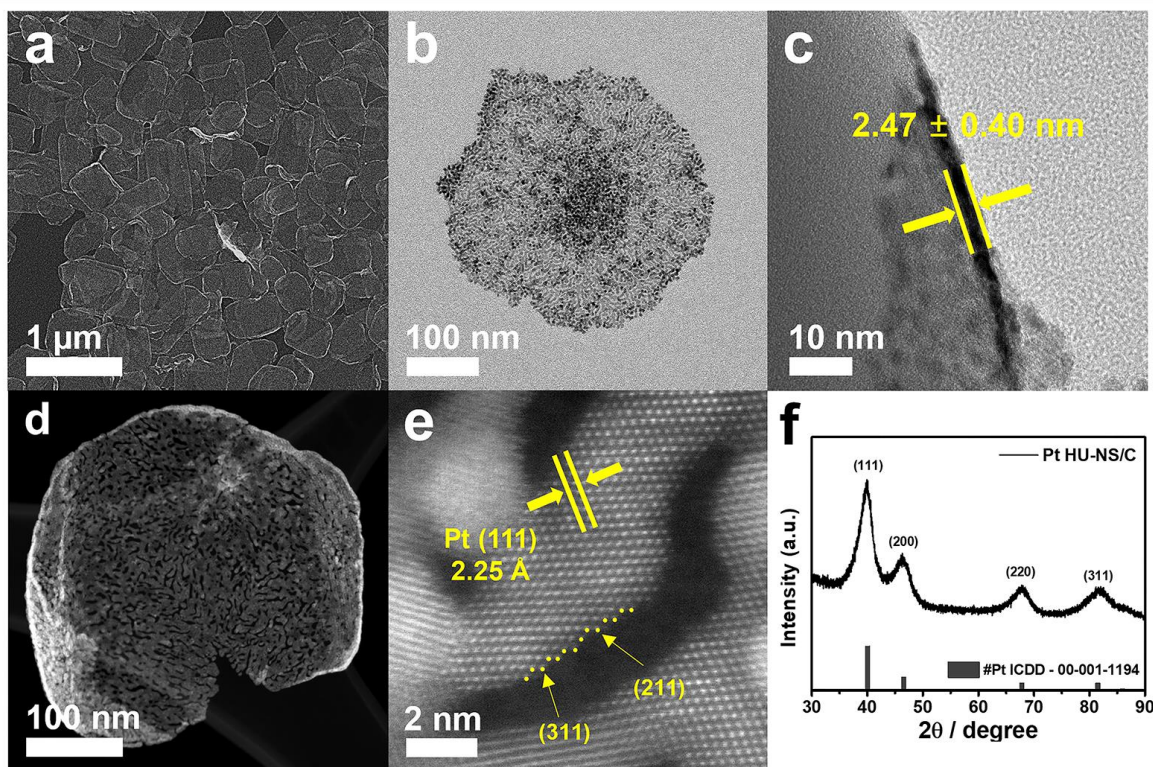


**Figure 4.1.** (a) SEM and (b, c) TEM images of Pt NSs. (d) low- and (e) high-magnification HAADF-STEM images of Pt HU-NSs. (f) XRD pattern of Pt HU-NSs.

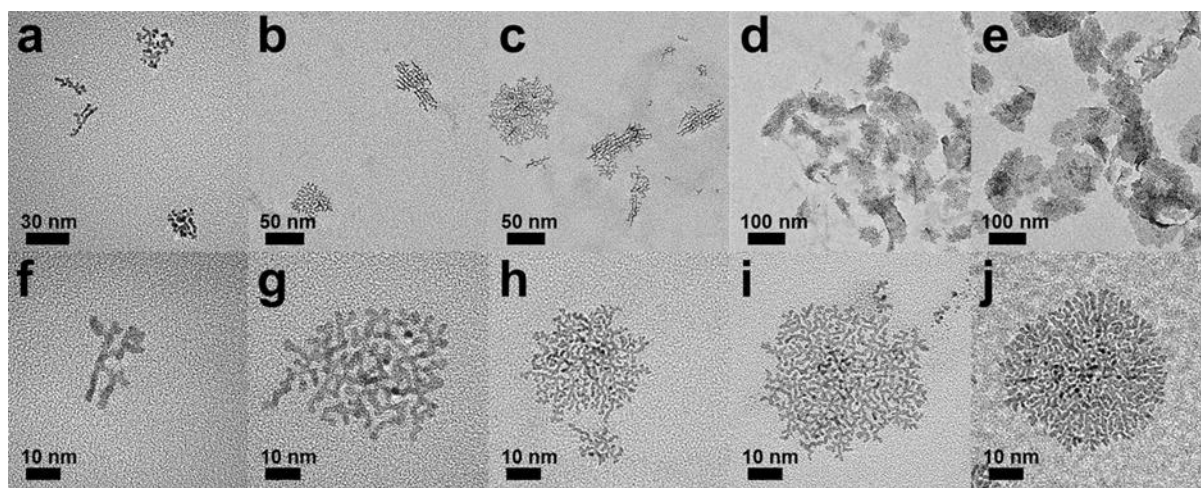


**Figure 4.2.** TEM images showing time dependent growth and shape evolution of Pt HU-NSs: reaction at (a, f) 15, (b, g) 20, (c, h) 25, (d, i) 30, and (e, j) 35 min.

The optimal thermal treatment (180 °C for 6 h) of the reaction mixture including as-prepared Pt HU-NSs, metal (Ni, Co, Cu, Fe, Mn, Pd, Ir, Rh, or Ru) precursors, AA, dimethylformamide (DMF), and PVP allowed the formation of Pt<sub>3</sub>M alloy, leading to the successful synthesis of the Pt<sub>3</sub>M HU-NSs. The atomic ratio of Pt-M HU-NSs can be controlled by changing the amount of metal precursors. **Figure 4.3.** presents the HAADF-STEM and corresponding energy dispersive spectroscopy (EDS) elemental mapping images of various Pt<sub>3</sub>M HU-NSs, which clearly exhibit the holey ultrathin 2D structures and the Pt-M alloy nature with homogeneous elemental distributions. The atomic ratios of Pt to M were determined using inductively coupled plasma optical emission spectrometry (ICP-OES) and EDS analysis (**Table 4.1.**), demonstrating the successful preparation of various Pt<sub>3</sub>M HU-NSs. The XRD patterns of the Pt<sub>3</sub>M HU-NSs exhibited highly crystalline fcc crystal structures (**Figure 4.4.**).

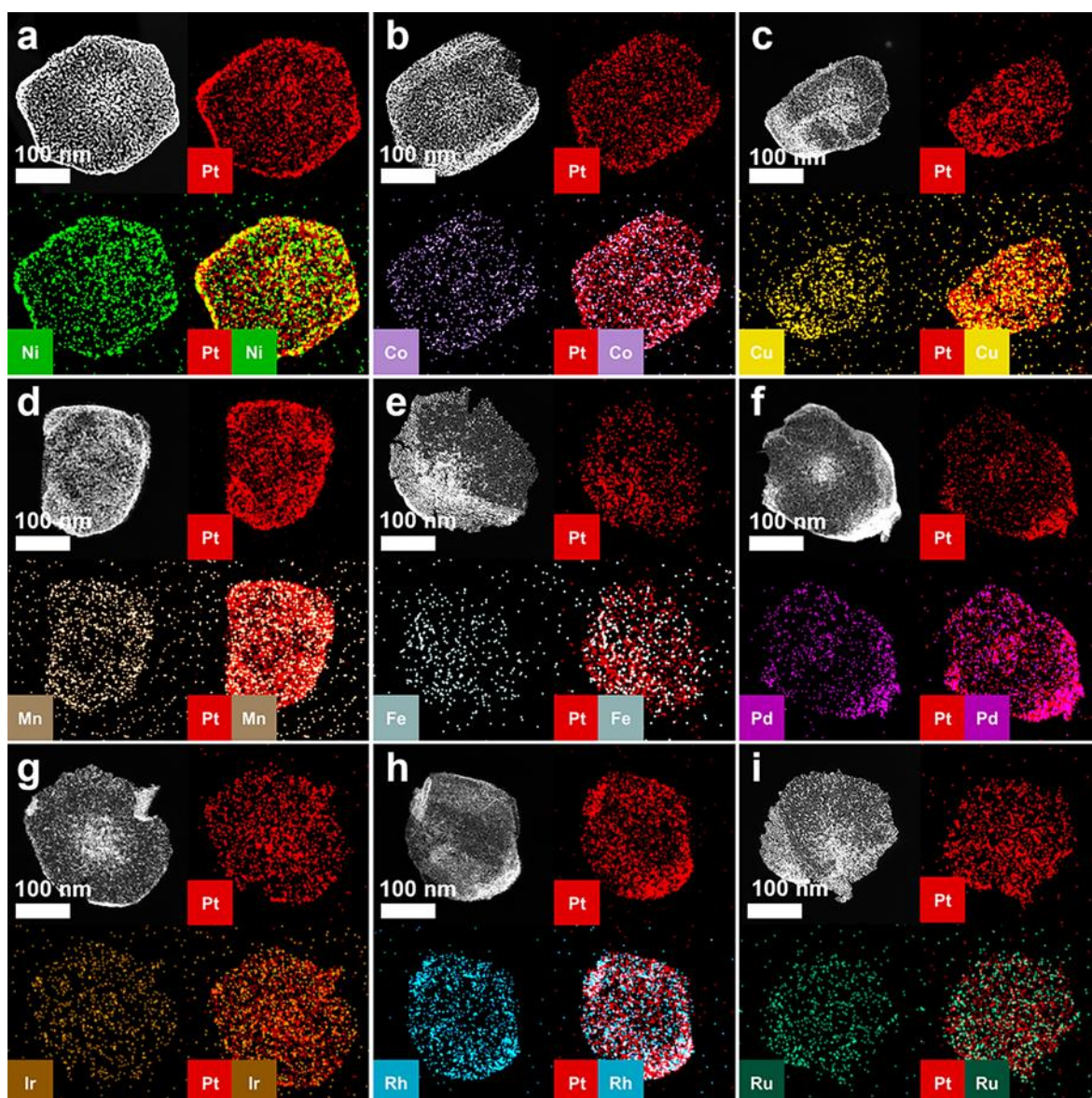


**Figure 4.3.** HAADF-STEM and corresponding EDS elemental mapping images of various  $\text{Pt}_3\text{M}$  HU-NSs. (a)  $\text{Pt}_3\text{Ni}$  HU-NSs. (b)  $\text{Pt}_3\text{Co}$  HU-NSs. (c)  $\text{Pt}_3\text{Cu}$  HU-NSs. (d)  $\text{Pt}_3\text{Mn}$  HU-NSs. (e)  $\text{Pt}_3\text{Fe}$  HU-NSs. (f)  $\text{Pt}_3\text{Pd}$  HU-NSs. (g)  $\text{Pt}_3\text{Ir}$  HU-NSs. (h)  $\text{Pt}_3\text{Rh}$  HU-NSs. (i)  $\text{Pt}_3\text{Ru}$  HU-NSs.

**Table 4.1.** Atomic ratio of Pt<sub>3</sub>M HU-NSs determined by ICP-OES and EDS analysis.

| <b>Catalysts</b>               | <b>ICP-OES analysis</b> | <b>EDS analysis</b> |
|--------------------------------|-------------------------|---------------------|
|                                | <b>(Pt/M)</b>           | <b>(Pt/M)</b>       |
| <b>Pt<sub>3</sub>Ni HU-NSs</b> | 2.94                    | 2.91                |
| <b>Pt<sub>3</sub>Co HU-NSs</b> | 2.95                    | 3.12                |
| <b>Pt<sub>3</sub>Cu HU-NSs</b> | 2.97                    | 2.89                |
| <b>Pt<sub>3</sub>Mn HU-NSs</b> | 2.87                    | 2.57                |
| <b>Pt<sub>3</sub>Fe HU-NSs</b> | 2.81                    | 2.92                |
| <b>Pt<sub>3</sub>Pd HU-NSs</b> | 2.78                    | 2.73                |
| <b>Pt<sub>3</sub>Ir HU-NSs</b> | 2.74                    | 2.83                |
| <b>Pt<sub>3</sub>Rh HU-NSs</b> | 2.91                    | 2.90                |
| <b>Pt<sub>3</sub>Ru HU-NSs</b> | 2.84                    | 2.81                |



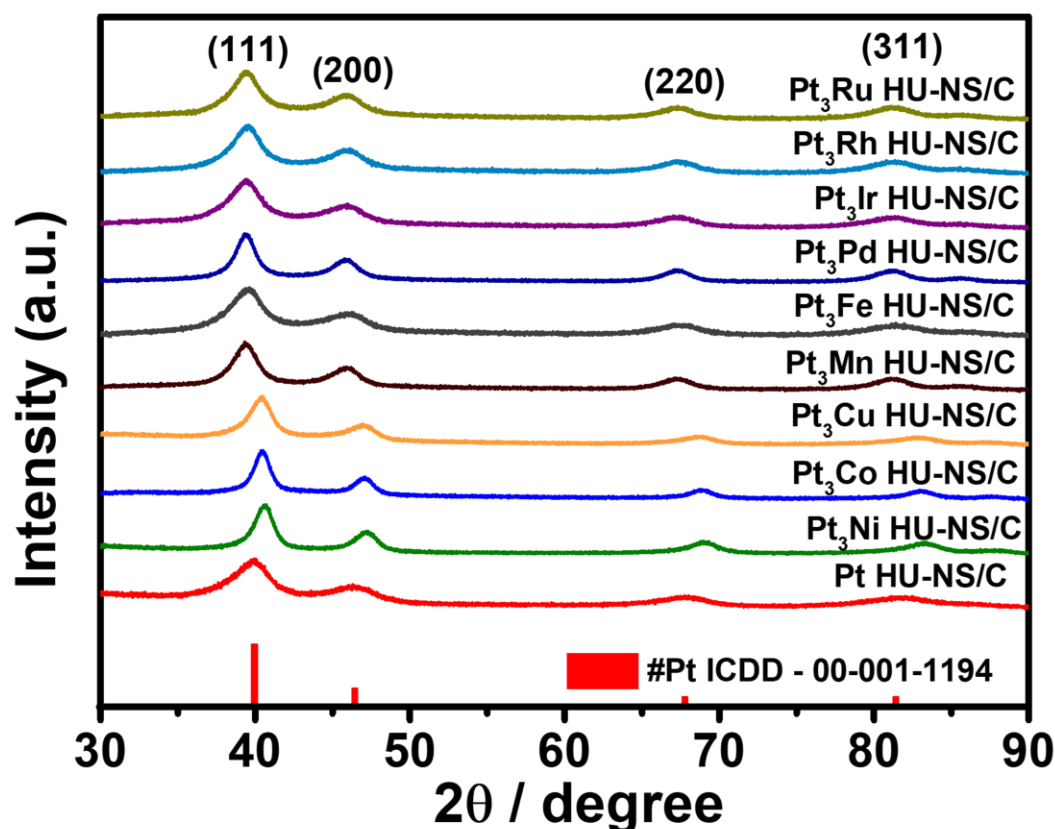


**Figure 4.4.** XRD patterns of various Pt<sub>3</sub>M HU-NSs. The red bars showing the reference of ICDD #00-001-1194 (Pt).

The structural and compositional features of the Pt<sub>3</sub>Ni HU-NSs were investigated by the SEM, HAADF-STEM, and TEM images, which demonstrated the well-preservation of ultrathin 2D morphology with a highly porous nature after thermal treatment (**Figure 4.5.a-c**). The diagonal length and pore size of the Pt<sub>3</sub>Ni HU-NSs were determined to be  $268 \pm 60$  and  $5.8 \pm 0.8$  nm by high-magnification HAADF-STEM and TEM images, respectively. The thickness of a Pt<sub>3</sub>Ni HU-NSs estimated by TEM measurements was  $3.39 \pm 0.36$  nm (**Figure 4.5.d**). The observed slight changes in thickness and pore size of Pt<sub>3</sub>Ni HU-NSs, as compared to pristine Pt HU-NSs, is attributed to the formation of a Pt-Ni alloy associated with the incorporation of Ni into the Pt HU-NSs. As shown in **Figure 4.5.e**, the lattice spacing of 2.19 Å is assigned to the (111) facets of fcc Pt-Ni,<sup>44-46</sup> and the low-coordinated edge atoms are also observed like the pristine Pt HU-NSs. The high-magnification EDS elemental mapping images revealed that Pt and Ni atoms are evenly distributed in the Pt<sub>3</sub>Ni HU-NS (**Figure 4.5.f**).

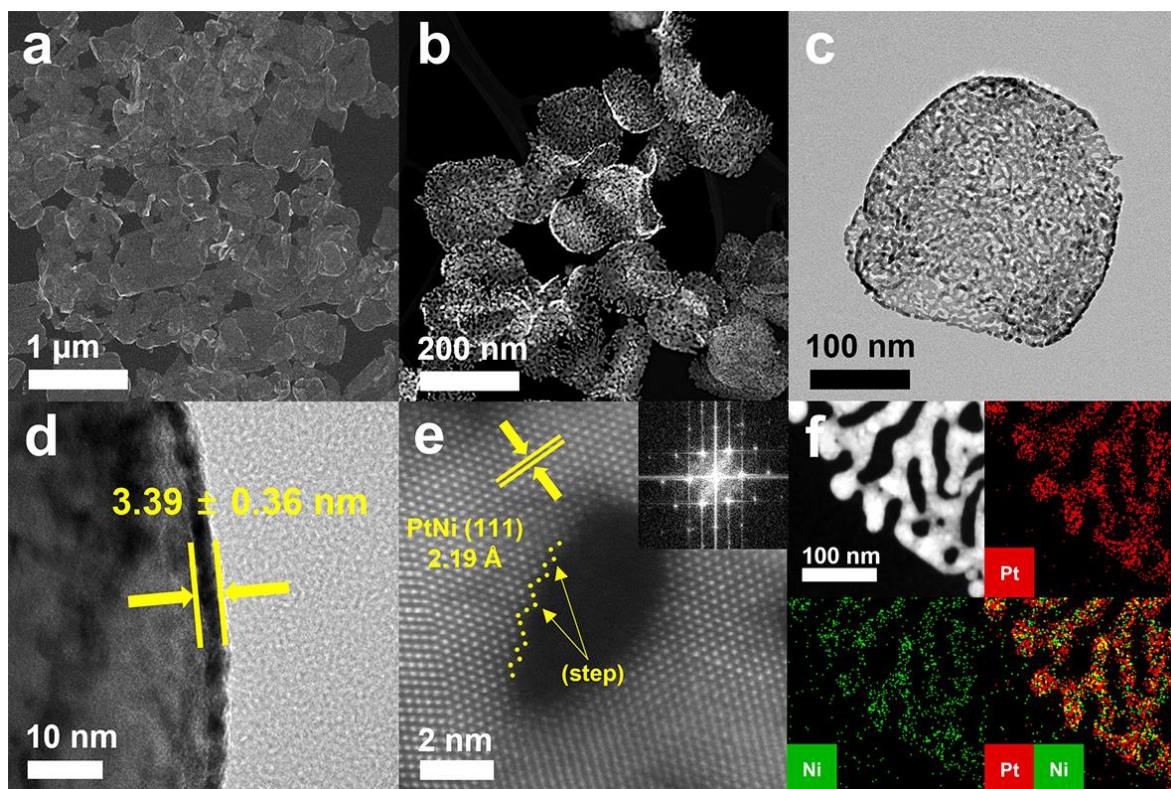


**Figure 4.5.** (a) SEM, (b) HAADF-STEM, and (c) TEM images of Pt<sub>3</sub>Ni HU-NSs. (d) TEM image of side-face of the Pt<sub>3</sub>Ni HU-NSs. (e) Atomic-resolution aberration corrected HAADF-STEM image of a Pt<sub>3</sub>Ni HU-NS and corresponding FFT pattern. (f) EDS elemental mapping images of a Pt<sub>3</sub>Ni HU-NS.

To further investigate the detailed compositional structure of Pt-Ni HU-NSs and their oxidation condition as well, the X-ray absorption near-edge structure (XANES) and the extended X-ray absorption fine structure (EXAFS) measurements were conducted. **Figure 4.6.a** shows the normalized Pt L<sub>3</sub>-edge XANES spectra of the Pt<sub>3</sub>Ni HU-NSs, Pt HU-NSs, and Pt foil. The oxidation state of the constituent can be estimated from the white line intensity in the XANES.<sup>25,47,48</sup> The Pt L<sub>3</sub>-edge XANES spectra revealed that the Pt HU-NSs exhibited a higher white line intensity compared to Pt foil, indicating a partial oxidation state of the Pt in the Pt HU-NSs. The higher white line intensity of the Pt HU-NSs is attributed to the higher portion of surface atom due to their thin thickness. In contrast, the white line intensity of the Pt<sub>3</sub>Ni HU-NSs closely resembled that of Pt foil, demonstrating that the Pt in Pt<sub>3</sub>Ni HU-NSs is in a predominantly metallic state. **Figure 4.6.b** shows the Ni K-edge XANES spectra of the Pt<sub>3</sub>Ni HU-NSs and Ni foil. The results verify that the Ni in the Pt<sub>3</sub>Ni HU-NSs is unambiguously in an oxidation state. These display that the oxidation states of Pt atoms in the in Pt<sub>3</sub>Ni HU-NSs can be

reduced by partial electron transfer from Ni atoms attributed to their Pt-Ni alloy phase. In addition, the Fourier transformed Pt L<sub>3</sub>-edge EXAFS spectra reflect that Pt<sub>3</sub>Ni HU-NSs manifest a shorter radial distance compared with those of Pt HU-NSs and Pt foil (**Figure 4.6.c**), implying the heteroatomic interaction between Pt and relatively smaller Ni atoms. Based on the coordination number (CN) information obtained from EXAFS spectra for the Pt<sub>3</sub>Ni HU-NSs, the alloying degree was determined to be J<sub>Pt</sub> (28.6%) and J<sub>Ni</sub> (99.4%), which matches well with the Pt/Ni atomic ratio of 3:1.<sup>49,50</sup> This observation indicates that a majority of Ni atoms is surrounded by Pt atoms, resulting in a uniform distribution of Ni atoms throughout the Pt nanosheets.

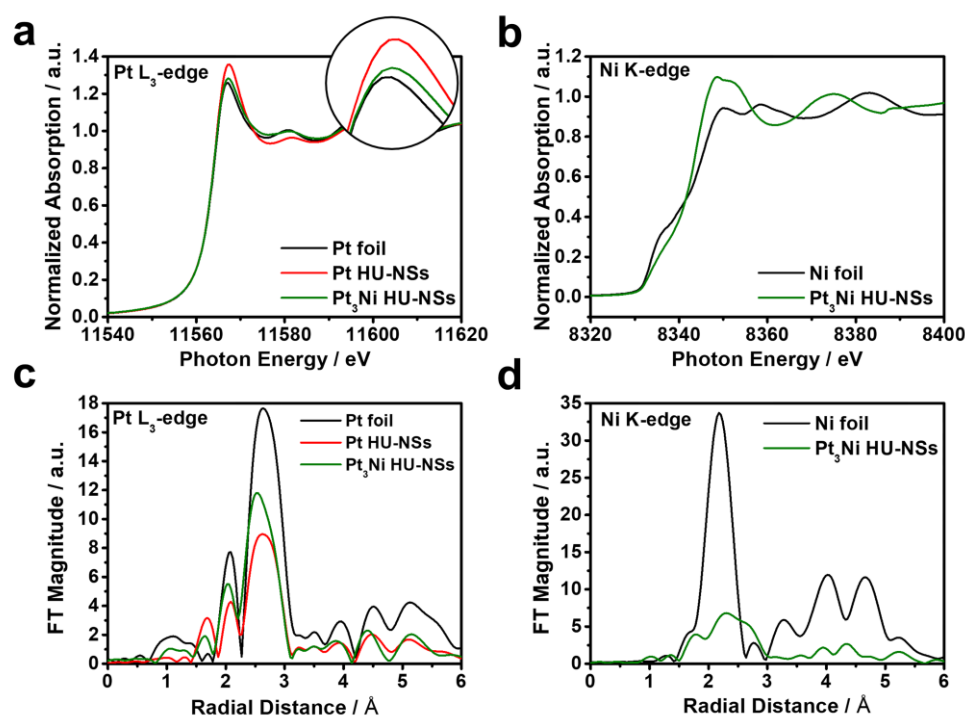


**Figure 4.6.** XAFS measurements for the Pt<sub>3</sub>Ni HU-NSs and Pt HU-NSs. XANES spectra at the (a) Pt L<sub>3</sub>-edge of the Pt<sub>3</sub>Ni HU-NSs, Pt HU-NSs, and Pt foil and (b) Ni K-edge of the Pt<sub>3</sub>Ni HU-NSs and Ni foil. Fourier-transformed  $k^3$ -weighted EXAFS spectra for (c) Pt L<sub>3</sub>-edge and (d) Ni K-edge of the catalysts.

The formation of Pt-M alloy through thermal treatment can be limited by the restrictive atomic diffusion depth of added metal atoms into the Pt template. To examine the importance of the thickness of Pt HU-NSs in the formation of Pt-M alloy HU-NSs, we conducted a comparative experiment using spherical

Pt nanocrystals (NCs) with a diameter of  $95 \pm 7$  nm as a Pt template (**Figure 4.7.a**). After subjecting the Pt NCs to thermal treatment with Ni precursors, it was observed that the core region of Pt NCs remained as pure Pt, while their shell regions of  $\sim 10$  nm underwent transformation into a Pt-Ni alloy, as observed in the EDS elemental mapping images (**Figure 4.7.b**). This result indicated the significance of the  $< 10$  nm thickness of the Pt HU-NSs in facilitating the formation of Pt-M HU-NSs.

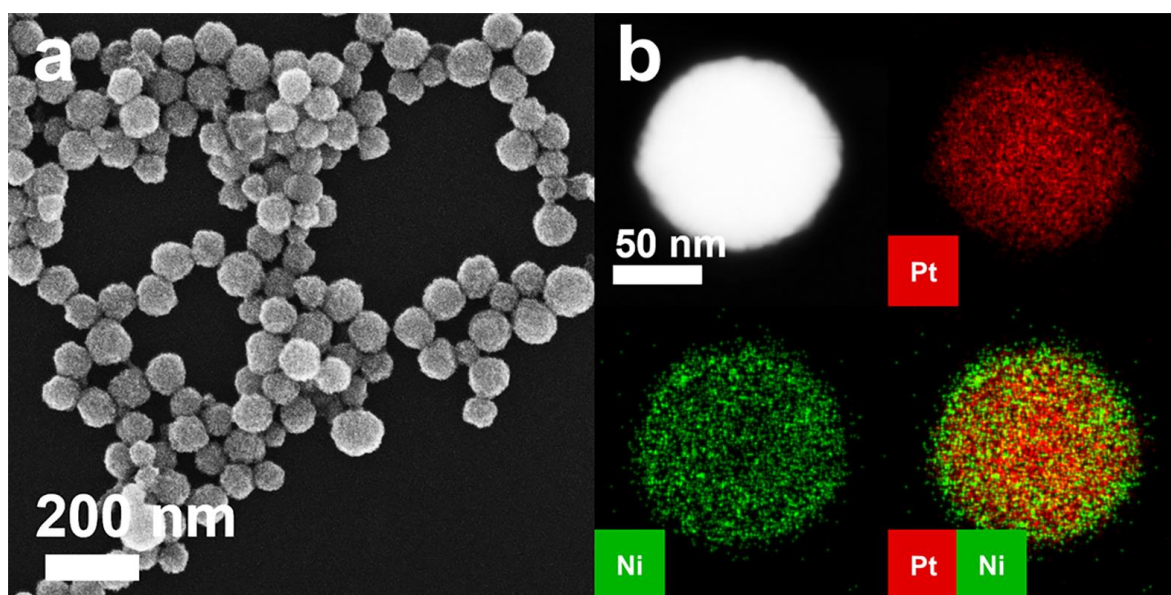


**Figure 4.7.** (a) SEM and (b) HAADF-STEM-EDS elemental mapping images of Pt-Ni NCs.

The optimal temperature and surfactants are essential for the synthesis of ultrathin 2D Pt HU-NSs by suppressing out-of-plane Pt growth and stabilizing the edge sites. The optimal temperature ( $40$  °C) leading to the formation of Pt HU-NSs was determined by observing the morphology of products formed under different reaction temperatures (**Figure 4.8.**). The insufficient reduction strength of  $K_2PtCl_4$  at a lower temperature than  $40$  °C led to irregularly shaped nanoparticles with several protrusions (**Figure 4.8.a**). In contrast, increasing the reaction temperature to  $40$  °C resulted in the formation of typical 2D Pt HU-NSs (**Figure 4.8.b**), while further increasing the temperature from  $50$  to  $100$  °C led to the gradual transformation of their 2D nanostructures into 3D morphologies (**Figure 4.8.c-f**). Besides the reaction temperature, it was found that the proper concentrations of PVP and CTAC also influence the formation of Pt HU-NSs (**Figure 4.9.**). These results demonstrated that the slow growth of Pt, achieved through precise control of reaction temperature and surfactant concentrations, plays a



crucial role in the formation of Pt HU-NSs. This controlled growth effectively suppressed the out-of-plane Pt growth, allowing for the successful synthesis of Pt HU-NSs with the desired structural characteristics.

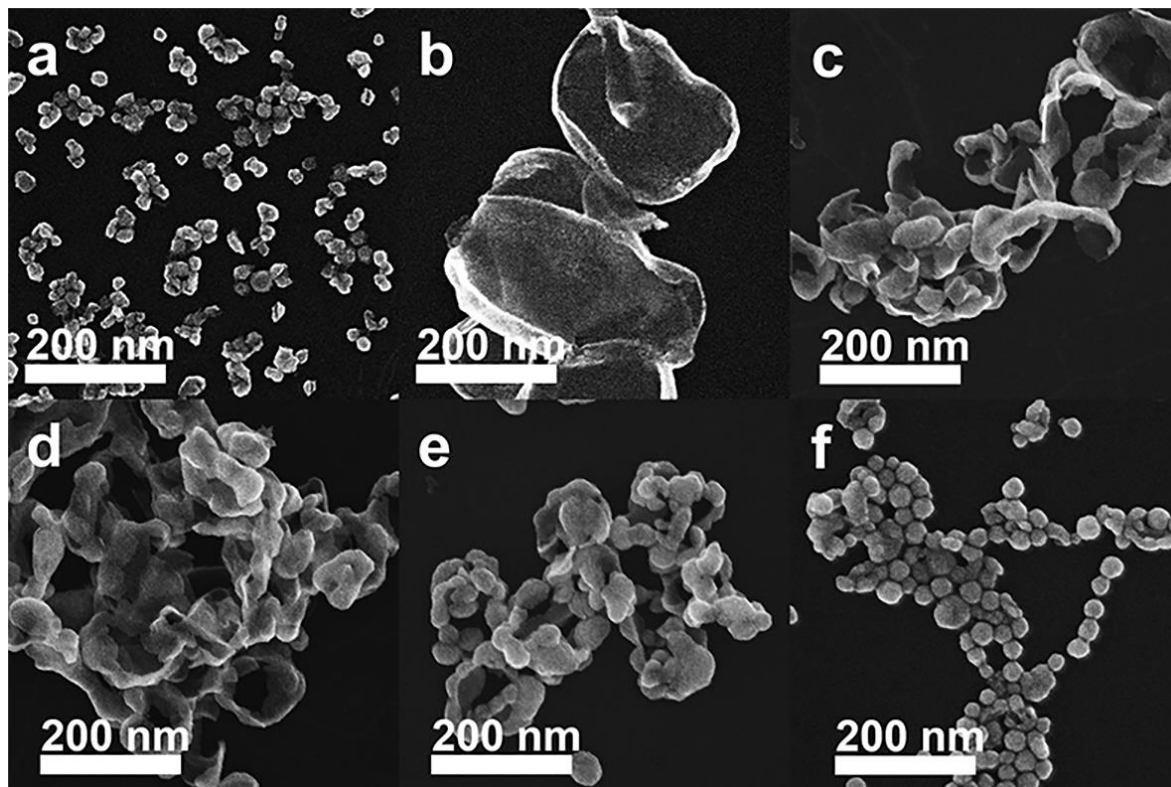


**Figure 4.8.** SEM images of Pt nanostructures with different reaction temperatures at (a) 30, (b) 40, (c) 50, (d) 60, (e) 80, and (f) 100 °C.

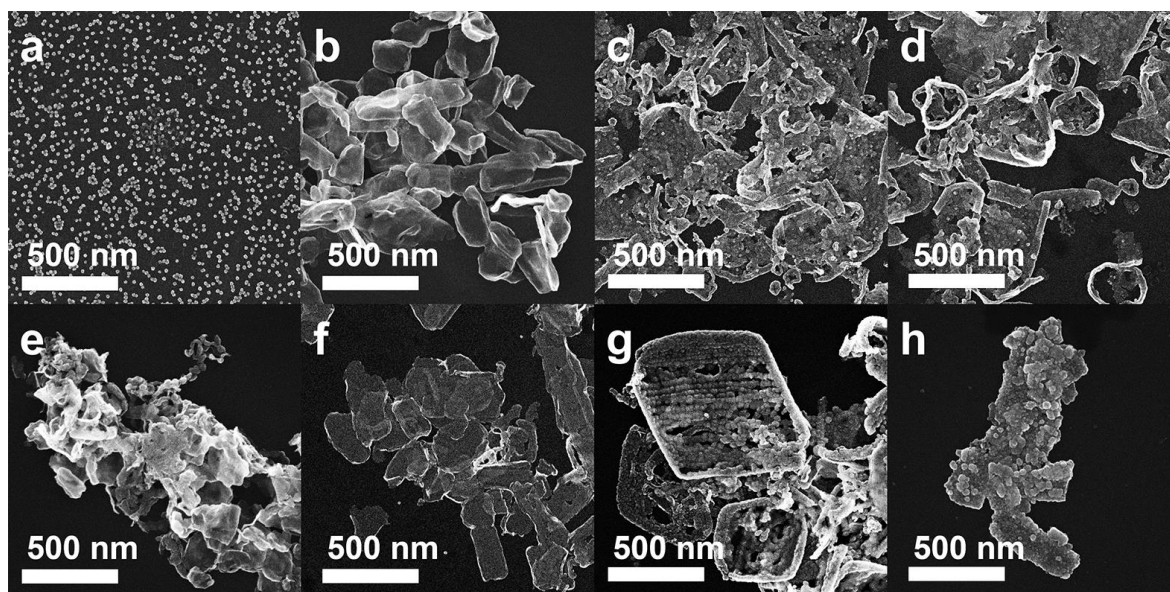


**Figure 4.9.** SEM images of nanostructures prepared with different amount of (a-d) CTAC and (e-h) PVP. For CTAC: (a) 0, (b) 50, (c) 200, and (d) 500 mM. For PVP: (e) 0, (f) 200, (g) 300, and (h) 400 mg.

To elucidate the formation mechanism of Pt-M alloy HU-NSs, a time-dependent analysis was conducted to track the structural and compositional evolution from Pt HU-NSs to Pt<sub>3</sub>Ni HU-NSs (**Figure 4.10**). **Figure 4.10.a-e,k,l** show that the pore size of Pt<sub>3</sub>Ni<sub>x</sub> HU-NSs ( $x = 0$  to  $\sim 1$ ) gradually increases as the atomic ratio of Ni increases in the Pt-Ni. The Pt HU-NSs ( $x = 0$ ) exhibited a pore size of  $0.6 \pm 0.4$  nm. In contrast, the intermediate products obtained at different reaction times of 30 (Pt<sub>3</sub>Ni<sub>0.52</sub>) and 90 min (Pt<sub>3</sub>Ni<sub>0.85</sub>) showed pore sizes of  $0.7 \pm 0.1$  and  $2.4 \pm 0.5$  nm, respectively. The Pt/Ni atomic ratio and pore size of the products obtained at reaction time of 270 min were Pt<sub>3</sub>Ni<sub>0.93</sub> and  $5.6 \pm 1.1$  nm, respectively, which are similar to those of typical Pt<sub>3</sub>Ni HU-NSs. These results indicated that Pt/Ni atomic ratio and pore size of HU-NSs are mostly converged at reaction time of 270 min. Accompanying the change in pore size, the thickness of the HU-NSs also continuously increased from 2.47 to 3.39 nm (**Figure 4.10.f-l**). Based on the evolution process of Pt<sub>3</sub>Ni HU-NSs, we suggest that Pt atoms are initially leached from the surface of HU-NS by the oxidative etching process, generating the Pt ions. Subsequently, the Ostwald ripening process promotes the co-deposition of the Ni precursor and Pt ions on the basal planes. Finally, the interatomic diffusion of Pt and Ni atoms leads to the formation of Pt-

Ni alloy HU-NSs. Consequently, the larger pore size and thickness of Pt<sub>3</sub>Ni HU-NSs compared to those of Pt HU-NSs can be obtained.

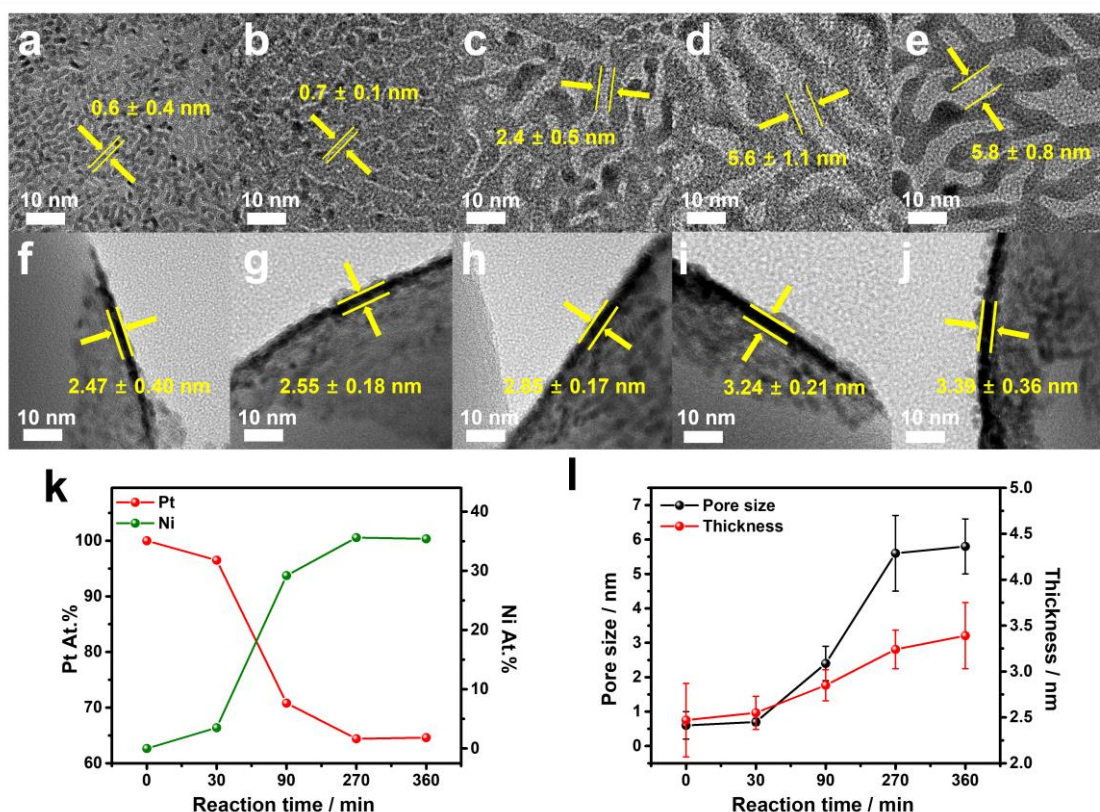


**Figure 4.10.** TEM images showing the time dependent transformation from Pt HU-NSs to Pt<sub>3</sub>Ni HU-NSs; (a, f) 0, (b, g) 30, (c, h) 90, (d, i) 270, and (e, j) 360 min. Changes in the (k) composition of metal elements, (l) pore size, and thickness of intermediate products during the reaction.

The electrocatalytic ORR performances of carbon-supported Pt<sub>3</sub>M HU-NSs (Pt<sub>3</sub>M HU-NS/C) were investigated using cyclic voltammetry (CV) and rotating disk electrode (RDE) techniques with a three-electrode electrochemical system. Electrochemically active surface area (ECSA), specific activity, and mass activity were obtained to evaluate the catalytic performance of Pt<sub>3</sub>M HU-NS/C and were compared with those of pristine Pt HU-NS/C and commercial Pt/C (20 wt% of Pt loaded on Vulcan carbon). The CV measurement was performed at a scan rate of 50 mV s<sup>-1</sup> in an Ar-saturated 0.1 M HClO<sub>4</sub> solution with a potential ranging between 0.08 and 1.108 vs. reversible hydrogen electrode (V<sub>RHE</sub>).<sup>51-54</sup> The CV curves of the catalysts shown in **Figure 4.11.a** display that hydrogen adsorption/desorption peaks

appeared in the region from 0.08 to 0.4  $V_{RHE}$ , and oxygen adsorption/desorption peaks appeared in the region from 0.60 to 1.108  $V_{RHE}$ .<sup>51-54</sup> The ECSA was evaluated by the hydrogen underpotential deposition (HUPD) analysis. Notably, all HU-NSs showed comparable ECSA values (40.02 – 52.32  $m^2 g^{-1}$ ) with that of Pt/C (59.70  $m^2 g^{-1}$ ) due to their porous 2D shape with ultrathin thicknesses (**Table 4.2.**). The ORR polarization curves of the catalysts were obtained in  $O_2$ -saturated 0.1 M  $HClO_4$  solutions using the RDE as a working electrode and the resulting linear sweep voltammetry (LSV) curves were normalized by the geometric surface area of electrode (0.196  $cm^2$ ) (**Figure 4.11.b**). The  $Pt_3Ni$ ,  $Pt_3Co$ ,  $Pt_3Cu$ ,  $Pt_3Mn$ , and  $Pt_3Pd$  HU-NS/C exhibited higher mass and specific activities compared to both commercial Pt/C and Pt HU-NS/C (**Figure 4.11.c** and **Table 4.2.**). The  $Pt_3Ni$  HU-NS/C showed a mass activity of 2.27  $A mg^{-1}Pt$ , which is 4.4 and 10 times higher than those of Pt HU-NS/C (0.52  $A mg^{-1}Pt$ ) and Pt/C (0.23  $A mg^{-1}Pt$ ) at 0.9  $V_{RHE}$ , respectively. Moreover,  $Pt_3Ni$  HU-NS/C showed a specific activity of 4.71  $mA cm^{-2}_{ECSA}$ , which is 4.0 and 12.1 times higher than those of Pt HU-NS/C and Pt/C at 0.9  $V_{RHE}$ , respectively.

To further investigate the impact of alloy composition on ORR, Pt-Ni HU-NSs with varying Pt/Ni ratio of  $Pt_1Ni$ ,  $Pt_2Ni$ , and  $Pt_4Ni$  were prepared. Figure 4e shows the ORR polarization curves of the Pt-Ni HU-NS/C samples. The mass activities for  $Pt_1Ni$ ,  $Pt_2Ni$ , and  $Pt_4Ni$  HU-NS/C were 1.12, 1.64, and 1.34  $A mg^{-1}Pt$ , respectively (**Figure 4.11.e,f**). These results indicated that the Pt/Ni atomic ratio of 3/1 is the optimal composition for improving electrocatalytic ORR, which is also consistent with previous results.<sup>44,55-59</sup>

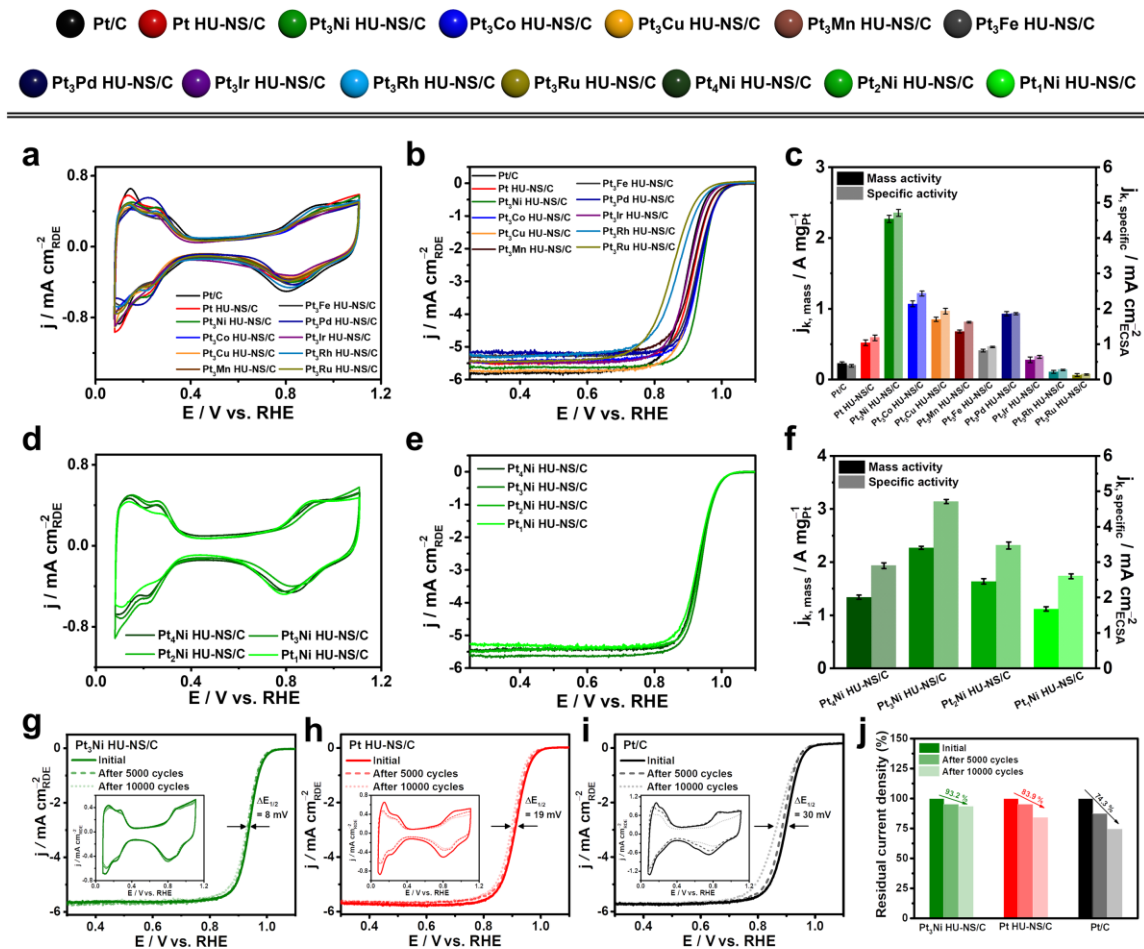


**Figure 4.11.** Electrochemical properties of different catalysts. (a) CVs and (b) ORR curves of different catalysts. (c) Mass activity and specific activities of different catalysts at 0.9V<sub>RHE</sub>. (d) CVs and (e) ORR curves of Pt-Ni alloy catalysts with different Pt/Ni atomic ratios and (f) corresponding mass activity and specific activities of the catalysts at 0.9V<sub>RHE</sub>. ORR curves for (g) Pt<sub>3</sub>Ni HU-NS/C, (h) Pt HU-NS/C, and (i) commercial Pt/C catalysts before and after 5000 and 10000 cycles in an O<sub>2</sub>-saturated 0.1 M HClO<sub>4</sub> solution. The insets displaying the CVs before and after the durability test for each catalyst. (j) Bar graph showing changes in specific activities before and after durability test for each catalyst.

**Table 4.2.** The ECSA, Mass and specific activities of Pt<sub>3</sub>M HU-NS/C, Pt HU-NS/C, and Pt/C.

| Catalyst                   | ECSA $H_{\text{UPD}}$<br>( $\text{m}^2 \text{g}^{-1}_{\text{Pt}}$ ) | Mass Activity<br>( $\text{A mg}^{-1}_{\text{Pt}}$ ) | Specific Activity<br>( $\text{mA cm}^{-2}_{\text{ECSA}}$ ) |
|----------------------------|---|---|--|
| Pt <sub>3</sub> Ni HU-NS/C | 48.42   | 2.27  | 4.71   |
| Pt <sub>3</sub> Co HU-NS/C | 43.64   | 1.07  | 2.43   |
| Pt <sub>3</sub> Cu HU-NS/C | 44.26   | 0.85  | 1.93   |
| Pt <sub>3</sub> Mn HU-NS/C | 43.99   | 0.68  | 1.62   |
| Pt <sub>3</sub> Fe HU-NS/C | 42.02   | 0.41  | 0.92   |
| Pt <sub>3</sub> Pd HU-NS/C | 51.19   | 0.93  | 1.86   |
| Pt <sub>3</sub> Ir HU-NS/C | 42.76   | 0.28  | 0.64   |
| Pt <sub>3</sub> Rh HU-NS/C | 40.88   | 0.11  | 0.27   |
| Pt <sub>3</sub> Ru HU-NS/C | 45.61   | 0.07  | 0.14   |
| Pt HU-NS/C                 | 52.32   | 0.52  | 1.18   |
| Pt/C                       | 59.70   | 0.23  | 0.39   |

An accelerated durability test (ADT) was conducted for Pt<sub>3</sub>Ni HU-NS/C, Pt HU-NS/C, and Pt/C catalysts under a scan rate of 100 mV s<sup>-1</sup> between 0.6 and 1.0 V<sub>RHE</sub> in an O<sub>2</sub>-saturated 0.1 M HClO<sub>4</sub> solution for 5,000 and 10,000 cycles. To assess the stability, CVs and ORR polarization curves before and after ADT were measured (**Figure 4.11.g-i**). After 5000 cycles, Pt<sub>3</sub>Ni and Pt HU-NS/C showed stable performances, whereas commercial Pt/C showed slightly decreased ORR performance. After 10000 cycles, the E<sub>1/2</sub> values for the Pt<sub>3</sub>Ni HU-NS/C, Pt HU-NS/C, and Pt/C shifted negatively to 8, 19,

and 30 mV compared to the initial values, respectively (**Figure 4.11.g-i**). The specific activity of the Pt<sub>3</sub>Ni HU-NS/C, Pt HU-NS/C, and Pt/C catalysts retained 93.2, 83.9, and 74.4% of their initial activity, respectively (**Figure 4.11.j**). Notably, the specific activity of Pt<sub>3</sub>Ni HU-NS/C remained 4.4 and 15.1 times higher than that of Pt HU-NS/C and Pt/C, respectively, after the cycling process. A STEM image obtained after the ADT verified that the Pt<sub>3</sub>Ni HU-NS/C maintains its morphology during the harsh conditions of test. The EDS-determined Pt/Ni atomic ratio of the Pt<sub>3</sub>Ni HU-NS/C after the ADT was 3.12/1, which is slightly higher than that of the fresh samples. This indicated that the slight decrease in ORR activity of the Pt<sub>3</sub>Ni HU-NSs after 10,000 cycles can be attributed to the leaching of Ni from the Pt<sub>3</sub>Ni HU-NS/C.

The ultraviolet photoelectron spectroscopy (UPS) measurements were conducted to investigate the d-band center of the Pt<sub>3</sub>Ni HU-NSs, Pt HU-NSs, and Pt/C, since the surface electronic structure plays a crucial role in the adsorption/desorption behavior of adsorbates in electrocatalysis. Compared to the Pt/C, Pt HU-NSs exhibited a lower d-band center (**Figure 4.12.a**) due to the ultrathin thickness and the surface containing a high density of low-coordinated atoms.<sup>29,47,54,60-62</sup> Furthermore, Pt<sub>3</sub>Ni HU-NSs showed an even more downshifted d-band center compared to Pt HU-NSs, which can be attributed to the formation of the Pt-Ni alloy (**Figure 4.12.a**). An identical trend was observed in X-ray photoelectron spectroscopy (XPS) valence-band spectra of the catalysts (**Figure 4.12.b**). The lower d-band center of the Pt<sub>3</sub>Ni HU-NSs leads a weakened bonding strength for oxygen-containing intermediates produced during ORR compared to pure Pt catalysts. As the lower d-band center facilitates faster desorption of the intermediates, the Pt<sub>3</sub>Ni HU-NSs shows enhanced ORR activity. To validate the enhancement of ORR performance for Pt<sub>3</sub>Ni HU-NS/C associated with the downshift of the d-band center, we conducted CO stripping experiment, which can provide an indirect assessment of the bonding strength of oxygen-containing species on the catalyst surface.<sup>15,60,61,63-66</sup> The Pt<sub>3</sub>Ni HU-NSs exhibited a CO stripping peak at a lower potential compared to Pt HU-NCs and Pt/C, suggesting a weaker bonding strength between the Pt<sub>3</sub>Ni HU-NSs and oxygen-containing species in comparison to Pt HU-NS/C and Pt/C catalysts (**Figure 4.12.c**). Taken together, the superior ORR performance of Pt<sub>3</sub>Ni HU-NS/C compared to Pt HU-NS/C and commercial Pt/C can be attributed to several factors. These include the large number of active

sites and edge atoms associated with the ultrathin holey 2D shape, as well as the downshift in the Pt d-band center resulting from the formation of the Pt-Ni alloy and surface coordination environment. These factors collectively promoted the optimal bond strength of intermediates during ORR relative to pure Pt catalysts, accelerating the desorption of intermediates and facilitating water formation. As a result, Pt<sub>3</sub>Ni HU-NS/C demonstrated exceptional ORR performance compared to the other catalysts evaluated in this study.

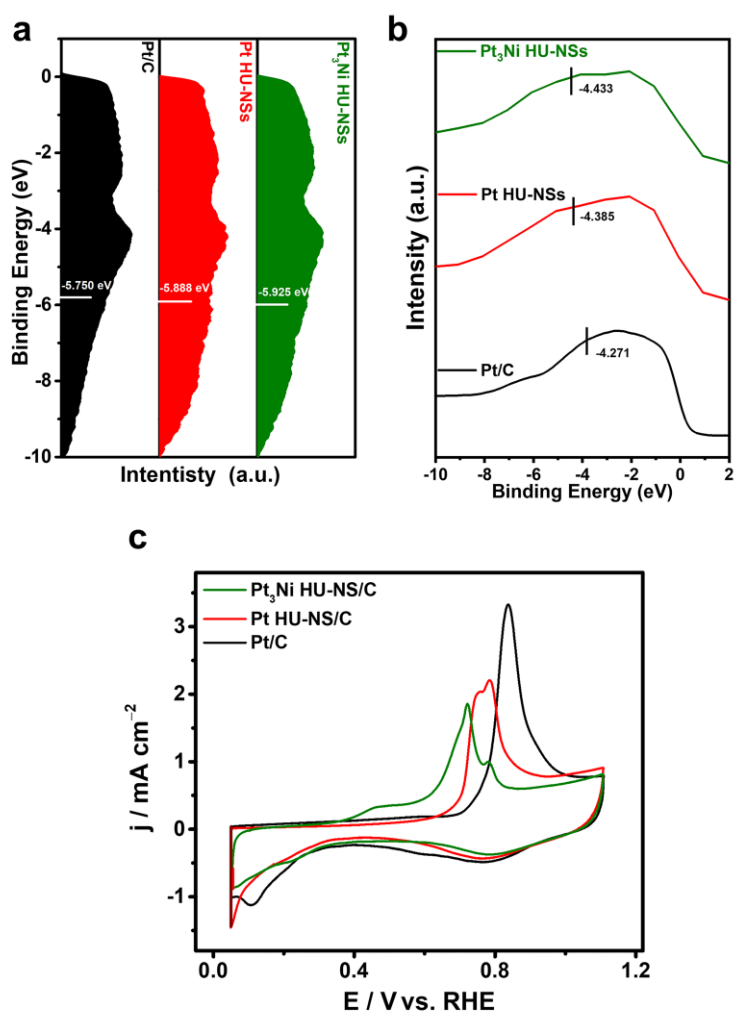


**Figure 4.12.** (a) UPS and (b) XPS valence-band spectra of Pt<sub>3</sub>Ni HU-NSs, Pt HU-NSs, and Pt/C. (c) CO-stripping voltammogram of the catalysts.



#### 4.4 Conclusion

In summary, we have successfully developed a universal synthesis method for preparing Pt<sub>3</sub>M alloy HU-NSs with ultrathin thickness and abundant edge sites. The preparation of Pt HU-NSs through a slow Pt growth rate and the preservation of their morphology during the formation of Pt<sub>3</sub>M alloy HU-NSs through controlled thermal treatment are critical factors in the successful synthesis of Pt<sub>3</sub>M alloy HU-NSs. Pt<sub>3</sub>Ni HU-NSs exhibited an outstanding ORR performance due to their abundant active sites and distinctive surface including edge-rich atoms associated with their holey ultrathin 2D shape, along with a downshift in the d-band center resulting from the formation of Pt-Ni alloy and surface coordination environment. We anticipate that our innovative approach can be extended to the synthesis of other 2D alloy nanostructures with enriched edge sites, paving the way for the development of highly efficient catalyst systems.

#### 4.5. References

1. Hong, J.W., Kim, Y., Wi, D.H., Lee, S., Lee, S.U., Lee, Y.W., Choi, S.I., and Han, S.W., *Angew. Chem. Int. Ed.*, **2016**, 55, 2753-2758.
2. Hussain, N., Liang, T., Zhang, Q., Anwar, T., Huang, Y., Lang, J., Huang, K., and Wu, H., *Small*, **2017**, 13, 1701349.
3. Takimoto, D., Ohnishi, T., Nutariya, J., Shen, Z., Ayato, Y., Mochizuki, D., Demortière, A., Boulineau, A., and Sugimoto, W., *J. Catal.*, **2017**, 345, 207-215.
4. Liu, H.-M., Han, S.-H., Zhao, Y., Zhu, Y.-Y., Tian, X.-L., Zeng, J.-H., Jiang, J.-X., Xia, B.Y., and Chen, Y., *J. Mater. Chem. A*, **2018**, 6, 3211-3217.
5. Luo, M., Zhao, Z., Zhang, Y., Sun, Y., Xing, Y., Lv, F., Yang, Y., Zhang, X., Hwang, S., Qin, Y., et al. *Nature*, **2019**, 574, 81-85.
6. Liu, B., Han, Q., Li, L., Zheng, S., Shu, Y., Pedersen, J.A., and Wang, Z., *Environ. Sci. Technol.*, **2021**, 55, 16379-16389.
7. Yu, H., Zhou, T., Wang, Z., Xu, Y., Li, X., Wang, L., and Wang, H., *Angew. Chem. Int. Ed.*, **2021**, 60, 12027-12031.
8. Wu, G., Han, X., Cai, J., Yin, P., Cui, P., Zheng, X., Li, H., Chen, C., Wang, G., and Hong, X., *Nat. Commun.*, **2022**, 13, 4200.
9. Kuang, Y., Feng, G., Li, P., Bi, Y., Li, Y., and Sun, X., *Angew. Chem. Int. Ed.*, **2016**, 55, 693-697.
10. Han, Y., Kim, J., Lee, S.U., Choi, S.I., and Hong, J.W., *Chem Asian J.*, **2020**, 15, 1324-1329.
11. Peng, X., Lu, D., Qin, Y., Li, M., Guo, Y., and Guo, S., *ACS Appl. Mater. Interfaces*, **2020**, 12, 30336-30342.
12. Chen, Q., Chen, Z., Ali, A., Luo, Y., Feng, H., Luo, Y., Tsiakaras, P., and Kang Shen, P., *Chem. Eng. J.*, **2022**, 427, 131565.
13. Gu, B.S., Dutta, S., Hong, Y.R., Ngome Okello, O.F., Im, H., Ahn, S., Choi, S.Y., Woo Han, J., Ryu, S., and Lee, I.S., *Angew. Chem. Int. Ed.*, **2023**, 62, e202307816.
14. Takimoto, D., Toma, S., Suda, Y., Shirokura, T., Tokura, Y., Fukuda, K., Matsumoto, M., Imai, H., and Sugimoto, W., *Nat. Commun.*, **2023**, 14, 19.
15. Liu, Y., Cheng, H., Lyu, M., Fan, S., Liu, Q., Zhang, W., Zhi, Y., Wang, C., Xiao, C., Wei, S., et al., *J. Am. Chem. Soc.*, **2014**, 136, 15670-15675.
16. Yang, N., Zhang, Z., Chen, B., Huang, Y., Chen, J., Lai, Z., Chen, Y., Sindoro, M., Wang, A.L., Cheng, H.,

- et al., *Adv. Mater.*, **2017**, 29, 1700769. 10.1002/adma.201700769.
17. Zhang, Q., Li, P., Zhou, D., Chang, Z., Kuang, Y., and Sun, X., *Small*, **2017**, 13, 1701648.
  18. Chen, H.Y., Jin, M.X., Zhang, L., Wang, A.J., Yuan, J., Zhang, Q.L., and Feng, J.J., *J. Colloid Interface Sci.*, **2019**, 543, 1-8.
  19. Wang, Z., Xiao, B., Lin, Z., Xu, Y., Lin, Y., Meng, F., Zhang, Q., Gu, L., Fang, B., Guo, S., and Zhong, W., *Angew. Chem. Int. Ed.*, **2021**, 60, 23388-23393.
  20. Li, C., Gao, F., Ren, Y., Li, B., Li, L., Lu, Z., Yang, X., Zhang, X., and Yu, X., *ACS Appl. Nano Mater.*, **2022**, 5, 1192-1199.
  21. Nanba, Y., and Koyama, M., *Computational Materials Science*, **2022**, 203, 111132.
  22. Calle-Vallejo, F., Pohl, M.D., Reinisch, D., Loffreda, D., Sautet, P., and Bandarenka, A.S., *Chem. Sci.*, **2017**, 8, 2283-2289.
  23. Guo, J., Gao, L., Tan, X., Yuan, Y., Kim, J., Wang, Y., Wang, H., Zeng, Y.J., Choi, S.I., Smith, S.C., and Huang, H., *Angew. Chem. Int. Ed.*, **2021**, 60, 10942-10949.
  24. Guo, K., Fan, D., Bao, J., Li, Y., and Xu, D., *Adv. Funct. Mater.*, **2022**, 32, 2208057.
  25. Xia, T., Zhao, K., Zhu, Y., Bai, X., Gao, H., Wang, Z., Gong, Y., Feng, M., Li, S., Zheng, Q., et al., *Adv. Mater.*, **2023**, 35, e2206508.
  26. Calle-Vallejo, F., Tymoczko, J., Colic, V., Loffreda, D., Schuhmann, W., and Bandarenka, A.S., *Science*, **2015**, 350, 185-188.
  27. Lai, J., Lin, F., Tang, Y., Zhou, P., Chao, Y., Zhang, Y., and Guo, S., *Adv. Energy Mater.*, **2019**, 9, 1800684.
  28. Li, M., Tian, F., Lin, T., Tao, L., Guo, X., Chao, Y., Guo, Z., Zhang, Q., Gu, L., Yang, W., et al., *Small Methods*, **2021**, 5, e2100154.
  29. Lin, F., Lv, F., Zhang, Q., Luo, H., Wang, K., Zhou, J., Zhang, W., Zhang, W., Wang, D., Gu, L., and Guo, S., *Adv. Mater.*, **2022**, 34, e2202084.
  30. Ao, W., Ren, H., Cheng, C., Fan, Z., Yin, P., Qin, Q., Zhang, Q., and Dai, L., *Angew. Chem. Int. Ed.*, **2023**, 62, e202305158.
  31. Li, C., Clament Sagaya Selvam, N., and Fang, J., *Nanomicro Lett.*, **2023**, 15, 83.
  32. Sun, Y., Zhang, X., Luo, M., Chen, X., Wang, L., Li, Y., Li, M., Qin, Y., Li, C., Xu, N., et al., *Adv. Mater.*, **2018**, 30, e1802136.
  33. Jang, H.J., Ham, S., Acapulco, J.A., Jr., Song, Y., Hong, S., Shuford, K.L., and Park, S., *J. Am. Chem. Soc.*, **2014**, 136, 17674-17680.

34. Kang, Y., Jiang, B., Malgras, V., Guo, Y., Cretu, O., Kimoto, K., Ashok, A., Wan, Z., Li, H., Sugahara, Y., et al., *Small Methods*, **2021**, 5, e2100679.
35. Li, Y., Cheng, C., Han, S., Huang, Y., Du, X., Zhang, B., and Yu, Y., *ACS Energy Lett.*, **2022**, 7, 1187-1194.
36. Liu, S., Zhang, H., Yu, H., Deng, K., Wang, Z., Xu, Y., Wang, L., and Wang, H., *Appl. Catal. B-Environ.*, **2023**, 336, 122948.
37. Mao, Q., Mu, X., Deng, K., Yu, H., Wang, Z., Xu, Y., Li, X., Wang, L., and Wang, H., *Adv. Funct. Mater.*, **2023**, 2304963.
38. Jia, Y., Jiang, Y., Zhang, J., Zhang, L., Chen, Q., Xie, Z., and Zheng, L., *J. Am. Chem. Soc.*, **2014**, 136, 3748-3751.
39. Jang, S.W., Dutta, S., Kumar, A., Hong, Y.R., Kang, H., Lee, S., Ryu, S., Choi, W., and Lee, I.S., *ACS Nano*, **2020**, 14, 10578-10588.
40. Antony, R.P., Preethi, L.K., Gupta, B., Mathews, T., Dash, S., and Tyagi, A.K., *Mater. Res. Bull.*, **2015**, 70, 60-67.
41. Xiong, Y., Shan, H., Zhou, Z., Yan, Y., Chen, W., Yang, Y., Liu, Y., Tian, H., Wu, J., Zhang, H., and Yang, D., *Small*, **2017**, 13, 1603423.
42. Lu, L., Nie, Y., Wang, Y., Wu, G., Li, L., Li, J., Qi, X., and Wei, Z., *J. Mater. Chem. A*, **2018**, 6, 104-109.
43. Wahidah, H., and Hong, J.W., *Bull. Korean Chem. Soc.*, **2022**, 43, 1111-1117.
44. Wu, J., Zhang, J., Peng, Z., Yang, S., Wagner, F.T., and Yang, H., *J. Am. Chem. Soc.*, **2010**, 132, 4984-4985.
45. Wu, J., Gross, A., and Yang, H., *Nano Lett.*, **2011**, 11, 798-802.
46. Chou, S.-W., Lai, Y.-R., Yang, Y.Y., Tang, C.-Y., Hayashi, M., Chen, H.-C., Chen, H.-L., and Chou, P.-T., *J. Catal.*, **2014**, 309, 343-350.
47. Tian, X.-L., Zhao, X., Wang, L., Wang, H., and Xia, B.Y., *Science*, **2019**, 366, 850-856.
48. Morris, D.J., and Zhang, P., *Chemistry–Methods*, **2021**, 1, 162-172.
49. Hwang, B.-J., Sarma, L.S., Chen, J.-M., C.-H., C., Liu, D.-G., Lee, J.-F., and Tang, M.-T., *J. Am. Chem. Soc.*, **2005**, 127, 11140-11145.
50. Yang, J., Hubner, R., Zhang, J., Wan, H., Zheng, Y., Wang, H., Qi, H., He, L., Li, Y., Dubale, A.A., et al., *Angew. Chem. Int. Ed.*, **2021**, 60, 9590-9597.
51. Choi, S.I., Xie, S., Shao, M., Lu, N., Guerrero, S., Odell, J.H., Park, J., Wang, J., Kim, M.J., and Xia, Y., *ChemSusChem*, **2014**, 7, 1476-1483.
52. Xu, F., Cai, S., Lin, B., Yang, L., Le, H., and Mu, S., *Small*, **2022**, 18, e2107387.

53. Jin, H., Xu, Z., Hu, Z.Y., Yin, Z., Wang, Z., Deng, Z., Wei, P., Feng, S., Dong, S., Liu, J., et al., *Nat. Commun.*, **2023**, 14, 1518.
54. Yan, W., Guo, O., Xing, Q., Liao, M., Shi, Z., Feng, H., Zhang, Y., Li, X., and Chen, Y., *Small*, **2023**, 19, e2300200.
55. Stamenkovic, V.R., Fowler, B., Mun, B.S., Wang, G., Ross, P.N., Lucas, C.A., and Markovic, N.M., *Science*, **2007**, 315, 493-496.
56. Wang, C., Markovic, N.M., and Stamenkovic, V.R., *ACS Catal.*, **2012**, 2, 891-898.
57. Huang, X., Zhu, E., Chen, Y., Li, Y., Chiu, C.Y., Xu, Y., Lin, Z., Duan, X., and Huang, Y., *Adv. Mater.*, **2013**, 25, 2974-2979.
58. Gong, M., Deng, Z., Xiao, D., Han, L., Zhao, T., Lu, Y., Shen, T., Liu, X., Lin, R., Huang, T., et al., *ACS Catal.*, **2019**, 9, 4488-4494.
59. Li, X., Huang, Y., Chen, Z., Hu, S., Zhu, J., Tsiakaras, P., and Kang Shen, P., *Chem. Eng. J.*, **2023**, 454, 140131.
60. Liu, M., Lu, B.A., Yang, G., Yuan, P., Xia, H., Wang, Y., Guo, K., Zhao, S., Liu, J., Yu, Y., et al., *Adv. Sci.*, **2022**, 9, e2200147.
61. Suzuki, A., Nakamura, M., and Hoshi, N., *Electrochem. Commun.*, **2022**, 136, 107235.
62. Han, W., Zhang, X., Wang, R., Bai, T., Liu, H., Cui, L., Liu, J., and Liang, X., *J. Alloy. Compd.*, **2023**, 936, 168287.
63. Chen, W., Gao, W., Tu, P., Robert, T., Ma, Y., Shan, H., Gu, X., Shang, W., Tao, P., Song, C., et al., *Nano Lett.*, **2018**, 18, 5905-5912.
64. Zysler, M., and Zitoun, D., *Part. Part. Syst. Charact.*, **2020**, 37, 2000002.
65. Ding, H., Wang, P., Su, C., Liu, H., Tai, X., Zhang, N., Lv, H., Lin, Y., Chu, W., Wu, X., et al., *Adv. Mater.*, **2022**, 34, e2109188.
66. Li, M., Hu, Z., Li, H., Zhao, W., Zhou, W., Yang, Q., and Hu, S., *ACS Appl. Nano Mater.*, **2022**, 5, 8243-8250.

## Chapter 5. Boron-Insertion Promote Unique Crystal Structure of PdPt Nanocrystals for Superior Electrocatalytic Hydrogen Evolution Activity and Stability

### 5.1. Introduction

Over the past decade, renewable and future clean energy exploration has been in very high demand. Hydrogen ( $H_2$ ), used to produce high energy density, clean, and abundant reserves, is widely considered a promising alternative to fossil resources as a sustainable energy source that can alleviate the rapidly growing demand.<sup>1-3</sup> Currently, electrochemical systems are one of the methods used to convert energy, especially hydrogen production, by hydrogen evolution reaction (HER) in a water electrolyzer, but rationally designing cost-effective, high active, and robust catalysts to facilitate its widespread industrialization is still a formidable challenge.<sup>4-8</sup> Various electrocatalysts have been developed in literature as the central components of electrolyzers.<sup>9-14</sup> Among the various electrocatalysts, platinum (Pt)-based nanomaterials with superior H adsorption feature are still the most efficient catalyst for HER in acidic media because it can catalyze the HER with ultralow overpotentials and small Tafel slopes.<sup>15-18</sup> However, the state-of-the-art Pt-based nanomaterials with its traditional crystal phase (face-centered cubic - fcc) has severe challenges, high cost, sluggish kinetics, and unsatisfied stability, which remarkably limit large-scale commercial implementation. Therefore, designing Pt-based HER electrocatalysts with low cost, high performance and long-term stability in an acidic environment is important.

Encouraging progress for enhanced HER has been created by modulating their crystal structure such as (fcc,<sup>19</sup> hcp,<sup>20</sup> and bcc<sup>21</sup>), alloying Pt-based nanomaterials with another transition metal (Pd,<sup>22</sup> Ru,<sup>23</sup> Rh,<sup>24</sup> Ni,<sup>25</sup> and Co<sup>26</sup>), constructing an ordered structure (Fe,<sup>27</sup> Pb,<sup>28</sup> and Ga<sup>29</sup>), doping with metalloid/non-metal elements, such as B,<sup>30</sup> and P<sup>31</sup>. For instance, Pt-Ni anisotropic superstructures with distinctive morphology and crystal phase with a core fcc-phase and a shell hcp-phase affected the change of coordination environment and chemical bonding at the crystal phase boundaries for highly efficient electrochemical hydrogen evolution reaction (HER).<sup>32</sup> Another progress shows that incorporating B into Pt causes the interstitial doped of B into Pt-Pt lattice at the octahedral - Oh site, giving the super-active electrocatalytic activity compared to their counterparts.<sup>33</sup> However, due to the difficulty in synthesis

and the need for knowledge of the phase diagram, it has been challenging to identify new catalysts with better activity and stability than Pt-based alloy nanomaterials. Phase engineering of nanomaterials (PEN) has recently been proven to be a compelling strategy to modulate the intrinsic properties of noble metal-based nanomaterials, thus enhancing their performances in various applications by precisely tuning the atomic arrangement, which inspires the synthesis of noble metal-based alloy with unconventional phases and the exploration of their phase-dependent catalytic performance. Combining the Pt-based alloy nanomaterials and doping with non-metal elements promotes the change of crystal structure from its traditional crystal structure, possibly enhancing HER activity.

Herein, we report a synthesis procedure to tuning the crystal phase of bimetallic PdPt NCs with tuning by the present of boron (B) might lower the surface level binding energy between Pd and Pt in the PdPt NCs that produces weaken the robust bonding between metals and reaction intermediate to improve the hydrogen evolution electrocatalytic performance. The PdPt–B NCs catalyst achieves the low overpotential HER with 11.8 mV at 10 mA cm<sup>-2</sup>, a small Tafel plots of 14.7 mV dec<sup>-1</sup>, and a high stability test (chronopotentiometric test) with a hundred days, which indicates superior electrocatalytic activity. Our synthetic approach is a unique method, which tunes the traditional crystal structure of traditional PdPt NCs (fcc) to hcp phase transition by introducing the B element into their Pd-Pt nor Pd-Pd lattice in the PdPt NCs.

## **5.2. Experimental section**

### **5.2.1. Chemicals and materials**

Borane tetrahydrofuran (BH<sub>3</sub> in THF, Sigma-Aldrich), Nafion® perfluorinated resin solution (5 wt.%, Sigma-Aldrich), N, N-dimethylformamide (DMF, 99.5%, Sigma-Aldrich), Pd commercial (wt.20%, 99.9%, Alfa Aesar), Pt commercial (wt. 20%, 99.9%, Alfa Aesar), poly(vinylpyrrolidone) (PVP, MW≈55,000, Sigma-Aldrich), potassium tetrachloroplatinate (K<sub>2</sub>PtCl<sub>4</sub>, >99.9%, Sigma-Aldrich), sodium tetrachloropalladate (Na<sub>2</sub>PdCl<sub>4</sub>, >99.9%, Sigma-Aldrich), benzoic acid (BA, ≥99.99%, Sigma-Aldrich), and other chemicals were reagent grade and deionized water with a resistivity of greater than 18.3 MΩ·cm was used in the preparation of reaction solutions.

### **5.2.2. Synthesis of Pd-Pt nanocrystals**

In a typical synthesis of Pd-Pt nanoparticles, 4.8 mL of 20 mM  $\text{Na}_2\text{PdCl}_4$  aqueous solution, 1.2 mL of 20 mM  $\text{K}_2\text{PtCl}_4$  aqueous solution, 210 mg of PVP and 60 mg of benzoic acid were mixed with 10 mL of N, N-dimethylformamide in 50 mL vial. After the vial had been capped, the mixture was ultrasonicated to get the homogeneous mixture. The mixture was transferred into an oil-bath and heated at 130 °C for 5 hours before it was cooled to room temperature. The resulting colloidal products were collected by centrifugation and washed several times with an ethanol-acetone mixture. The synthesis condition to control ratio of Pd-Pt just modified the ratio of Pd: Pt precursor amount, respectively.

### **5.2.3 Synthesis of B-doped Pd-Pt nanocrystals**

40 mg of Pd-Pt nanoparticles were dissolved in 5 mL THF and added with 10 mL of  $\text{BH}_3$  in THF in the Teflon cup, the mixture was sonicated for 10 min before being transferred into a Teflon-lined autoclave. After the reaction for 7 days at 180 °C, the products were collected and washed using centrifugation with ethanol several times at 10,000 rpm for 10 min before drying at 60 °C overnight.

### **5.2.4 Electrochemical measurements**

Electrochemical experiments were performed in a three-electrode cell using EC-Lab Biologic Model SP-300 potentiostat. Graphite rods and Ag/AgCl (3.0 M KCl) were used as the counter and reference electrodes, respectively. The working electrode was prepared by dropping 5  $\mu\text{L}$  of the catalyst ink onto the L-type glassy carbon electrode (GCE, 0.196  $\text{cm}^2$ ). The GCE was cleaned electrochemically via 50 potential cycles ranging from -0.130 to 0.895 V vs. Ag/AgCl at a scan rate of 50  $\text{mV s}^{-1}$ . The HER was performed at room temperature and under acidic conditions (0.5 M  $\text{H}_2\text{SO}_4$   $\text{N}_2$ -purged electrolyte). The potential applied for linear sweep voltammogram (LSV) ranges from 0.05 to -0.25 V vs. RHE with a sweep rate of 10  $\text{mV s}^{-1}$ . Chronoamperometric curves were generated at 0.25 V vs. Ag/AgCl.

### **5.2.5 Characterization**

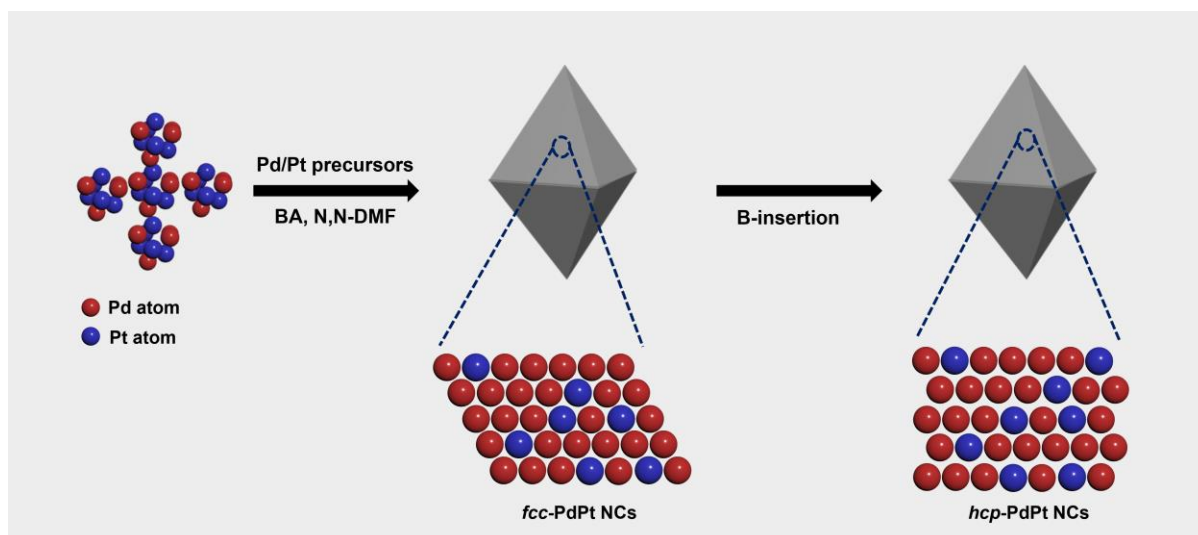
SEM images were obtained from a JEM-2100F (JEOL). TEM, HADDF-STEM, and EDS data were obtained with field-emission transmission electron microscopes (FEI Tecnai G2 F30 S-Twin operated at 300 kV and Talos F200X operated at 200 kV with Super-X system equipped with 4 EDS detectors) or a double Cs-corrected transmission electron microscope (Titan cubed G2 60-300 operated at 300 kV with Super-X system equipped with 4 EDS detectors) after placing a drop of diluted colloidal solution



on a formvar/carbon-coated Cu or Ni grid (300 mesh). The compositions of nanostructures were determined by inductively coupled plasma-optical emission spectrometry (ICP-OES, Spectroblue-ICP-OES (Ametek)). X-ray diffraction (XRD) measurements were conducted on a Rigaku D/MAX2500V/PC using Cu K $\alpha$  (0.1542 nm) radiation. Ultraviolet photoelectron spectroscopy (UPS) and X-ray photoelectron spectroscopy (XPS) valence band measurements were conducted using a Thermo VG Scientific Sigma Probe spectrometer (light source = 1486.6 eV (Al K $\alpha$  X-ray)). Before the preparation of TEM sample, residual chemicals in the catalysts NCs solution were eliminated via centrifugation. The precipitated NCs were re-dispersed into purified water, and an aqueous solution containing nanostructures was then dropped onto the TEM grid (Formvar/Carbon 300 Mesh, Copper). The TEM grid was then dried at room temperature. The TEM grid was cleaned using ethanol before capturing the TEM image. SEM analysis was done using instruments at total-period analysis center for Ulsan chemical industry of the Korea Basic Science Institute (KBSI).

### 5.3. Result and Discussion

The PdPt–B NCs are synthesized by solvothermal reaction under the assistance of  $\text{BH}_3$  as a B-doping source is shown in **Scheme 5.1**. Firstly, PdPt NCs were synthesized using wet-chemical synthesis method, following the previously reported procedure with a slight modification,<sup>34</sup>  $\text{Na}_2\text{PdCl}_4$ ,  $\text{K}_2\text{PtCl}_4$ , benzoic acid, and poly(vinylpyrrolidone) were dissolved in N, N-dimethylformamide. The as-obtained mixture was then heated in an oil bath at 130 °C for 5 h. **Figure 5.1.a** show the high-resolution transmission electron microscopy (HR-TEM) images of majority of the products with  $7.4 \pm 0.3$  nm of average diameter, which demonstrates the successful formation of PdPt NCs. High-angle annular dark field-scanning TEM (HAADF-STEM) images of PdPt NCs displayed a lattice distance of 2.24 Å (**Figure 5.1.b and c**), which matches well with the value of {111} PdPt.<sup>35</sup> The fast Fourier transform (FFT) patterns indicate the fcc metallic feature of the NCs (**Figure 5.1.d**).<sup>36, 37</sup> To prepare the PdPt–B NCs, the boron insertion treatment was performed by dissolved the PdPt NCs in THF solution containing the B source ( $\text{BH}_3$  in THF), presonicated before transferred the mixture into Teflon-lined stainless autoclave and heating for 7 days at 180 °C. **Figure 5.1.e and f** shows HR-TEM and HAADF-STEM images of PdPt after B-insertion, the products have an average diameter sized with  $8.1 \pm 0.2$  nm, which demonstrates the successful B insertion into lattice of PdPt NCs. The hcp lattice for PdPt–B NCs were checked with magnified images (**Figure 5.1.h**) of square region in (f), which highlights the changing the crystal structure from fcc to hcp were determined the characteristic ABAB hcp stacking of Pd–Pt atoms (the bright dots). The distance between characteristic planes (100) and (002) planes are measured to be 2.68 Å and 4.70 Å, respectively, the (002) planes of PdPt–B NCs is smaller compared to the theoretical Pd–B crystal (2.65 Å and 4.77 Å),<sup>38</sup> due to the present of Pt. **Figure 5.1.j** shows the HAADF-STEM-EDS mapping images of PdPt–B NCs. We found that B elements were mix with air during the elemental mapping measurement. Additionally, The EDX spectrum and ICP-OES (**Table 5.1**) reveals the atomic ratio of Pd: Pt: B contents before and after B-insertion is estimated from 4:1 to ~3: 1: 1, which indicated the inserted of B into PdPt makes the Pd leaching during the insertion of B.



**Scheme 5.1.** Schematic illustration of synthesis PdPt–B NCs.

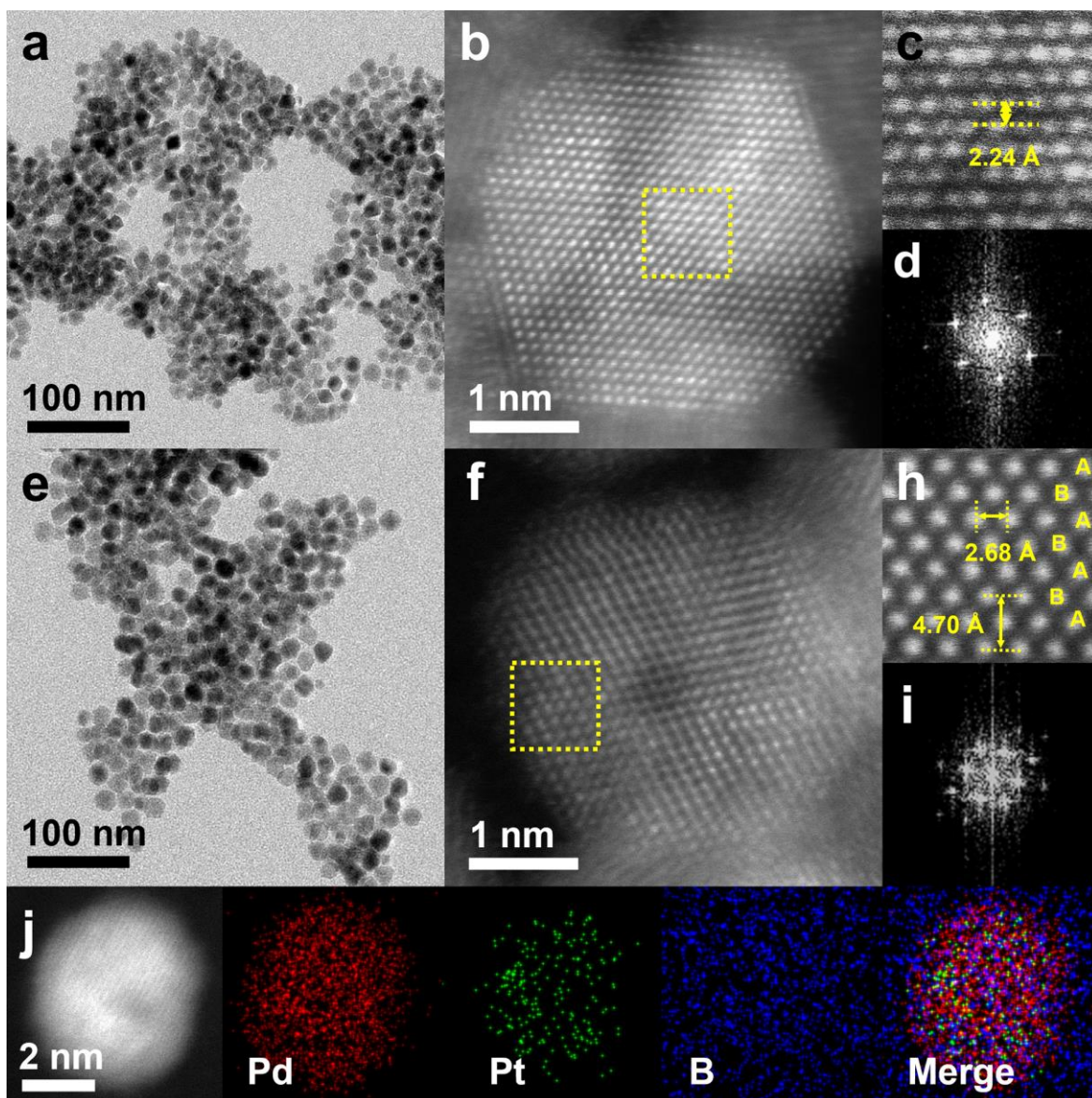


**Figure 5.1.** The characterization of (a–d) PdPt NCs and (e–j) PdPt–B NCs. (a, e) TEM images, (b, f) STEM image, (c, h) inset high magnification-STEM images, (d, i) FFT patterns, and (j) HAADF-STEM-EDS mapping images, respectively.

**Table 5.1.** EDS and ICP-OES analysis result of atomic ratio Pd: Pt: B in PdPt and PdPt–B NCs.

| Catalysts  | EDX Spectrum |           |          | ICP-OES   |           |          |
|------------|--------------|-----------|----------|-----------|-----------|----------|
|            | Pd (At.%)    | Pt (At.%) | B (At.%) | Pd (At.%) | Pt (At.%) | B (At.%) |
| PdPt NCs   | 81.59        | 18.39     | -        | 80.72     | 19.28     | -        |
| PdPt–B NCs | 61.30        | 18.78     | 19.92    | 63.82     | 19.34     | 16.84    |

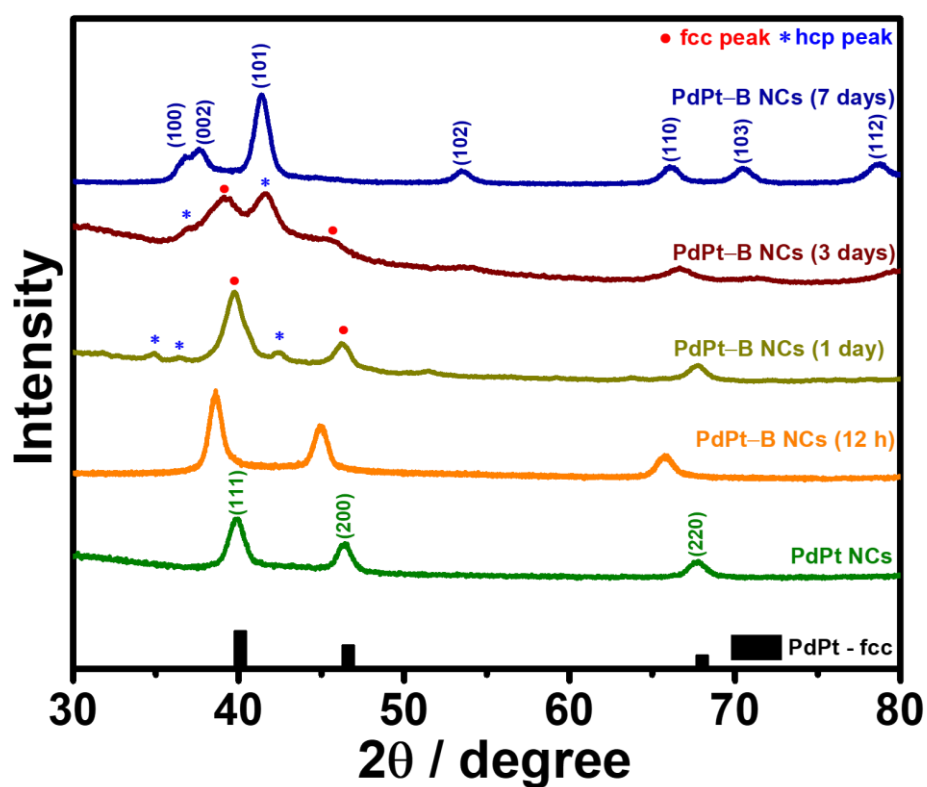


**Figure 5.2.** XRD patterns of pristine PdPt to hcp-PdPt–B NCs. The lines on the bottom show standard XRD pattern of fcc-PdPt structure and hcp-Pd structure.

Interestingly, the hcp crystal structure of PdPt has never been published, the crystal phases of the PdPt–B and PdPt NCs were further identified using the XRD technique. As shown in **Figure 5.2.**, the hcp PdPt–B phase evolves from pure PdPt for 7 days, the fcc lattice disappears completely when B was inserted into Pd–Pt lattice, which indicates the formation of the hcp PdPt–B phase with high phase-purity and high crystallinity. For the first 12 h insertion time, the crystalline of fcc PdPt were shifted to a lower  $2\theta$  value compared to the pristine fcc PdPt, which indicated the enlarged Pd–Pt interlattice spacings due to the insertion of smaller B atoms into the octahedral interstitial sites of PdPt NCs. In the next 12 h insertion time (1 day) the mixture of fcc-hcp phase was shown, the fcc PdPt crystal return in the position following with appearance of hcp small peak ((100), (002), and (101)), the crystal evolution in 3 days insertion also shows the high mixture of fcc-hcp phase and PdPt–B NCs become fully hcp phase in the reaction reach 7 days. The characteristic peaks for hcp lattice as shown in the PdPt–B NCs are  $2\theta = 36.64$  (100),  $37.58$  (002),  $41.43$  (101),  $53.49$  (102),  $66.10$  (110),  $70.55$  (103), and  $78.76$  (112) degree which correspond to a hcp lattice with  $a = 2.82$  Å and  $c = 4.72$  Å. The (110) planes peak were down shift from  $42.26$  (hcp Pd–B standard reference) to  $41.43$  degree, which suggest the different lattice causes from the present of Pt in PdPt–B NCs. For the pure PdPt NCs, all the peaks in the XRD pattern are consistent with the standard PdPt references, further validating the formation of the fcc phase. The B insertion into PdPt different atomic ratio (85:15; and 90:10) also have been tested (**Figure 5.3**), with the same time insertion process shows the perfect change crystal phase from fcc-to-hcp, these provide the direct evidence that the B insertion is slow and accompanied by the fcc-to-hcp transition even with different atomic ratio of PdPt NCs.

In order to better understand the surface electronic interaction for B insertion in PdPt NCs, we performed with X-ray absorption spectroscopy (XAS) measurement. Firstly, X-ray absorption near edge structure (XANES) measurement in **Figure 5.4.a** and b for the Pd K-edge and Pt  $L_3$ -edge of the catalysts. In the **Figure 5.4.a**, the XANES spectrum of PdPt–B NCs shows a positive shift of photon energy compared to PdPt NCs and decreasing of atomic number coordination, which presumably that Pd with B bonding were obtained, the PdPt–B spectrum also has different energy compared to Pd–B, demonstrating the oxygen vacancies were not produces during the metal alloy NCs and insertion of B

into metal NCs, indicating there is no difference pattern of absorption peak. Also, at the Pt L<sub>3</sub>-edge (**Figure 5.4.b**), there was a ~0.15 eV shift between the PdPt–B and PdPt NCs, which may have been induced by the special electronic structure of the B atoms in the PdPt NCs compared to pristine PdPt NCs. Secondly, the local interaction B insertion to PdPt NCs was also experimentally probed by extended X-ray absorption fine structure (EXAFS) spectroscopy. As shown in **Figure 5.4.c**, the presence of B indicated Pd–Pd interaction becomes loose compared with metal-metal interaction (Pd–Pt), the result consistent with the presence of B in the PdPt NCs were Pd–Pt interaction more weakened after cooperating B among the coordinated atom, we predicted this result indicate the B insertion were appear among on the Pd atom. Contrastly, in the case of Pt L<sub>3</sub>-edge (**Figure 5.4.d**), it is shown the negative shift is appeared due to the low coordination among Pt–Pt atoms, but the presence of B did not significantly decrease the coordination among Pt–Pt in the PdPt NCs, which indicate the probability of B appear among Pt–Pt atom is lower compared to Pd–Pd coordination.

We also have measured the X-ray photoelectron spectroscopy (XPS) for comparing PdPt–B and pristine PdPt NCs, **Figure 5.4.e** and **f** shows the detailed result for Pd 3d and Pt 4f. The Pd 3d<sub>5/2</sub> and 3d<sub>3/2</sub> level binding energy is 335.53 and 340.75 eV for PdPt–B NCs, which is shifted to lower binding energy compared to pristine PdPt NCs with 335.68 and 341.00 eV. Interestingly, similar with Pd, the Pt binding energy also shows significant electron transfer, Pt 4f<sub>7/2</sub> and 4f<sub>5/2</sub> level binding energy is 71.09 and 74.34 eV for PdPt–B NCs, which also shifted to the lower value compared to pristine PdPt NCs (71.26 and 74.60 eV). On the other hand, the B 1s binding energy level (**Figure 5.4.g**) peaks mainly at 188.66 eV, indicating the presence of B gives an electron transfer to Pd and Pt in the PdPt–B NCs. To prove our study, another experiment also compared the Pd 3d binding energy of PdPt–B with Pd–B NCs. Based on the result, the Pd 3d of Pd–B NCs not receive much electron from B compared to PdPt–B NCs, which is indicated the PdPt–B could reach much more electron compared Pd–B that could provide better performance in HER process. From the XAS and XPS spectrum, it is clear that the B atoms affected the change the electronic interaction with PdPt, which provides the different activity in the surface of the catalysts. Additionally, the comparison of pure PdPt with Pd and Pt NCs binding energy was shown in **Table 5.2.**, alloying Pd with Pt gives the different electronic interaction that have different binding

energy values compared to single metal NCs.

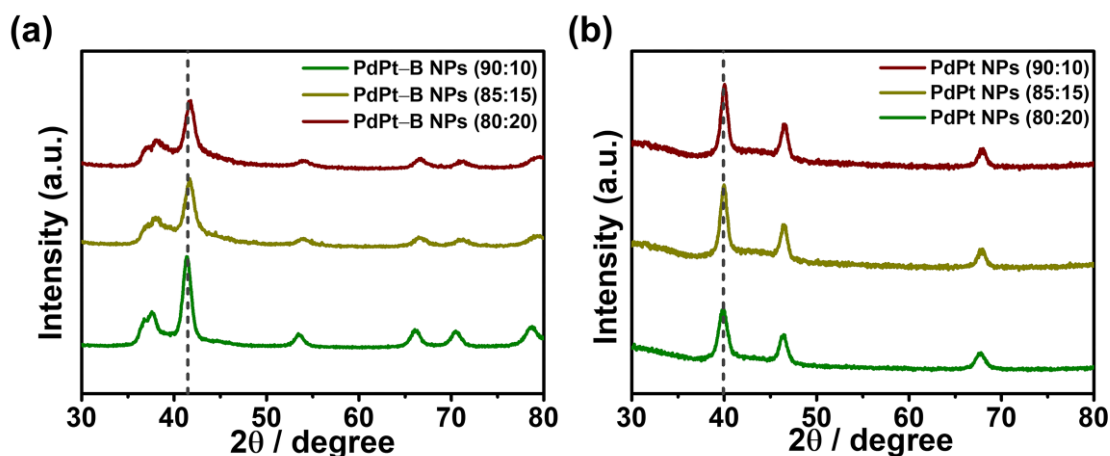


**Figure S2.** XRD patterns of (a) PdPt-B and (b) PdPt NCs with different atomic ratio of Pd: Pt; green (80:20), yellow (85:15), and red (90:10).

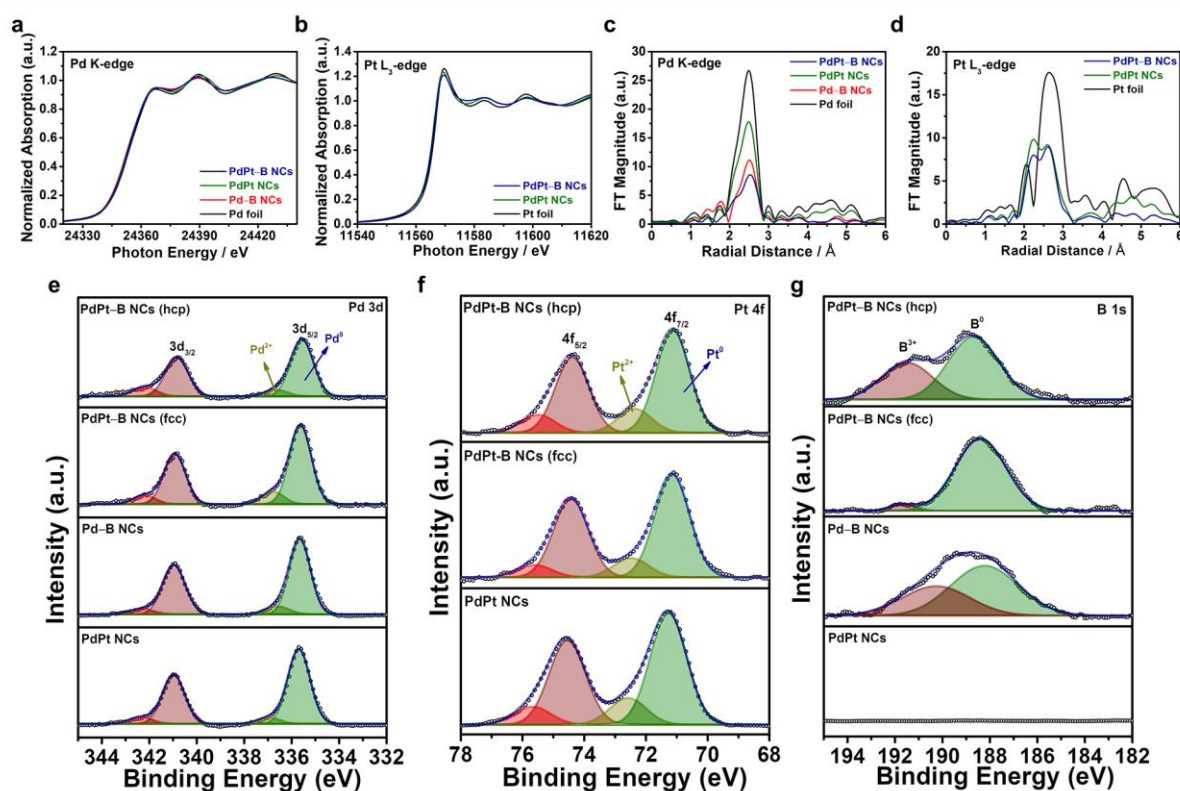


**Figure 5.4.** XAS and XPS spectra of the catalysts. (a, b) XANES spectra, (c, d) EXAFS spectra of Pd K-edge and Pt L<sub>3</sub>-edge, (e, f) XPS spectra of Pd 3d and Pt 4f.



**Table 5.2.** Binding energy value of Pd 3d and Pt 4f of PdPt–B and PdPt NCs include Pd and Pt.

| <b>Catalyst</b>   | <b>Pt 3d<sub>3/2</sub></b> | <b>Pd 3d<sub>5/2</sub></b> |
|-------------------|----------------------------|----------------------------|
| <b>PdPt NCs</b>   | 341.00 eV                  | 335.68 eV                  |
| <b>Pd–B NCs</b>   | 340.92 eV                  | 335.65 eV                  |
| <b>PdPt–B NCs</b> | 340.75 eV                  | 335.53 eV                  |

| <b>Catalyst</b>   | <b>Pt 4f<sub>5/2</sub></b> | <b>Pt 4f<sub>7/2</sub></b> |
|-------------------|----------------------------|----------------------------|
| <b>PdPt NCs</b>   | 74.60 eV                   | 71.26 eV                   |
| <b>Pd–B NCs</b>   | -                          | -                          |
| <b>PdPt–B NCs</b> | 74.34 eV                   | 71.09 eV                   |

| <b>Catalyst</b>   | <b>B 1s<sup>3+</sup></b> | <b>B 1s<sup>0</sup></b> |
|-------------------|--------------------------|-------------------------|
| <b>PdPt NCs</b>   | -                        | -                       |
| <b>Pd–B NCs</b>   | 190.34 eV                | 188.14 eV               |
| <b>PdPt–B NCs</b> | 191.49 eV                | 188.66 eV               |

The electrochemical HER performance were evaluated to prove the insertion of B can boosting catalytic performance of NCs in acidic solution were studied. As a comparison, the commercial Pt/C and Pd/C were also tested under same conditions. Due to the interaction of HER in the surface and intermediate, it might optimize the H adsorption and desorption on the surface site of NCs. As shown in the **Figure 5.5.a**, firstly cyclic voltammograms (CVs) is conducted in N<sub>2</sub>-saturated 0.5 M H<sub>2</sub>SO<sub>4</sub> electrolyte with a typical three-electrode setup at room temperature, it describe the activity of PdPt before and after B dopant have differences due to the modification fcc-to-hcp lattice fringes, it might the evolution of B in the PdPt-B have broader comparing the pristine PdPt, this presumably due to the fact that PdPt-B is the thermodynamically more stable phase comparing the pristine Pd-Pt could makes the catalysts becomes fully resistant to H-corrosion. **Figure 5.5.b, d** and **Table 5.3.** show HER polarization curves of varies PdPt-B NCs, PdPt NCs, Pt/C and Pd/C at scan rate of a 10 mV s<sup>-1</sup>. Impressively, the hcp-PdPt-B NCs shows an overpotential at  $j = 10 \text{ mA cm}^{-2}$  with 11.8 mV is less than that other PdPt-B NCs (PdPt-B<sub>3days</sub> NCs – 20.1 mV, PdPt-B<sub>1day</sub> NCs – 22.8 mV, and PdPt-B<sub>12h</sub> NCs – 23.2 mV), pristine PdPt NCs (23.5 mV), Pt/C (36.0 mV) and Pd/C (122.3 mV), which indicating that hcp-PdPt-B NCs exhibit excellent HER performance, comparable to their pure PdPt, Pt/C and Pd/C. Such low overpotential (11.8 mV) of PdPt-B NCs to drive the current density of 10 mA cm<sup>-2</sup> toward HER is among the lowest values of the reported Pd-based HER catalyst under acidic conditions (**Table 5.4**). The different atomic ratio of Pd: Pt of PdPt-B and PdPt NCs also were tested with HER, **Figure 5.6.** shows the significant result of PdPt NCs after insertion of B, the overpotential values might be higher due to the content ratio of Pd: Pt, which indicated the higher content of Pd in the PdPt NCs will close to pure Pd making the activity become lower in the HER acidic condition, but still higher than that counterpart of commercial Pt/C and Pd/C.

Furthermore, the analysis of Tafel slopes was conducted to evaluate the kinetic behaviors of the catalysts in HER. As shown in **Figure 5.5.c** and **d**, the Tafel slope of hcp-PdPt-B NCs (14.7 mV dec<sup>-1</sup>) is much lower than those of PdPt-B<sub>3days</sub> (17.3 mV dec<sup>-1</sup>), PdPt-B<sub>1day</sub> (22.6 mV dec<sup>-1</sup>), PdPt-B<sub>12h</sub> (24.4 mV dec<sup>-1</sup>), pristine PdPt NCs (25.3 mV dec<sup>-1</sup>), Pt/C (30.5 mV dec<sup>-1</sup>) and even Pd/C (76.8 mV dec<sup>-1</sup>), suggesting the favorable reaction kinetics of hcp phase of PdPt-B NCs catalyst during the HER process.

Additionally, the exchange current density ( $j_0$ ) of the catalyst was obtained by an extrapolation method from the Tafel plots. **Figure 5.5.e** shows PdPt–B NCs catalyst has the larger  $j_0$  ( $2.34 \text{ mA cm}^{-2}$ ), which is about 1.2-, 2.4-, and 3.3-time increase relative to PdPt NCs ( $1.92 \text{ mA cm}^{-2}$ ), Pt/C ( $0.99 \text{ mA cm}^{-2}$ ) and Pd/C ( $0.70 \text{ mA cm}^{-2}$ ), suggesting the superior HER activity of PdPt–B NCs. This speculation is also evidenced by the electrochemical impedance spectra (EIS), where the charge transfer resistance of the PdPt NCs is less than those of PdPt NCs and Pt/C (**Figure 5.5.f**), reflecting the faster HER occurred on the PdPt–B NCs.

Moreover, the long-term electrochemical stability of PdPt–B NCs catalyst was also investigated by the accelerated durability test (ADT) and chronopotentiometric test (CPs). After 10,000 continuous potential cycles, there is no obvious change in the polarization curves just decrease about  $\sim 2.1 \text{ mV}$  of hcp-PdPt–B NCs (**Figure 5.5.g**). The ADT (HER polarization curves) of fcc-PdPt–B<sub>12h</sub> NCs, PdPt NCs, Pt/C and Pd/C also have been tested in the **Figure 5.5.h-j** and **Table 5.4**. as a comparison for our PdPt–B NCs ( $13.9 \text{ mV}$ ), the overpotential HER activity after ADT is  $27.6 \text{ mV}$  (fcc-PdPt–B<sub>12h</sub> NCs),  $28.0 \text{ mV}$  (PdPt NCs),  $50.3 \text{ mV}$  (Pt/C), and  $171.1 \text{ mV}$  (Pd/C), suggesting the dramatic change of counterpart's catalysts morphology and active site structure after the harsh condition of ADT test. The potential applied in the CPs is same with the overpotential of the PdPt–B NCs catalyst ( $11.8 \text{ mV}$ ), the CPs show a negligible variation during the HER test for 100 days (inset of **Figure 5.5.g**). The TEM images of PdPt–B NCs before and after stability test were shown in the **Figure 5.7.**, the morphology of PdPt–B even after the harsh condition (CPs test) remained, indicating not only changes the crystal structure of PdPt but also provide the higher stability of the morphology.

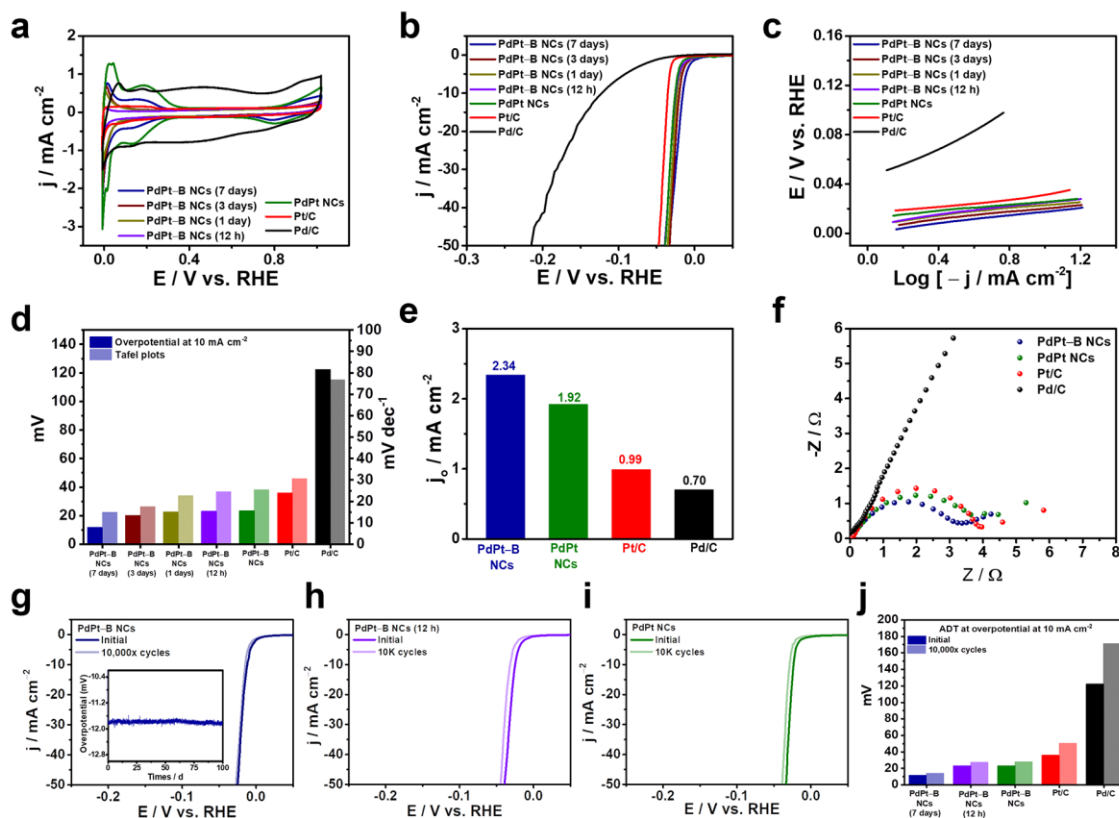


**Figure 5.5.** Electrocatalytic performances of PdPt–B NCs, PdPt NCs, Pt/C, and Pd/C under acid conditions. (a) CVs curves, (b) HER Polarization curves recorded in  $N_2$ -saturated 0.5 M  $H_2SO_4$  electrolyte at a scan rate of 10  $mV s^{-1}$ , (c) Tafel plots for HER obtained from the corresponding polarization curves in (b), and (d) Comparison of the overpotentials for different catalysts at the current density of 10  $mA cm^{-2}$  and Tafel plots, respectively. (e) Exchange current density and (f) EIS spectra of the PdPt–B NCs, PdPt NCs, commercial Pt/C and commercial Pd/C. (g–i) HER polarization curves of PdPt–B NCs, PdPt–B<sub>12h</sub> NCs and PdPt NCs before and after the accelerated durability test. Inset: the chronopotentiometric test of the PdPt–B catalysts at potentials of 10  $mA cm^{-2}$  for 100 days.

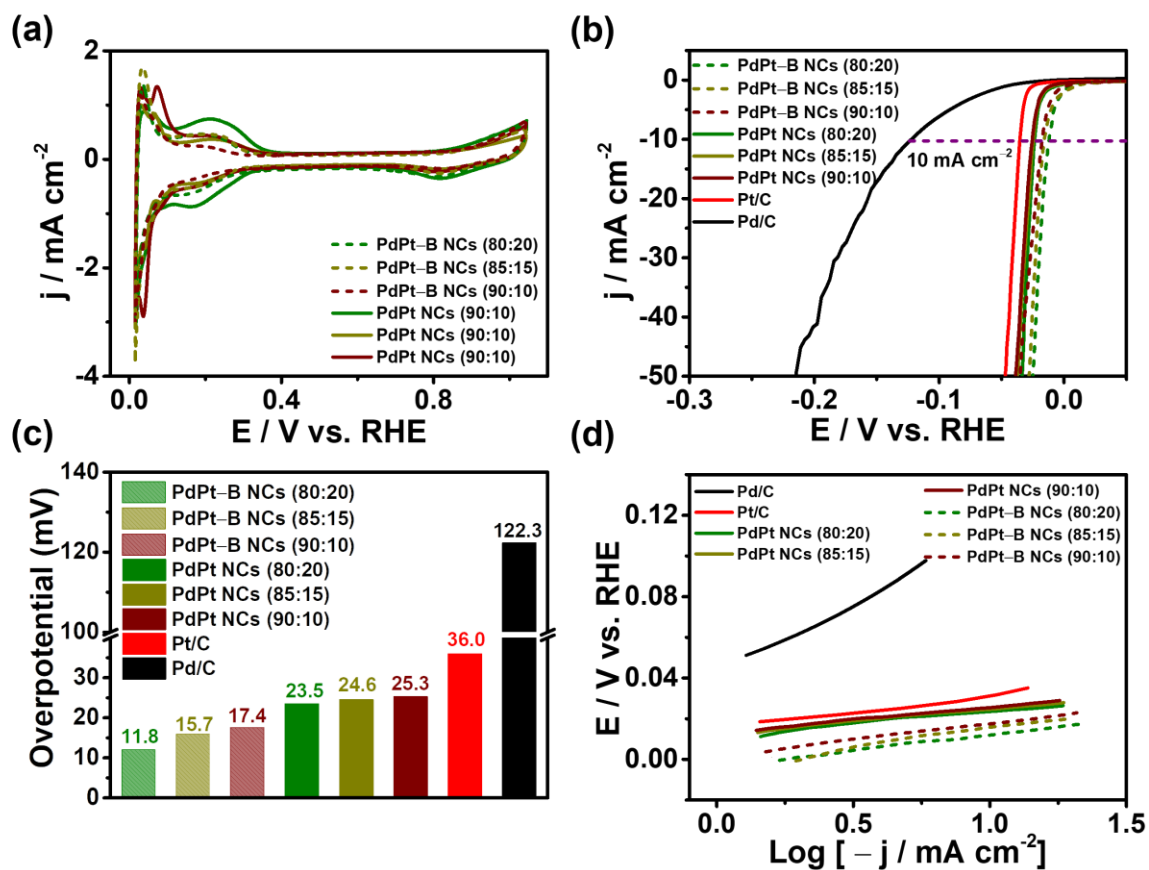


**Figure 5.6.** (a) Cyclic voltammograms, (b) HER polarization curves, (c) Comparison of the overpotentials for different catalysts at the current density of  $10 \text{ mA cm}^{-2}$ , (d) Tafel plots for HER obtained from the corresponding polarization curves in (a) of various PdPt-B and PdPt NCs include counterpart of Pt/C and Pd/C.

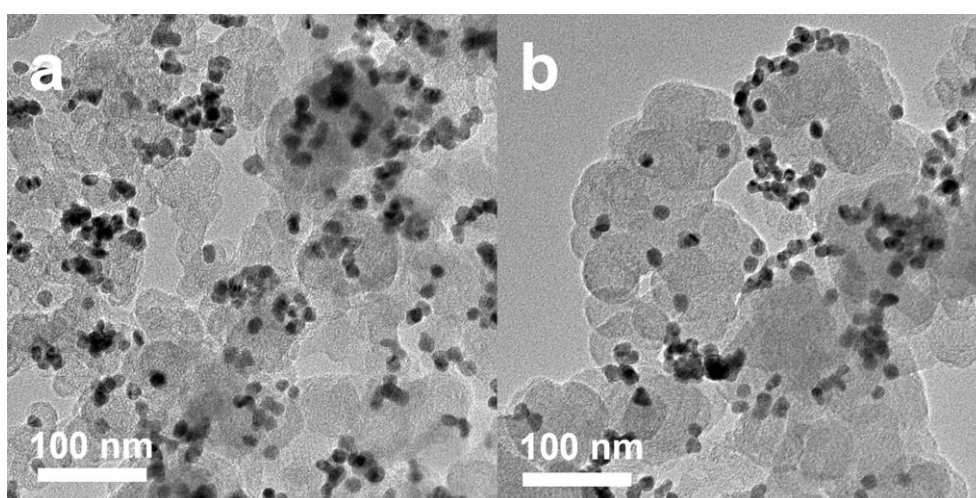


**Figure 5.7.** TEM images before and after chronopotentiometry test for PdPt-B NCs. The (a) before and (b) after test for PdPt-B NCs, respectively.

**Table 5.3.** Activity values for PdPt–B NCs depending on reaction time including commercial Pd/C and Pt/C in HER activity. The value including overpotential at  $10 \text{ mA cm}^{-2}$  and Tafel plots compared in  $0.5 \text{ M H}_2\text{SO}_4$ .

| <b>Catalyst</b>            | <b>Overpotential / <math>\eta</math> (mV)<br/>~10 mA cm<sup>-2</sup></b> | <b>Tafel Plots / (mV dec<sup>-1</sup>)</b> |
|----------------------------|--|--|
| <b>PdPt–B NCs (7 days)</b> | 11.8 mV  | 14.7 mV dec <sup>-1</sup>                  |
| <b>PdPt–B NCs (3 days)</b> | 20.1 mV  | 17.3 mV dec <sup>-1</sup>                  |
| <b>PdPt–B NCs (1 day)</b>  | 22.8 mV  | 22.6 mV dec <sup>-1</sup>                  |
| <b>PdPt–B NCs (12 h)</b>   | 23.2 mV  | 24.4 mV dec <sup>-1</sup>                  |
| <b>PdPt NCs</b>            | 23.5 mV  | 25.3 mV dec <sup>-1</sup>                  |
| <b>Pt/C</b>                | 36.0 mV  | 30.5 mV dec <sup>-1</sup>                  |
| <b>Pd/C</b>                | 122.3 mV   | 76.8 mV dec <sup>-1</sup>                  |

**Table 5.4.** The comparison of HER performance of PdPt–B NCs with some representative Pd-based electrocatalysts in acidic media (0.5 M H<sub>2</sub>SO<sub>4</sub>).

| <b>Catalysts</b>         | <b>Overpotential at<br/>10 mA/cm<sup>2</sup> (mV)</b> | <b>Tafel Slope<br/>(mV/dec)</b> |
|--------------------------|---|---------------------------------|
| <b>PdPt–B NCs</b>        | <b>11.8</b>   | <b>14.7</b>                     |
| <b>PdPt NCs</b>          | <b>23.5</b>   | <b>25.3</b>                     |
| <b>Pt/C</b>              | <b>36</b>   | <b>30.5</b>                     |
| Pd <sub>2</sub> B        | 19  | -                               |
| Pd <sub>2</sub> B        | 15.3  | 22.5                            |
| Rh <sub>2</sub> P        | ~20   | -                               |
| RuP <sub>2</sub> @NPC    | 38  | 38                              |
| PtCoFe@CN                | 45  | 32                              |
| Pd/Cu-Pt                 | 22.8  | 25                              |
| Pt-MoS <sub>2</sub>      | 80  | 40                              |
| AL-Pt/Pd <sub>3</sub> Pb | 13.8  | 18                              |
| Rh-MoS <sub>2</sub>      | 47  | 24                              |
| Au@PdAg/NRB              | 26.2  | 30                              |
| RhCu NTs                 | 12  | 33                              |
| RhFe                     | 25  | 32                              |

The superior HER performance of PdPt–B NCs catalyst could be explained as follows. First, the presence of B can modify the crystal structure of PdPt NCs from the fcc to hcp crystal, which surprisingly has never been reported in our study. Due to the small atom of B, B could possibly be inserted into random Pd–Pt nor Pd–Pd lattice (locates at the octahedral ( $O_h$ ) and tetrahedral ( $T_h$ ) interstitial sites),<sup>30, 33, 39</sup> which is predicted to exhibit much higher intrinsic HER activity than Pt. As shows is the XRD pattern, after the insertion of B into PdPt NCs, the change of crystal structure has clear from fcc to hcp phase and down-shift degree in the (110) position compared to standard Pd–hcp due to the insertion reaction time and Pt composition in PdPt. Second, the presence of B can locally weaken the H–PdPt bonding and facilitate the H–H coupling, which promotes better performance of electrochemical HER activity compared to pure fcc-PdPt NCs.<sup>38, 40-42</sup> Lastly, the B insertion into PdPt NCs could promote the extremely stable catalysts, the stable arrangement of hcp PdPt–B phase provides the active catalyst especially for hydrogenation catalytic reaction.



#### 5.4. Conclusion

We have reported the newest synthesis method to modify the crystal phase by inserting non-metallic elements, especially boron, for PdPt NCs seeds. As a result, PdPt–B NCs have been obtained. Impressively, the synthesized PdPt–B NCs exhibited superior HER performance with an overpotential of only 11.8 mV to achieve the current density of  $10 \text{ mA cm}^{-2}$ , which is even lower than that of pure PdPt NCs, commercial Pt/C and commercial Pd/C and most of reported Pd-based HER catalyst in acid conditions. The excellent catalytic performance places it among the best-reported Pd-based HER electrocatalysts. Compared with the pure “fcc” PdPt NCs, the superior HER performance of “hcp” PdPt–B NCs, e.g., lower overpotential at  $10 \text{ mA cm}^{-2}$  which is smaller Tafel plot value and faster reaction kinetics, demonstrates the crucial role of the crystal phase engineering of nanomaterials in determining their catalytic properties. This work demonstrates a new strategy for the crystal phase-engineering of bimetallic nanoparticles and for improving the electrocatalytic performance of HER. It is highly anticipated that this approach could extend to another non-metallic dopant into nanocrystal systems and even other types of semiconductor materials.

## 5.5 References

1. Glenk, G.; Reichelstein, S., *Nat. Energy*, **2019**, 4, (3), 216-222.
2. Crabtree, G. W.; Dresselhaus, M. S.; Buchanan, M. V., *Phys. Today*, **2004**, 57, (12), 39-44.
3. Wismann, S. T.; Engbaek, J. S.; Vendelbo, S. B.; Mortensen, P. M., *Science*, **2019**, 364, 756-759.
4. Yang, W.; Chen, S., *Chem. Eng. J.*, **2020**, 393, 124726.
5. Dubouis, N.; Grimaud, A., *Chem. Sci.*, **2019**, 10, (40), 9165-9181.
6. Zou, X.; Zhang, Y., *Chem. Soc. Rev.*, **2015**, 44, (15), 5148-80.
7. Lasia, A., *Int. J. Hydrog. Energy*, **2019**, 44, (36), 19484-19518.
8. Wang, S.; Lu, A.; Zhong, C. J., *Nano Conver.*, **2021**, 8, (1), 4.
9. Bender, J. T.; Petersen, A. S.; Østergaard, F. C.; Wood, M. A.; Heffernan, S. M. J.; Milliron, D. J.; Rossmeisl, J.; Resasco, J., *ACS Energy Lett.*, **2022**, 8, (1), 657-665.
10. Jia, Z.; Yang, Y.; Wang, Q.; Kong, C.; Yao, Y.; Wang, Q.; Sun, L.; Shen, B.; Kruzic, J. J., *ACS Mater. Lett.*, **2022**, 4, (8), 1389-1396.
11. Li, L.; Wang, P.; Shao, Q.; Huang, X., *Chem. Soc. Rev.*, **2020**, 49, (10), 3072-3106.
12. Tian, L.; Li, Z.; Xu, X.; Zhang, C., *J. Mater. Chem. A*, **2021**, 9, (23), 13459-13470.
13. Salonen, L. M.; Petrovykh, D. Y.; Kolen'ko, Y. V., *Mater. Today Sustain.*, **2021**, 11-12, 100060.
14. Cui, Z.; Jiao, W.; Huang, Z.; Chen, G.; Zhang, B.; Han, Y.; Huang, W., *Small*, **2023**, 19, (35), e2301465.
15. Hansen, J. N.; Prats, H.; Toudahl, K. K.; Morch Secher, N.; Chan, K.; Kibsgaard, J.; Chorkendorff, I., *ACS Energy Lett.*, **2021**, 6, (4), 1175-1180.
16. Peng, Z.; Yang, H., *Nano Today*, **2009**, 4, (2), 143-164.
17. Cheng, N.; Stambula, S.; Wang, D.; Banis, M. N.; Liu, J.; Riese, A.; Xiao, B.; Li, R.; Sham, T. K.; Liu, L. M.; Botton, G. A.; Sun, X., *Nat. Commun.*, **2016**, 7, 13638.
18. Seh, Z. W.; Kibsgaard, J.; Dickens, C. F.; Chorkendorff, I.; Norskov, J. K.; Jaramillo, T. F., *Science*, **2017**, 355, (6321).
19. Zhang, J.; Le, J.; Dong, Y.; Bu, L.; Zhang, Y.; Cheng, J.; Li, L.; Huang, X., *Sci. China-Chem.*, **2021**, 65, (1), 87-95.
20. Liu, K.; Yang, H.; Jiang, Y.; Liu, Z.; Zhang, S.; Zhang, Z.; Qiao, Z.; Lu, Y.; Cheng, T.; Terasaki, O.; Zhang, Q.; Gao, C., *Nat. Commun.*, **2023**, 14, (1), 2424.
21. Li, J.; Li, F.; Guo, S. X.; Zhang, J.; Ma, J., *ACS Appl. Mater. Interfaces*, **2017**, 9, (9), 8151-8160.
22. Lv, H.; Chen, X.; Xu, D.; Hu, Y.; Zheng, H.; Suib, S. L.; Liu, B., *Appl. Catal. B-Environ.*, **2018**, 238, 525-

23. Yang, Z.; Yang, D.; Wang, Y.; Long, Y.; Huang, W.; Fan, G., *Nanoscale*, **2021**, 13, (22), 10044-10050.
24. Xie, Y. X.; Cen, S. Y.; Ma, Y. T.; Chen, H. Y.; Wang, A. J.; Feng, J. J., *J. Colloid Interface Sci.*, **2020**, 579, 250-257.
25. Li, L.; Wang, S.; Xiong, L.; Wang, B.; Yang, G.; Yang, S., *J. Mater. Chem. A*, **2019**, 7, (20), 12800-12807.
26. Guo, F.; Zou, Z.; Zhang, Z.; Zeng, T.; Tan, Y.; Chen, R.; Wu, W.; Cheng, N.; Sun, X., *J. Mater. Chem. A*, **2021**, 9, (9), 5468-5474.
27. Li, Q.; Zhu, H.; Chen, X.; Liu, H.; Ren, Y.; Chen, Y.; Ohara, K.; Zhou, L.; Chen, J.; Deng, J.; Miao, J.; Lin, K.; Kuang, X.; Xing, X., *J. Am. Chem. Soc.*, **2022**, 144, (44), 20298-20305.
28. Li, Y.; Guo, S., *Nano Today*, **2019**, 28.
29. Liu, X.; Zhao, Z.; Liang, J.; Li, S.; Lu, G.; Priest, C.; Wang, T.; Han, J.; Wu, G.; Wang, X.; Huang, Y.; Li, Q., *Angew. Chem. Int. Ed. Engl.*, **2023**, 62, (23), e202302134.
30. Li, H.; Qin, X.; Zhang, X.-G.; Jiang, K.; Cai, W.-B., *ACS Catal.*, **2022**, 12, (20), 12750-12764.
31. Guo, K.; Fan, D.; Bao, J.; Li, Y.; Xu, D. *Adv. Func. Mater.*, **2022**, 32, (47), 2208057.
32. Cao, Z.; Chen, Q.; Zhang, J.; Li, H.; Jiang, Y.; Shen, S.; Fu, G.; Lu, B. A.; Xie, Z.; Zheng, L. *Nat. Commun.*, **2017**, 8, 15131.
33. Mao, Z.; Ding, C.; Liu, X.; Zhang, Q.; Qin, X.; Li, H.; Yang, F.; Li, Q.; Zhang, X.-G.; Zhang, J.; Cai, W.-B., *ACS Catal.*, **2022**, 12, (15), 8848-8856.
34. Cho, K. Y.; Yeom, Y. S.; Seo, H. Y.; Kumar, P.; Lee, A. S.; Baek, K. Y.; Yoon, H. G., *ACS Appl. Mater. Interfaces*, **2017**, 9, (2), 1524-1535.
35. Pramadewandaru, R. K.; Shim, J.-H.; Lee, Y. W.; Hong, J. W., *Catalysts*, **2021**, 11, (11), 1337.
36. Kim, H. J.; Moon, C. J.; Lee, S.; Theerthagiri, J.; Hong, J. W.; Choi, M. Y.; Lee, Y. W., *J. Mater. Sci. Technol.*, **2023**, 165, 153-160.
37. Li, F.-M.; Gao, X.-Q.; Li, S.-N.; Chen, Y.; Lee, J.-M., *NPG Asia Mater.*, **2015**, 7, (10), e219-e219.
38. Chen, L.; Zhang, L.-R.; Yao, L.-Y.; Fang, Y.-H.; He, L.; Wei, G.-F.; Liu, Z.-P., *Energy Environ. Sci.*, **2019**, 12, (10), 3099-3105.
39. Li, Z.; Xie, Z.; Chen, H.; Liang, X.; Ai, X.; Yuan, L.; Li, X.; Zou, X., *Chem. Eng. J.*, **2021**, 419, 129568.
40. Wei, G. F.; Zhang, L. R.; Liu, Z. P., *Phys. Chem. Chem. Phys.*, **2018**, 20, (44), 27752-27757.
41. Jiang, T.; Yu, L.; Zhao, Z.; Wu, W.; Wang, Z.; Cheng, N., *Chem. Eng. J.*, **2022**, 433, 133525.
42. Yu, Q.; Fu, Y.; Zhao, J.; Li, B.; Wang, X.; Liu, X.; Wang, L., *Appl. Catal. B-Environ.*, **2023**, 324, 122297.

## **Acknowledgement**

I am deeply honored to express my heartfelt gratitude to all those who have supported and encouraged me throughout the completion of this thesis.

First and foremost, I am profoundly thankful to my advisor, Prof. Jong Wook Hong, for his unwavering support, invaluable guidance, and constant motivation. His insightful feedback and suggestions have played a pivotal role in shaping this work, and I am truly appreciative of his expertise and mentorship.

I extend my gratitude to my thesis committee, comprised of Dr. Jaehoon Jung, Dr. Jong Wook Hong, Dr. Dongho Lee, Dr. Min Hyung Lee, and Dr. Young Wook Lee, for their thoughtful comments and constructive critiques, which significantly enhanced the quality of this thesis.

I am grateful for the assistance, advice, and encouragement I received from my peers and friends during the process of working on this thesis. Special thanks to Ghufrani Aulia, Dian Tri L., Hafidatul W., Jasmtiha M., Yu Jieun, Seo Oh-Ryeong, Son Subin, Kim Taegyun, Kim Heon-Chul, and Dr. Poliraju. Their insightful criticism sharpened my thinking and improved the overall piece.

To my friends, I appreciate your understanding and encouragement during my moments of crisis. Your friendship has made my experience in Ulsan and Korea truly wonderful.

Lastly, I want to express my sincere appreciation to my family: my mother, Rita Agus; father, Dwiwandaru P.A.; brothers, Bintang G., and Elang B.; sister-in-law, Dilla R.; nephew, Harvy G.; beloved one, Nisrina P.A.; and other family members. Your love and support have given me the strength to pursue my dreams and reach for the stars.

I am also grateful to Allah SWT for His constant presence and guidance in my life.

I intend for this thesis to stand as a living tribute to all those who have supported me along this journey and for whom my gratitude knows no bounds.

**RESPATI KEVIN PRAMADEWANDARU**

## Curriculum Vitae

### Personal Details

Name: Respati Kevin Pramadewandaru  
Email: respatikevin@gmail.com  
Date of Birth: 30<sup>th</sup> November 1995  
Place of Birth: Jakarta, Indonesia  
Languages Known: Bahasa, English, Korean

### Education

**2020 ~ 2023** Doctor of Philosophy (Ph.D.)

Department of Nano-Energy Chemistry, University of Ulsan, South Korea

**Advisor:** Prof. Jong Wook Hong

**2018 ~ 2020** Master of Science (M.Sc.)

Department of Chemistry, University of Ulsan, South Korea

**Advisor:** Prof. Jong Wook Hong

**2013 ~ 2017** Bachelor of Science (B.Sc.)

Department of Chemistry, Universitas Indonesia, Depok, Indonesia

**Advisor:** Prof. Ivandini T.A.

### Awards & Recognitions

**October, 2022** Poster Presentation at The Korean Chemical Society Conference, Gyeongju, South Korea: “Highly Enhanced Electrocatalytic Performances with Dendritic Bimetallic Palladium-Based Nanocrystals.”

**August, 2022** Poster Awards at International Joint Symposium (Fukuoka University & University of Ulsan), Ulsan, South Korea: “Highly Enhanced Electrocatalytic Performances with Dendritic Bimetallic Palladium-Based Nanocrystals.”

**April, 2022** Poster Presentation at The Korean Chemical Society Conference, Jeju, South Korea: “2D Ultrathin PtNi Porous Nanosheets for Highly Active Oxygen Reduction Reaction.”

**August, 2021** Poster Awards at International Joint Symposium (Fukuoka University & University of Ulsan), Ulsan, South Korea: “2D Ultrathin PtNi Porous Nanosheets for Highly Active Oxygen Reduction Reaction.”

**September, 2020** Received full funding with scholarship program for post graduate students, University of Ulsan, South Korea

### List of Publications/Submission

1. Boron-Insertion Promote Unique Crystal Structure of PdPt Nanocrystals for Superior Electrocatalytic Hydrogen Evolution Activity and Stability, *Under preparation*.
2. Complementary Function of Bi and B in Ternary Pd-Bi-B Alloy Nanocrystals for Highly Durable and Active Electrochemical Ethanol Oxidation, **ACS Catalysis** 2023, *Under submission*.
3. Ultrathin holey Pt-M alloy nanosheets via sequential kinetic-thermodynamic metal reduction control, **Advance Functional Materials** 2023, *Under submission*.
4. Synergistic Effect of Bimetallic Pd-Pt Nanocrystals for the Highly Efficient Methanol Oxidation Electrocatalysts, **RSC Advances** 2023, 13, 27046.
5. Preparation of Palladium-Doped Nickel Phosphide Nanoparticles as Efficient Electrocatalysts for the Hydrogen Evolution Reaction, **ChemNanoMat** 2023, e202300300.
6. Highly Enhanced Electrocatalytic Performances with Dendritic Bimetallic Palladium-Based Nanocrystals, **Catalysts** 2021, 11(11), 1337.
7. Active Bumpy Pt-Pd Nanocubes for Methanol Oxidation Reaction, **Bull. Korean Chem. Soc.** 2020, 41, 237-240.